Institut für
Kontinuumsmechanik

Multiscale crack propagation and crack coalescence using the XFEM

Matthias Holl

B14/1

Leibniz
Universität
Hannover

ISBN 978-3-941302-09-9

Many materials contain microcracks which influence the overall behavior of the structure, especially in case of crack propagation and crack coalescence. To consider microcracks efficiently, they are taken into account in a domain of interest, here around the crack fronts, by applying the multiscale projection method. To capture the physical properties of cracks accurately and to avoid remeshing during the crack propagation process, all cracks in the multiscale problem are modeled using the eXtended Finite Element Method (XFEM).
To allow for crack propagation of microcracks as well as macrocracks, and to model crack coalescence of cracks from different scales, propagation and coalescence of cracks is computed on the finest scale. Stable crack growth is achieved via an adjustment of the applied boundary conditions acting on the coarsest scale. Due to crack propagation, the respective crack fronts change their positions such that the fine scale domains move fully adaptive through the domain.

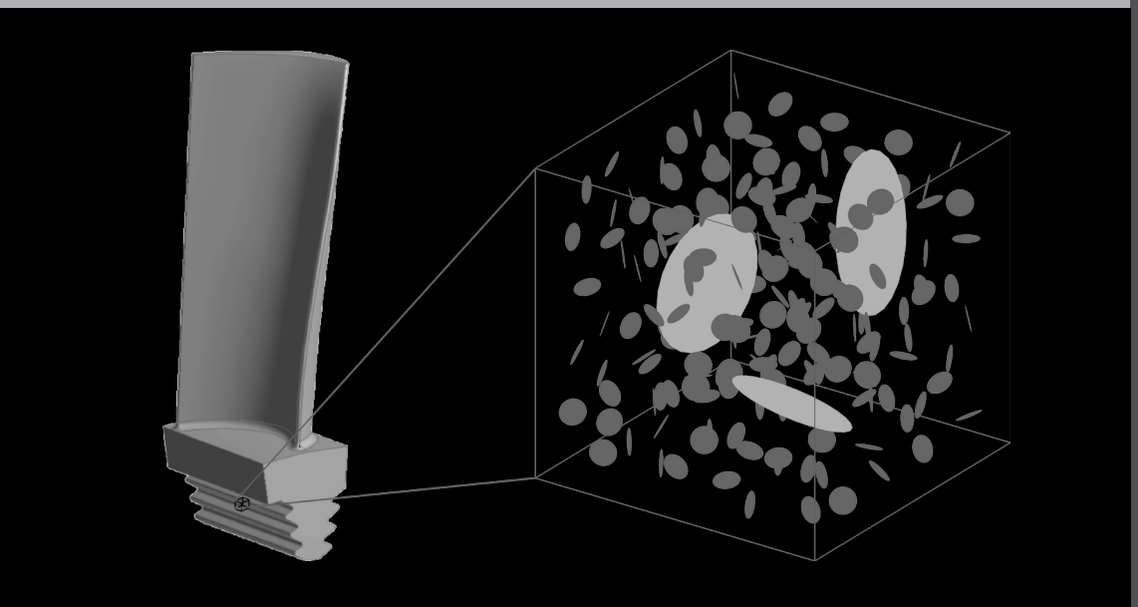

Matthias Holl | Multiscale crack propagation and crack coalescence using the XFEM

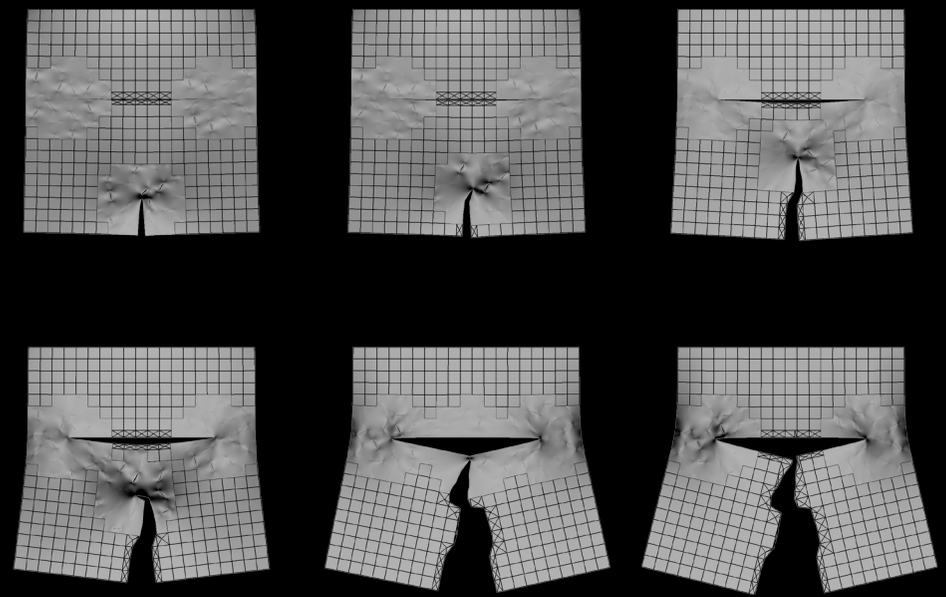

Multiscale crack propagation and crack coalescence using the XFEM

B14/1

Matthias Holl

Leibniz
Universität
Hannover

Institut für
Kontinuumsmechanik

To my friends and family

Zusammenfassung

In dieser Arbeit wird die Interaktion von Mikro- und Makrorissen im Bezug auf die globale Systemantwort, insbesondere makroskopische Größen wie Risspfad und Lastverlauf, für spröd brechende Materialien numerisch untersucht. Anhand dieser Ergebnisse soll festgestellt werden, welchen Einfluss vorhandene Mikrorisse auf diese Antwortgrößen haben.
Zur Modellierung von Rissen wird die extended finite element method verwendet, so dass in Kombination mit Abstandsfunktionen eine weitestgehende netzunabhängige mechanische und geometrische Beschreibung von Rissen erfolgt. Zur präzisen Approximation des Verschiebungsfeldes beinhalten die Ansätze die asymptotische analytische Lösung erster Ordnung des Rissspitzenfeldes. Insbesondere bei Rissfortschritt bietet diese Methode herkömmlichen Methoden gegenüber den Vorteil der netzunabhängigen Rissbeschreibung, so dass eine Neuvernetzung nicht notwendig wird. Neben einem weitverbreiteten Energiekriterium zur Vorhersage von Rissfortschritt, wird ein weiteres Kriterium, basierend auf einem Schädigungsmodell, vorgestellt.
Der große Längenunterschied von Mikro- und Makrorissen würde bei herkömmlichen numerischen Verfahren zu einem enormen Rechenaufwand führen, da für eine präzise Modellierung der Mikrorisse ein feines Netz benötigt würde. Die sogenannte Multiskalenprojektionsmethode hingegen bietet eine numerisch zeitgünstige Möglichkeit Mikrorisse in bestimmten Gebieten aufzulösen ohne die Qualität der Lösung signifikant zu verändern. Eine parallele Berechnung der Feinskalengebiete mit OPENMP sorgt zusätzlich für eine Reduzierung der Rechenzeit.
Da Mikrorissfortschritt nur auf der feinsten Skala möglich ist und das Verschiebungsfeld auf dieser Skala zudem am besten approximiert wird, wird die Struktur auf dieser Skala auf Rissfortschritt überprüft. Zur Verfolgung eines stabilen Risspfades bei mehrskaligem Rissfortschritt wird ein skalenübergreifendes Kurvenverfolgungsverfahren vorgestellt. Um zudem auf allen Skalen identische Geometrien zu erhalten, werden fortschreitende Makrorisse von der feinen Skala auf die gröbste Skala übertragen.
Die Modellierung von Rissvereinigung setzt neue Ansatzfunktionen voraus, welche mehrere Risse sowie deren Kreuzungspunkte in einem Element abbilden können. Neben diesen Funktionen wird ein geeignetes Kriterium für Rissvereinigung eingeführt.
Zur Modellierung von Rissvereinigung unter Verwendung der Multiskalenmethode werden zusätzliche Ansatzfunktionen für sich nähernde Rissspitzen eingeführt. Eine neue Rampenfunktion sorgt für die Erfüllung der partition of unity in allen Elementen, sowie für eine Verkleinerung des ange-reichertern Bereiches auf der groben Skala. Zur numerisch effektiven skalenübergreifenden Modellierung von Rissvereinigung werden die entstehenden Risspfade auf die grobe Skala übertragen, so dass sie mit den dort üblichen Ansatzfunktionen dargestellt werden können. Anhand von zahlreichen Beispielen werden abschließend die Effekte von Mikrorissen und die Robustheit der entworfenen Methode dargelegt.

Schlagworte: XFEM, Rissfortschritt, Rissvereinigung, Mehrskalenmodellierung

Abstract

This work numerically investigates the interaction between microcracks and macrocracks in brittle media. This enables an investigation into the effect microcracks have on the global response of the structure, i.e. crack path and required loading behavior.
extended finite element method in combination with the level set method is applied in order to model the cracks, yielding an almost mesh independent tool to model cracks with a high level of accuracy. In order to capture the displacement field that accurately, the ansatz contains the first order asymptotic analytical solution for the near tip field. This crack description is beneficial, especially once cracks propagate: Thus, remeshing is avoided during fracturing processes. Besides a well-known energetic fracture criterion, a new damage-based criterion is also proposed.
Traditional numerical approaches require long computation times for the precise description of microcracks and macrocracks, as microcracks induce fine meshes. However, great differences in the size of microcracks and macrocracks allow scale separation and thus the application of the so-called multiscale projection method. This method enables the restriction of microcracks to regions of interest alone, leading to shorter computation times without changing the solution significantly. A parallel computation of the microdomains via OPENMP yields an additional speed-up in solution time.
As the propagation of microcracks is only possible at the respective scale and as the solution is most accurate there, crack propagation is performed to this scale. In order to follow a stable crack path, load control between the scales is introduced for multiscale crack propagation. Additionally, a mapping strategy is introduced to upscale propagating macrocracks to their corresponding scale, to ensure the same geometry on all scales.
As crack coalescence might result in intersecting cracks, the enrichment functions are extended to be capable of modeling junctions in crack paths. Besides this additional enrichment functions, a criterion for crack coalescence is also introduced.
Modeling crack coalescence in a multiscale framework also requires additional shape functions to model approaching crack tips. Furthermore, a new ramp function is introduced, reducing enrichment functions to only cracked elements on the coarse scale. To preserve a fast computation, merged macrocracks must be mapped onto the coarse scale, such that they can be represented using interpolation functions of that scale. Some examples demonstrate the robustness of the presented method as well as state the effect of microcracks.

Key words: XFEM, crack propagation, crack coalescence, multiscale

Acknowledgements

This thesis is the result of my four-year research work at Insitute of Continuum Mechanics (IKM) at the Gottfried Wilhelm Leibniz Universität Hannover under guidance of Prof. Peter Wriggers. The project was supported by the German Research Foundation (DFG) and was part of the Collaborative Research Centre 871 (SFB 871).

First of all, I thank my advisor and principal referee Prof. Peter Wriggers for his constant support and trust as well as the excellent working climate during my time at the IKM. This was mainly featured by academical freedom to implement own ideas as well as sound academical advice and discussions of ideas when it was needed. Prof. Peter Wriggers encouraged and supported me to present and discuss my work on international conferences, from which I benefited extremely.

Secondly, I thank my second referee Prof. Nicolas Moës for his effort to come to Hanover, for fruitful discussions on conferences as well as for his invitation to the Institut de Recherche en Génie Civil et Mécanique (GeM) at École Centrale de Nantes (ECN). During the last four years, his publications introduced me to the eXtended Finite Element Method and constantly enriched my knowledge about this method.

My sincere thanks goes also to my colleagues from the IKM and the SFB 871 for the pleasant working atmosphere, their openness for scientific exchange in terms of raising and answering questions and for many shiny moments during and after scientific conferences. Especially Dr. Stefan Löhnerts had always an open door, offered discussions and encouraged me in my research work. I am thankful for the enjoyable time I had in my office with my office mates, with whom I shared nearly daily the advantages and disadvantages of research. I would also like to acknowledge the work of the technical staff and the office staff, who organized the background work of the research activity.

Finally, I thank my friends and my family for their constant support at any time.

Hannover, January 2014 Matthias Holl

Contents

1 Introduction **1**
- 1.1 Background and state of the art . . . 2
- 1.2 Structure of this work . . . 4

2 Continuum solid mechanics **5**
- 2.1 Kinematics . . . 5
- 2.2 Stresses . . . 9
- 2.3 Balance laws . . . 9
- 2.4 Material theory . . . 13
- 2.5 Weak form of equilibrium . . . 15
- 2.6 Linear elastic fracture mechanics . . . 16

3 Finite Element Method **27**
- 3.1 Bilinear/trilinear displacement Finite Element approach . . . 27
  - 3.1.1 Isoparametric concept . . . 28
  - 3.1.2 Discretization of the weak form . . . 30
  - 3.1.3 Numerical integration and solution procedure . . . 30
- 3.2 Fundamentals of the eXtended Finite Element Method . . . 31
  - 3.2.1 Level set method . . . 32
  - 3.2.2 Enrichment functions . . . 33
  - 3.2.3 Integration . . . 35
  - 3.2.4 Mesh regularization . . . 37
- 3.3 Discretization of non-local strain field . . . 40

4 Multiscale approach **43**
- 4.1 Weak form . . . 44
- 4.2 Continuity condition . . . 46
- 4.3 Solution procedure . . . 47

5 Crack propagation using the XFEM **51**
- 5.1 2D crack propagation . . . 51
  - 5.1.1 Crack propagation on one scale . . . 51
  - 5.1.2 Multiscale crack propagation . . . 56
- 5.2 2D crack coalescence . . . 58
  - 5.2.1 Crack coalescence on one scale . . . 59

5.2.2 Multiscale crack coalescence 66
5.3 3D crack propagation 85
5.3.1 Crack propagation on one scale 85
5.3.2 Multiscale crack propagation 99

6 Conclusions and outlook **109**

Bibliography **112**

CURRICULUM VITAE **125**

Chapter 1

Introduction

Analytical solutions of loaded cracked structural components, such as the cracked turbine blade displayed in figure 1.1, are usually not available or require too many simplifications. Using skilled manual workers to judge the effect of cracks might yield conservative or risky decisions and is furthermore strongly dependent on the expert. Overcautious and conservative judgments lead to high overhauling costs or high scrape rates. In the unfavorable case of an overly risky decision, the component might fail which can lead to catastrophes such as the *Eschede train disaster* (1998), which occurred due to the rupture of a rail wheel. To circumvent purely analytical models and to dependent not only in the judgments of experts, numerical methods are applied to investigate the behavior of complex mechanical tasks.

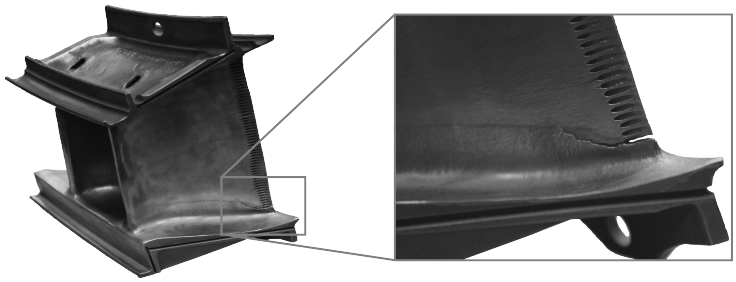

Figure 1.1: Cracked turbine blade [SFB 871, Leibniz Universität Hannover].

Numerical solution methods such as the finite element method gained attention in recent decades as these methods can be applied to several kinds of physical and geometrical problems. Regarding fracture mechanics, traditional numerical solution methods are not able to capture the main features of fracturing solids accurately and numerically efficiently, even though numerical fracture mechanics have been involved in research for about forty years.
Small defects such as microcracks are present in a vast amount of structures due to overhauls or minor production imperfections. However, most current computational approaches are not able to take these fine scale defects into account in a computationally efficient framework without drastic restrictions to the model. Nevertheless, these defects might influence the global response of the structure drastically: Crack shielding and crack amplification might occur, which can affect the external load required to perform crack propagation. Besides the critical load, fine scale features might influence the crack path due to crack coalescence. Thus, these defects might be responsible for failure and shall be investigated in computa-

tions. Hence, computationally efficient multiscale strategies are needed to investigate the effect of fine scale features on the global response of a structure.

1.1 Background and state of the art

Since the development of the finite element method, various numerical tools for modeling cracks and their propagation have been developed, e.g. meshfree methods as summarized by FRIES (2005). Within the finite element method, two generally different models for simulating fracturing processes appeared: Continuum softening models and discrete crack models. The most widely used continuum softening models are the so-called damage models, summarized by BAŽANT ET AL. (1984), LEMAITRE (1986) and SIMO & JU (1987a,b) among others. Cracks are modeled via softening variables relating known field quantities, e.g. strains, to damage variables, which are driven by constitutive equations. To overcome numerical drawbacks such as mesh dependency, non-local damage models by PIJAUDIER-CABOT & BAŽANT (1987) and LASRY & BELYTSCHKO (1988) and gradient enhanced damage models by PEERLINGS ET AL. (1996) gained attention and are nowadays frequently employed. These models can be applied to a broad range of different material models, but require a lot of experiments to resolve all material parameters. Current research by MOËS ET AL. (2011) and BERNARD ET AL. (2012) aims to find new techniques to store and to propagate crack surfaces. A more recent approach of continuum softening models are phase-field models, introduced by BOURDIN (1998), BOURDIN ET AL. (2008) and MIEHE ET AL. (2010). These models reformulate brittle fracture such that similar governing equations to those for gradient enhanced damage models are obtained. Thus, infinitesimal small finite elements capture the crack path highly precisely according to the respective fracture criterion. Consequently, recent research focalizes on adaptive refinement and higher order methods as illustrated by BORDEN ET AL. (2012). A similar mechanical model was applied recently by PANDOLFI & ORTIZ (2012). However, modeling fracture is achieved via an eigenerosion of finite elements and not via traditional softening. An advantage of all softening models is their ability to model crack nucleation, enabled by their additional governing equation and their continuous material degradation. Furthermore, the resulting path and the fracture criterion are comparably easy to implement. A disadvantage is that non-local and phase-field models generally yield a non-symmetric system matrix and furthermore non-linear systems to solve, even in linear elastic fracture mechanics. Additionally, a sharp crack path requires a fine mesh or adaptive refinement. However, an adequate singular stress field at the crack front can still not be achieved due to the ductile behavior, naturally induced by softening. Due to the ability to model crack nucleation and propagation, softening models are frequently applied to virgin materials.

Research about discrete crack models aimed first at improving the accuracy of finite element solutions for cracked solids: While CHAN ET AL. (1970) present an adaptive method to capture features of the crack tip precisely, BYSKOV (1970) suggests subdividing cracked finite elements to gain accuracy. To meet the order of singularity in the stress field of the first order analytical solution, BENZLEY (1974) enriches the standard finite element approximation, which is the basis of todays extended finite element method. An alternative approach was exploited by HENSHELL & SHAW (1975): Instead of enrichment functions, the order of sin-

gularity is obtained by collapsing finite elements, which is the basis for integrating singular functions highly accurately following DUFFY (1982). With the so-called partition-of-unity method by MELENK & BABUŠKA (1996) enrichment strategies for several types of problems became popular, such that non-propagating cracks could be investigated accurately. Besides an accurate solution of the near-tip field, propagating cracks require a numerical method to follow the crack path. As remeshing performed by e.g. BITTENCOURT ET AL. (1996) is computationally expensive, methods to decouple the crack from the finite element mesh developed rapidly: A prominent member of these methods is the so-called strong discontinuity approach by SIMO ET AL. (1993) and OLIVER (1995, 1996a,b): In contrast to the partition-of-unity method it is not able to capture the stress field that accurately. Furthermore, the crack propagation step depends on the finite element mesh, as this method can only distinguish between completely cracked and non-cracked elements. A second common method is the extended finite element method/generalized finite element method introduced by BELYTSCHKO & BLACK (1999), MOËS ET AL. (1999), STROUBOULIS ET AL. (2000) for two-dimensional problems and by DUARTE ET AL. (2000), SUKUMAR ET AL. (2000), MOËS ET AL. (2002) for three-dimensional problems, resolving both issues: By evoking the partition-of-unity method, the stress field is captured accurately and by describing the crack using level set fields introduced by OSHER & SETHIAN (1988) and combining these fields to the enrichment functions as introduced by STOLARSKA ET AL. (2001), the crack can propagate independent of the finite element mesh. Adding further enrichment functions according to DAUX ET AL. (2000) even allows to capture intersecting cracks, which was an essential ingredient for BUDYN ET AL. (2004) to model merging cracks. Besides improving convergence by BABUŠKA & BANERJEE (2012) and LOEHNERT (2013) among others, current research seeks inter alia accuracy improvements by PASSIEUX ET AL. (2011), MINNEBO (2012) and PEREIRA ET AL. (2012). In contrast to softening models, discrete models cannot predict crack nucleation simultaneously hand. Furthermore, independent of the numerical method, the crack surface description requires additional effort, especially for merging cracks. Due to this accurate representation of the crack path, the solution in the vicinity of the crack front gains accuracy. A mesh independent crack path description via enrichment functions combined with e.g. level sets additionally provides a flexible framework to simulate propagating cracks. Thus, discrete crack models are mainly applied to model crack growth of already cracked structures.

In order to model crack nucleation within a discrete crack model, coupling of softening models to discrete crack models is a popular choice, demonstrated by MAZARS & PIJAUDIER-CABOT (1996), AREIAS & BELYTSCHKO (2005), MEDIAVILLA ET AL. (2006a) and SEABRA ET AL. (2013) among others. Once no stiffness remains in a finite element due to softening, a discrete crack is inserted. The damage model induces nearly all drawbacks from softening models, i.e. an unsymmetric system matrix and a fine mesh. To overcome the fine mesh, MOËS (2013) applies mesh coarsening in discrete cracked areas to achieve shorter computation times with nearly identical results. Thus, these methods are a promising alternative to pure softening models.

To take into account micro effects with computational efficiency, multiscale methods are frequently applied in solid mechanics. Following GEERS ET AL. (2010), traditional multiscale techniques such as the variational multiscale method by HUGHES (1995) and the FE^2 method

by MIEHE ET AL. (1999) and FEYEL & CHABOCHE (2000) do not account for localization effects on the fine scale, meaning that so-called continuous-discontinuous multiscale techniques require application. These approaches were applied to damage mechanics by MASSART ET AL. (2007) and COENEN ET AL. (2012), and to fracture mechanics by LOEHNERT & BELYTSCHKO (2007b) and BELYTSCHKO ET AL. (2008). Depending on the properties of the fine scale effects, some of these methods can even nucleate cracks on the coarse scale as for instance the so-called multiscale aggregating discontinuity method by BELYTSCHKO ET AL. (2008) and COENEN ET AL. (2012).
Further previous achievements in fracture mechanics, numerical treatment of cracks and multiscale techniques are summarized in the following chapters of this work.

1.2 Structure of this work

In the first part of this work, the basic governing equations are summarized, followed by an introduction of linear elastic fracture mechanics including a sketch of damage mechanics.
The basic concepts of the finite element method are introduced in section 3. In order to model cracks in linear elastic media accurately, this approach is enhanced to the state of the art of the extended finite element method. Following, the introduced damage model is coupled to the derived finite element approach. With the applied damage evolution, this coupling yields a cheap and simple damage model for brittle materials.
In order to capture effects in the fine scale with computational efficiency, the so-called multiscale projection method by LOEHNERT & BELYTSCHKO (2007a) is applied. Thus, chapter 4 sketches the main aspects of this method, introducing a parallel computation via OPENMP[1] of the fine scale domains.
The numerical modeling of cracks, crack propagation and crack coalescence in a multiscale framework using the extended finite element method is derived in chapter 5. First, the underlying theory for two-dimensional problems without considering microcracks is introduced. Subsequently, this approach is embedded into the multiscale projection method requiring a load control scheme across the scales. The following investigation of merging cracks on one scale requires a criterion for crack coalescence as well as an extension of several introduced features, i.e. enrichment schemes, enrichment functions, quadrature and storage of crack surfaces. The last section for two-dimensional problems finally includes crack coalescence in the proposed multiscale method. The focus is set on the interaction of cracks from different scales, including several coalescence scenarios and enrichment patterns. The effect of fine scale features on the global response of the structure is exhibited in numerical examples. Three-dimensional problems are introduced hereafter: As the extension of one dimension increases the dimension of cracks as well, crack propagation is revisited. Thus, the computational aspects as well as mechanical properties occurring due to this extra dimension are accentuated. Applying the multiscale projection method in the last section of this chapter allows to demonstrate the effect of fine scale features on the crack path.
Finally, chapter 6 summarizes this work. The limits of the proposed models are emphasized, yielding perspectives and possible future work of the proposed models.

[1] http://openmp.org

Chapter 2

Continuum solid mechanics

This chapter briefly summarizes the main aspects of continuum mechanics for solid media as used in this work. There is a huge variety of literature that introduces continuum solid mechanics including kinematics, balance laws, material theory as well as variational principles, e.g. TRUESDELL & NOLL (1965), MALVERN (1969), ALTENBACH & ALTENBACH (1994), CHADWICK (1999), HOLZAPFEL (2000), HAUPT (2002), GURTIN ET AL. (2010) among others.
Fracture mechanics requires a special treatment in the concept of continuum mechanics, as discussed by e.g. ANDERSON (2005), GROSS & SEELIG (2007) among others.

2.1 Kinematics

This section briefly summarizes the kinematics of continua, i.e. their deformation and motion in time at each material point $\mathcal{P}$. Furthermore, the most general deformation tensors as well as strain tensors are introduced.

Deformation

Considering a material body $\mathfrak{B}$ as a set of continuously distributed material points $\mathcal{P}$ in EUCLIDean space $\mathbb{R}^3$ is a fundamental assumption in the continuum theory. The coherence between those points is preserved during the deformation process, which allows the deformation to be described by a continuous, one-to-one mapping of each material point $\mathcal{P}$ from the material body $\mathfrak{B}$ to a region $\mathcal{B}$. This mapping is defined by a bijective function $\boldsymbol{\chi}$

$$\boldsymbol{\chi} : \mathfrak{B} \longrightarrow \mathcal{B} \quad . \tag{2.1}$$

Assuming the material body $\mathfrak{B}$ is occupying the region $\mathcal{B}_0$ at time $t_0 = 0$ and the region $\mathcal{B}_t$ at time t, the position vector of an arbitrary material point $\mathcal{P}$ at time t_0 follows

$$\boldsymbol{X} = \boldsymbol{\chi}_0 (\mathcal{P}) \quad , \tag{2.2}$$

where $\boldsymbol{X} \in \mathcal{B}_0$. At an arbitrary time $t > t_0$ the position vector of point $\mathcal{P}$ can be denoted by $\boldsymbol{x} \in \mathcal{B}_t$

$$\boldsymbol{x} = \boldsymbol{\chi}_t (\mathcal{P}) \quad . \tag{2.3}$$

Since the mapping $\boldsymbol{\chi}$ is bijective, a unique inverse function $\boldsymbol{\chi}^{-1}$ exists at all times t_0, t. Therefore, the mapping between both position vectors $\boldsymbol{x}$ and $\boldsymbol{X}$ is unique and well defined

$$\boldsymbol{X} = \boldsymbol{\chi}_0 \left(\boldsymbol{\chi}_t^{-1} (\boldsymbol{x}) \right) \quad , \tag{2.4}$$

$$\boldsymbol{x} = \boldsymbol{\chi}_t \left(\boldsymbol{\chi}_0^{-1} (\boldsymbol{X}) \right) \quad . \tag{2.5}$$

Expressing all field variables in terms of $\boldsymbol{x}$ is referred to as current configuration, EULERian or spatial description. The observer follows the deformation in a spatial point (2.4). The initial configuration, LAGRANGian or material description considers an observer being fixed to a material point. All field variables are expressed in terms of $\boldsymbol{X}$ (2.5).

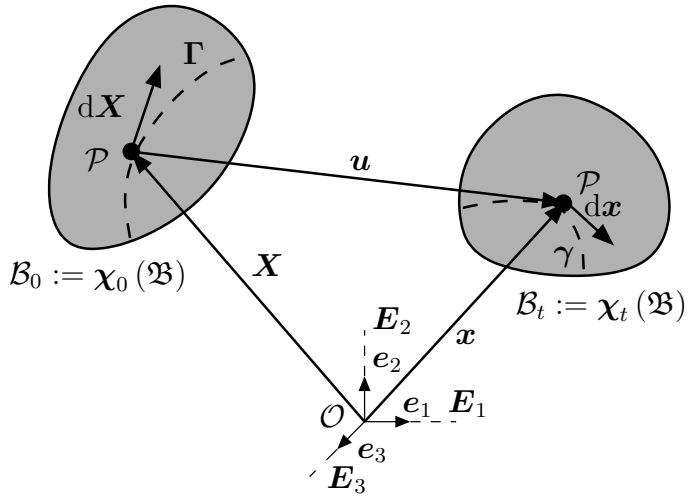

Figure 2.1: Deformation and motion of a material body $\mathfrak{B}$.

The displacement vector $\boldsymbol{u}\,(t)$ of point $\mathcal{P}$ at time t displayed in figure 2.1 is defined as

$$\boldsymbol{u} = \boldsymbol{x} - \boldsymbol{X} \quad . \tag{2.6}$$

The velocity $\boldsymbol{v}$ and acceleration $\boldsymbol{a}$ of this point can be expressed in terms of $\boldsymbol{x}$ by differentiating $\boldsymbol{u}$ with respect to time $\dot{(\cdot)} = \frac{\mathrm{d}}{\mathrm{d}t}(\cdot)$, $\ddot{(\cdot)} = \frac{\mathrm{d}^2}{\mathrm{d}t^2}(\cdot)$

$$\boldsymbol{v} = \frac{\mathrm{d}\boldsymbol{u}}{\mathrm{d}t} = \frac{\mathrm{d}\boldsymbol{x}}{\mathrm{d}t} = \dot{\boldsymbol{u}} = \dot{\boldsymbol{x}} \quad , \quad \boldsymbol{a} = \frac{\mathrm{d}\boldsymbol{v}}{\mathrm{d}t} = \frac{\mathrm{d}^2\boldsymbol{x}}{\mathrm{d}t^2} = \ddot{\boldsymbol{x}} \quad . \tag{2.7}$$

In order to determine the distortion of each material point $\mathcal{P}$, rotations and strains are evaluated in an infinitely small domain around the point $\mathcal{P}$. Consider that the position vector $\boldsymbol{X}$ lies on the material line $\boldsymbol{\Gamma}\,(s)$ in the material description and the position vector $\boldsymbol{x}$ lies on the same material line $\boldsymbol{\gamma}\,(s)$ in the spatial description, where s denotes the parametrization of the line. Differentiating both line descriptions with respect to s and following the material line with an infinitesimal increment $\mathrm{d}s$

$$\mathrm{d}\boldsymbol{X} = \frac{\partial \boldsymbol{\Gamma}}{\partial s}\,\mathrm{d}s \quad , \quad \mathrm{d}\boldsymbol{x} = \frac{\partial \boldsymbol{\gamma}}{\partial s}\,\mathrm{d}s \quad , \tag{2.8}$$

results in the material tangent vector $\mathrm{d}\boldsymbol{X}$, and the spatial tangent vector $\mathrm{d}\boldsymbol{x}$. Following HAUPT (2002) and plugging $\boldsymbol{\gamma}$ into (2.3), with $\boldsymbol{x} = \boldsymbol{\gamma}$ and differentiating with respect to s results in

$$\frac{\partial \boldsymbol{\gamma}}{\partial s} = \frac{\partial \boldsymbol{x}}{\partial s} = \frac{\partial \boldsymbol{\chi}_t(\boldsymbol{\Gamma})}{\partial s} = \frac{\partial \boldsymbol{\Gamma}}{\partial s} \frac{\boldsymbol{\chi}_t(\boldsymbol{\Gamma})}{\partial \boldsymbol{\Gamma}} \quad . \tag{2.9}$$

Applying (2.9) to (2.8) results in the material gradient of motion, or deformation gradient, $\boldsymbol{F}$

$$\boldsymbol{F} = \frac{\partial x_i}{\partial X_J}\, \boldsymbol{e}_i \otimes \boldsymbol{E}_J = F_{iJ}\, \boldsymbol{e}_i \otimes \boldsymbol{E}_J \quad . \tag{2.10}$$

Equation (2.10) denotes that the components F_{iJ} are identical to the elements of the JACOBI matrix and refer to the spatial basis $\boldsymbol{e}_i$ as well as to the material basis $\boldsymbol{E}_J$. Hence, the non-singular two-point tensor $\boldsymbol{F}$ linearly maps the material tangent vector $\mathrm{d}\boldsymbol{X}$ onto the spatial tangent vector $\mathrm{d}\boldsymbol{x}$

$$\mathrm{d}\boldsymbol{x} = \boldsymbol{F} \cdot \mathrm{d}\boldsymbol{X} \quad , \tag{2.11}$$

and thus describes the rotations and stretches of the material point $\mathcal{P}$. $\boldsymbol{F}$ can be uniquely decomposed into a pure rotation tensor $\boldsymbol{R}$, the left stretch tensor $\mathbf{v}$ and the right stretch tensor $\boldsymbol{U}$

$$\begin{aligned} F_{iJ}\, \boldsymbol{e}_i \otimes \boldsymbol{E}_J = \boldsymbol{R} \cdot \boldsymbol{U} &= R_{iK}\, U_{KJ}\, \boldsymbol{e}_i \otimes \boldsymbol{E}_J \\ &= \mathbf{v} \cdot \boldsymbol{R} = \mathrm{v}_{ik}\, R_{kJ}\, \boldsymbol{e}_i \otimes \boldsymbol{E}_J \end{aligned} \quad . \tag{2.12}$$

The proper orthogonal rotation tensor $\boldsymbol{R}$, i.e. $\boldsymbol{R}^{-1} = \boldsymbol{R}^{\mathrm{T}}$ and $\det(\boldsymbol{R}) = 1$, describes the rotation from $\mathrm{d}\boldsymbol{X}$ to $\mathrm{d}\boldsymbol{x}$ and consequently depends on the spatial as well as on the material basis. The symmetric, positive definite stretch tensors $\mathbf{v}$ and $\boldsymbol{U}$ only depend on one of the basis. The spectral decomposition of the stretch tensors, the deformation gradient and the rotation tensor follows

$$\begin{aligned} \mathbf{v} &= \sum_{i=1}^{3} \lambda_i\, \boldsymbol{n}_i \otimes \boldsymbol{n}_i \quad , \quad \boldsymbol{U} = \sum_{i=1}^{3} \lambda_i\, \boldsymbol{N}_i \otimes \boldsymbol{N}_i \quad , \\ \boldsymbol{F} &= \sum_{i=1}^{3} \lambda_i\, \boldsymbol{n}_i \otimes \boldsymbol{N}_i \quad , \quad \boldsymbol{R} = \sum_{i=1}^{3} \boldsymbol{n}_i \otimes \boldsymbol{N}_i \quad . \end{aligned} \tag{2.13}$$

Here, the eigenvalues λ_i are the principal stretches and $\boldsymbol{N}_i$, $\boldsymbol{n}_i$ are the eigenvectors in the material and spatial description respectively.
Differentiating $\boldsymbol{F}$ with respect to time results in the material deformation velocity gradient $\dot{\boldsymbol{F}}$ and its transformation to the spatial configuration to the spatial deformation velocity gradient $\boldsymbol{\ell}$

$$\dot{\boldsymbol{F}} = \frac{\partial \dot{\boldsymbol{x}}}{\partial \boldsymbol{X}} \quad , \quad \boldsymbol{\ell} = \frac{\partial \dot{\boldsymbol{x}}}{\partial \boldsymbol{x}} = \dot{\boldsymbol{F}} \cdot \boldsymbol{F}^{-1} \quad . \tag{2.14}$$

The deformation gradient itself only maps line elements as tangent vectors, but it can be used in NANSON's formula to map infinitesimal surface elements from the material to the spatial configuration

$$\boldsymbol{n}\, \mathrm{d}a = \det(\boldsymbol{F})\ \boldsymbol{F}^{-\mathrm{T}} \cdot \boldsymbol{N}\, \mathrm{d}A \quad . \tag{2.15}$$

Here, $\mathrm{d}a$, $\mathrm{d}A$ denote the infinitesimal surface areas, $\boldsymbol{n}$, $\boldsymbol{N}$ the surface normals in the material and the spatial configuration respectively. The determinant of the JACOBIan matrix, often referred to as $J = \det(\boldsymbol{F})$ with $J > 0$, transforming an infinitesimal material volume element $\mathrm{d}V$ onto an infinitesimal spatial volume element $\mathrm{d}v$

$$\mathrm{d}v = \det(\boldsymbol{F})\ \mathrm{d}V \quad . \tag{2.16}$$

Strains

As previously shown, the material deformation gradient $\boldsymbol{F}$ describes the change of shape and orientation of an infinitesimal line element. Hence, this measure still includes rigid body motions, namely rotations, and thus cannot be used as strain measurement. The difference of the norm of the material and the spatial tangent vector is independent of rotations

$$\begin{aligned} ||\mathrm{d}\boldsymbol{x}||_2^2 - ||\mathrm{d}\boldsymbol{X}||_2^2 &= \mathrm{d}\boldsymbol{x}\cdot\mathrm{d}\boldsymbol{x} - \mathrm{d}\boldsymbol{X}\cdot\mathrm{d}\boldsymbol{X} \\ &= (\boldsymbol{F}\cdot\mathrm{d}\boldsymbol{X})\cdot(\boldsymbol{F}\cdot\mathrm{d}\boldsymbol{X}) - \mathrm{d}\boldsymbol{X}\cdot\boldsymbol{1}\cdot\mathrm{d}\boldsymbol{X} \\ &= \mathrm{d}\boldsymbol{X}\cdot\left(\boldsymbol{F}^{\mathrm{T}}\cdot\boldsymbol{F} - \boldsymbol{1}\right)\cdot\mathrm{d}\boldsymbol{X} \\ &= \mathrm{d}\boldsymbol{X}\cdot(\boldsymbol{C} - \boldsymbol{1})\cdot\mathrm{d}\boldsymbol{X} \\ &= \mathrm{d}\boldsymbol{X}\cdot 2\,\boldsymbol{E}\cdot\mathrm{d}\boldsymbol{X} \quad , \end{aligned} \tag{2.17}$$

which results in the GREEN - LAGRANGE strain tensor $\boldsymbol{E} = \frac{1}{2}\left(\boldsymbol{F}^{\mathrm{T}}\cdot\boldsymbol{F} - \boldsymbol{1}\right) = \frac{1}{2}(\boldsymbol{C} - \boldsymbol{1})$. Since the right CAUCHY - GREEN tensor $\boldsymbol{C} = \boldsymbol{F}^{\mathrm{T}}\cdot\boldsymbol{F} = \boldsymbol{U}\cdot\boldsymbol{U}$ is independent of the rotation tensor $\boldsymbol{R}$, the GREEN - LAGRANGE strain tensor is an appropriate strain measure referring to the material description. Observing the same strain measure in the spatial coordinate system results in the EULER - ALMANSI strain tensor $\boldsymbol{e}$

$$\begin{aligned} ||\mathrm{d}\boldsymbol{x}||_2^2 - ||\mathrm{d}\boldsymbol{X}||_2^2 &= \mathrm{d}\boldsymbol{x}\cdot\mathrm{d}\boldsymbol{x} - \mathrm{d}\boldsymbol{X}\cdot\mathrm{d}\boldsymbol{X} \\ &= \mathrm{d}\boldsymbol{x}\cdot\boldsymbol{1}\cdot\mathrm{d}\boldsymbol{x} - \left(\boldsymbol{F}^{-1}\cdot\mathrm{d}\boldsymbol{x}\right)\cdot\left(\boldsymbol{F}^{-1}\cdot\mathrm{d}\boldsymbol{x}\right) \\ &= \mathrm{d}\boldsymbol{x}\cdot\left(\boldsymbol{1} - \boldsymbol{F}^{-\mathrm{T}}\cdot\boldsymbol{F}^{-1}\right)\cdot\mathrm{d}\boldsymbol{x} \\ &= \mathrm{d}\boldsymbol{x}\cdot\left(\boldsymbol{1} - \boldsymbol{b}^{-1}\right)\cdot\mathrm{d}\boldsymbol{x} \\ &= \mathrm{d}\boldsymbol{x}\cdot 2\,\boldsymbol{e}\cdot\mathrm{d}\boldsymbol{x} \quad . \end{aligned} \tag{2.18}$$

Here, $\boldsymbol{b} = \boldsymbol{F}\cdot\boldsymbol{F}^{\mathrm{T}} = \mathbf{v}\cdot\mathbf{v}$ denotes the left CAUCHY - GREEN tensor, which is independent of rigid body motions, as is the right CAUCHY - GREEN tensor. Consequently the EULER - ALMANSI strain tensor $\boldsymbol{e} = \frac{1}{2}\left(\boldsymbol{1} - \boldsymbol{F}^{-\mathrm{T}}\cdot\boldsymbol{F}^{-1}\right) = \frac{1}{2}\left(\boldsymbol{1} - \boldsymbol{b}^{-1}\right)$ does not depend on $\boldsymbol{R}$. Linearizing $\boldsymbol{E}$ and $\boldsymbol{e}$ around $\boldsymbol{u} = \boldsymbol{0} \Leftrightarrow \boldsymbol{x} = \boldsymbol{X}$ results in the same linearized strain tensor $\boldsymbol{\varepsilon}$

$$\boldsymbol{\varepsilon} = \mathrm{LIN}\left[\boldsymbol{E}\right]\big|_{\boldsymbol{u}=\boldsymbol{0}} = \mathrm{LIN}\left[\boldsymbol{e}\right]\big|_{\boldsymbol{u}=\boldsymbol{0}} = \frac{1}{2}\left(\frac{\partial\boldsymbol{u}}{\partial\boldsymbol{X}} + \left(\frac{\partial\boldsymbol{u}}{\partial\boldsymbol{X}}\right)^{\mathrm{T}}\right) \quad . \tag{2.19}$$

Neglecting the second derivatives with respect to $\boldsymbol{X}$ in $\boldsymbol{E}$ and $\boldsymbol{x}$ in $\boldsymbol{e}$ respectively, leads to the linearized strain tensor $\boldsymbol{\varepsilon}$ used as strain measure in the small strain theory.

2.2 Stresses

Consider a stretched body $\mathfrak{B}$, occupying the space $\mathcal{B}_t$ at time t in the spatial description. Cutting the body along a plane induces a force $\mathrm{d}\boldsymbol{f}$ on the sliced surface element $\mathrm{d}a$ with its outward normal $\boldsymbol{n}$, as depicted in figure 2.2. The surface traction $\boldsymbol{t}$ is defined as force per area $\boldsymbol{t} = \mathrm{d}\boldsymbol{f}/\mathrm{d}a$.
On the counterpart of the body, the same force in the opposite direction on the corresponding surface element exerts, to fulfill NEWTON's third law of action and reaction, which is also known as free-body principle by EULER as explained by SZABÓ (1987): Both parts are in equilibrium, i.e. $\boldsymbol{t}(\boldsymbol{n}) = -\boldsymbol{t}(-\boldsymbol{n})$.

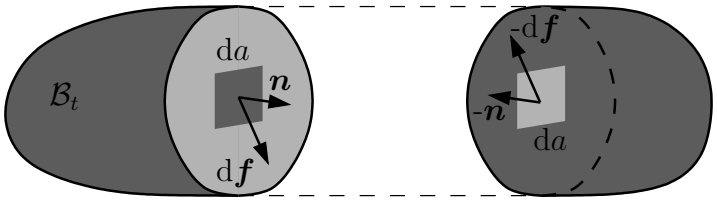

Figure 2.2: Deformed body cut by a plane with its normal $\boldsymbol{n}$.

According to CAUCHY's stress theorem, the surface traction $\boldsymbol{t}$ is defined by the outward normal $\boldsymbol{n}$ and the so-called CAUCHY stress tensor $\boldsymbol{\sigma}$

$$\boldsymbol{t} = \boldsymbol{\sigma} \cdot \boldsymbol{n} \quad . \tag{2.20}$$

Hence, the stretching of a body induces stresses inside the body. Since $\boldsymbol{n}$, $\mathrm{d}a$ and $\boldsymbol{t}$ are defined in spatial coordinates, the stress tensor $\boldsymbol{\sigma}$ is completely defined in these bases as well. Due to conservation of angular momentum, one can show that $\boldsymbol{\sigma}$ is a symmetric tensor, i.e. $\boldsymbol{\sigma} = \boldsymbol{\sigma}^{\mathrm{T}}$. Applying NANSON's formula (2.15) on the surface element $\boldsymbol{n}\,\mathrm{d}a$

$$\boldsymbol{t}\,\mathrm{d}a = \boldsymbol{\sigma} \cdot \boldsymbol{n}\,\mathrm{d}a = J\,\boldsymbol{\sigma} \cdot \boldsymbol{F}^{-\mathrm{T}}\,\boldsymbol{N}\,\mathrm{d}A = \boldsymbol{P} \cdot \boldsymbol{N}\,\mathrm{d}A \quad , \tag{2.21}$$

leads to the 1st PIOLA - KIRCHHOFF stress tensor $\boldsymbol{P} = J\,\boldsymbol{\sigma} \cdot \boldsymbol{F}^{-\mathrm{T}}$, which is an unsymmetric, two-point tensor: This stress tensor relates spatial tractions $\boldsymbol{t}$ to material surface elements $\boldsymbol{N}\,\mathrm{d}A$, such that $\boldsymbol{P}$ refers to the spatial as well as to the material bases. To overcome the inconvenience of an unsymmetric stress tensor, the 2nd PIOLA - KIRCHHOFF stress tensor $\boldsymbol{S}$

$$\boldsymbol{S} = \boldsymbol{F}^{-1} \cdot \boldsymbol{P} = J\,\boldsymbol{F}^{-1} \cdot \boldsymbol{\sigma} \cdot \boldsymbol{F}^{-\mathrm{T}} \quad , \tag{2.22}$$

is often applied. Due to the symmetry of $\boldsymbol{\sigma}$, $\boldsymbol{S}$ is symmetric and furthermore refers completely to the material bases. Unfortunately this stress measure has no direct physical meaning.

2.3 Balance laws

Balance laws form a set of equalities and inequalities valid for fluids and solids, and thus they balance the most important physical measures. In continuum solid mechanics the focus is

set on the conservation of mass, conservation of linear and angular momentum, conservation of energy as well as entropy inequality. In order to fulfill these laws, they are considered in the required constitutive model. For purely linear elastic mechanical systems as considered in this work, the conservation of energy is not an additional statement but a consequence of the conservation of linear momentum. However, as the theory of linear elastic fracture mechanics is based on conservation of energy, it is briefly discussed here. All balance laws are valid in integral or global form, i.e. for the material body $\mathfrak{B}$, as well as for each material point $\mathcal{P}$ known as the local form, independent of the chosen coordinate system.

Conservation of mass

In continuum solid mechanics the mass m of a body $\mathfrak{B}$ can be considered as constant in time. A material point $\mathcal{P}$ has the mass density $\rho = \rho(\boldsymbol{x}, t)$ in the spatial, and the mass density $\rho_0 = \rho(\boldsymbol{X})$ in the material system. With

$$\mathrm{d}m = \rho \,\mathrm{d}v = \rho_0 \,\mathrm{d}V \quad \Leftrightarrow \quad \frac{\mathrm{d}v}{\mathrm{d}V} = \frac{\rho_0}{\rho} = J \quad , \tag{2.23}$$

and (2.16) the conservation of mass follows

$$\frac{\mathrm{d}}{\mathrm{d}t} m = 0 = \frac{\mathrm{d}}{\mathrm{d}t} \int_{\mathcal{B}_t} \rho \,\mathrm{d}v = \frac{\mathrm{d}}{\mathrm{d}t} \int_{\mathcal{B}_0} \rho \, J \,\mathrm{d}V = \int_{\mathcal{B}_0} \dot{\rho} \, J + \rho \, \dot{J} \,\mathrm{d}V \quad . \tag{2.24}$$

With the derivative $\dot{J} = J \operatorname{div}(\dot{\boldsymbol{x}})$, the conservation of mass for a body yields

$$\frac{\mathrm{d}}{\mathrm{d}t} m = 0 = \int_{\mathcal{B}_0} \left(\dot{\rho} + \rho \operatorname{div}(\dot{\boldsymbol{x}})\right) \, J \,\mathrm{d}V = \int_{\mathcal{B}_t} \dot{\rho} + \rho \operatorname{div}(\dot{\boldsymbol{x}}) \,\mathrm{dv} \quad . \tag{2.25}$$

For an arbitrary volume (2.25) follows

$$\dot{\rho} + \rho \operatorname{div}(\dot{\boldsymbol{x}}) = 0 \quad . \tag{2.26}$$

Conservation of linear and angular momentum

The linear momentum $\boldsymbol{I}$ of a body $\mathfrak{B}$ is defined by

$$\boldsymbol{I} = \int_{\mathcal{B}_t} \rho \, \dot{\boldsymbol{x}} \,\mathrm{d}v \quad . \tag{2.27}$$

Its time derivative is equal to all external forces, i.e. traction $\boldsymbol{t}$ acting on the surface $\partial\mathcal{B}_t$ and volume forces $\boldsymbol{f} = \rho \, \boldsymbol{b}$ acting on the volume of a body $\mathcal{B}_t$

$$\frac{\mathrm{d}}{\mathrm{d}t} \int_{\mathcal{B}_t} \rho \, \dot{\boldsymbol{x}} \,\mathrm{d}v = \int_{\mathcal{B}_t} \rho \, \boldsymbol{b} \,\mathrm{d}v + \int_{\partial\mathcal{B}_t} \boldsymbol{t} \,\mathrm{d}a \quad , \tag{2.28}$$

which is NEWTON's second law of motion for continuous bodies. Applying CAUCHY's stress theorem (2.20), the conservation of mass (2.25) and the divergence theorem, the balance of linear momentum yields

$$\int_{\mathcal{B}_t} \left(\operatorname{div}(\boldsymbol{\sigma}) + \boldsymbol{f} - \rho \, \ddot{\boldsymbol{x}}\right) \,\mathrm{d}v = \boldsymbol{0} \quad , \tag{2.29}$$

for a body, and

$$\operatorname{div}(\boldsymbol{\sigma}) + \boldsymbol{f} = \rho\,\ddot{\boldsymbol{x}} \quad , \tag{2.30}$$

for an arbitrary volume. When considering statics, the acceleration field $\ddot{\boldsymbol{x}} = \boldsymbol{0}$ and thus the inertia term $\rho\,\ddot{\boldsymbol{x}}$ vanishes, which simplifies (2.29) and (2.30).
The time derivative of the angular momentum $\boldsymbol{L}$

$$\boldsymbol{L} = \int_{\mathcal{B}_t} \rho\,(\boldsymbol{x} - \boldsymbol{x}_0) \times \dot{\boldsymbol{x}}\,\mathrm{d}v \quad , \tag{2.31}$$

is equal to all external moments around an arbitrary point $\boldsymbol{x}_0$

$$\frac{\mathrm{d}}{\mathrm{d}t}\int_{\mathcal{B}_t} \rho\,(\boldsymbol{x} - \boldsymbol{x}_0) \times \dot{\boldsymbol{x}}\,\mathrm{d}v = \int_{\mathcal{B}_t} \rho\,((\boldsymbol{x} - \boldsymbol{x}_0) \times \boldsymbol{b})\,\mathrm{d}v + \int_{\partial\mathcal{B}_t} ((\boldsymbol{x} - \boldsymbol{x}_0) \times \boldsymbol{t})\,\mathrm{d}a \quad . \tag{2.32}$$

Applying CAUCHY's stress theorem (2.20), the balance of linear momentum (2.30) and the divergence theorem, the balance of angular momentum follows

$$\boldsymbol{\sigma} = \boldsymbol{\sigma}^{\mathrm{T}} \quad . \tag{2.33}$$

Conservation of energy

The first law of thermodynamics states that the energy in a closed system remains constant. The energy E of a body

$$E = K + U \quad , \tag{2.34}$$

depends on the kinetic energy K

$$K = \int_{\mathcal{B}_t} \frac{1}{2}\,\rho\,\dot{\boldsymbol{x}} \cdot \dot{\boldsymbol{x}}\,\mathrm{d}v \quad , \tag{2.35}$$

and the sum of the initial strain and thermal energy, called the internal energy U

$$U = \int_{\mathcal{B}_t} u\,\rho\,\mathrm{d}v \quad , \tag{2.36}$$

where u is the specific internal energy. The change of energy E in time

$$\frac{\mathrm{d}}{\mathrm{d}t}\,E = P + Q \quad , \tag{2.37}$$

is equal to the mechanical power P

$$P = \int_{\mathcal{B}_t} \rho\,\boldsymbol{b} \cdot \dot{\boldsymbol{x}}\,\mathrm{d}v + \int_{\partial\mathcal{B}_t} \boldsymbol{t} \cdot \dot{\boldsymbol{x}}\,\mathrm{d}a \quad , \tag{2.38}$$

and the thermal power supply Q

$$\begin{aligned} Q &= \int_{\mathcal{B}_t} \rho\,r\,\mathrm{d}v + \int_{\partial\mathcal{B}_t} q\,\mathrm{d}a \\ &= \int_{\mathcal{B}_t} \rho\,r\,\mathrm{d}v - \int_{\partial\mathcal{B}_t} \boldsymbol{q} \cdot \boldsymbol{n}\,\mathrm{d}a \end{aligned} \quad , \tag{2.39}$$

where $\rho\, r = \rho\,(\boldsymbol{x}, t) \cdot r\,(\boldsymbol{x}, t)$ is the internal heat source and $q = q\,(\boldsymbol{x}, t, \boldsymbol{n})$ is the heat flux density field depending on the outward normal $\boldsymbol{n} = \boldsymbol{n}\,(\boldsymbol{x}, t)$ of the surface $\partial\mathcal{B}_t$. Rewriting the heat flux density field q in terms of the CAUCHY heat flux vector $\boldsymbol{q} = \boldsymbol{q}\,(\boldsymbol{x}, t)$ and the outward normal $\boldsymbol{n}$, results in the second line of (2.39). Hence, a change in the mechanical power or heat supply directly effects a change of the kinetic and internal energy in time

$$\begin{aligned} \frac{\mathrm{d}}{\mathrm{d}t}\,(K + U) &= P + Q \quad , \\ \frac{\mathrm{d}}{\mathrm{d}t} \int_{\mathcal{B}_t} \rho \left(\frac{1}{2}\, \dot{\boldsymbol{x}} \cdot \dot{\boldsymbol{x}} + u \right) \mathrm{d}v &= \int_{\mathcal{B}_t} \rho\, (\boldsymbol{b} \cdot \dot{\boldsymbol{x}} + r)\, \mathrm{d}v + \int_{\partial\mathcal{B}_t} \boldsymbol{t} \cdot \dot{\boldsymbol{x}} - \boldsymbol{q} \cdot \boldsymbol{n}\, \mathrm{d}a \quad . \end{aligned} \tag{2.40}$$

Applying CAUCHY's stress theorem (2.20), the balance of linear momentum (2.30) and the divergence theorem to (2.40), the conservation of energy of a body yields

$$\int_{\mathcal{B}_t} \rho\, \dot{u}\, \mathrm{d}v = \int_{\mathcal{B}_t} \rho\, r + \boldsymbol{\sigma} : \boldsymbol{\ell} - \operatorname{div}(\boldsymbol{q})\, \mathrm{d}v \quad . \tag{2.41}$$

For an arbitrary volume the conservation of energy follows

$$\rho\, \dot{u} = \rho\, r + \boldsymbol{\sigma} : \boldsymbol{\ell} - \operatorname{div}(\boldsymbol{q}) \quad . \tag{2.42}$$

The value $\int_{\mathcal{B}_t} \boldsymbol{\sigma} : \boldsymbol{\ell}\, \mathrm{d}v$ is also known as the stress or physical power $\dot{\Psi}$. Besides the CAUCHY stress tensor $\boldsymbol{\sigma}$ and spatial deformation velocity gradient $\boldsymbol{\ell}$, the physical power can be rewritten in terms of other work conjugate pairings

$$\boldsymbol{\sigma} : \boldsymbol{\ell} = J^{-1}\, \boldsymbol{P} : \dot{\boldsymbol{F}} = J^{-1}\, \boldsymbol{S} : \dot{\boldsymbol{E}} \quad . \tag{2.43}$$

Entropy inequaltity

The second law of thermodynamics, or the CLAUSIUS - DUHEM inequality, provides information about the processes direction. In contrast to the previously mentioned balance principles, the entropy s is not a conserved quantity but restricted: The entropy production is never negative and depends on the heat flux density field q, the internal heat source $\rho\, r$ and the absolute temperature field $\Theta = \Theta\,(\boldsymbol{x}, \mathrm{t})$.

$$\frac{\mathrm{d}}{\mathrm{d}t} \int_{\mathcal{B}_t} \rho\, s\, \mathrm{d}v \geq \int_{\mathcal{B}_t} \rho\, \frac{r}{\Theta}\, \mathrm{d}v - \int_{\partial\mathcal{B}_t} \frac{1}{\Theta}\, \boldsymbol{q} \cdot \boldsymbol{n}\, \mathrm{d}a \quad . \tag{2.44}$$

Only in the case of a reversible process is the CLAUSIUS - DUHEM inequality an equation with equal quantities. Applying the free HELMHOLTZ energy $\psi = u - s\,\Theta$, the first law of thermodynamics as well as the divergence theorem to (2.44), the entropy inequality for an arbitrary volume using spatial quantities is as follows

$$-\rho \left(\dot{\psi} + s\, \dot{\Theta} \right) + \boldsymbol{\sigma} : \boldsymbol{\ell} - \frac{1}{\Theta}\, \boldsymbol{q} \cdot \frac{\partial \Theta}{\partial \boldsymbol{x}} \geq 0 \quad . \tag{2.45}$$

Using material quantities, the second law of thermodynamics yields

$$-\rho_0 \left(\dot{\psi} + s\, \dot{\Theta} \right) + \boldsymbol{S} : \dot{\boldsymbol{E}} - \frac{1}{\Theta}\, \boldsymbol{Q} \cdot \frac{\partial \Theta}{\partial \boldsymbol{X}} \geq 0 \quad , \tag{2.46}$$

where $\boldsymbol{Q} = \boldsymbol{Q}(\boldsymbol{X}) = J\,\boldsymbol{F}^{-1} \cdot \boldsymbol{q}$ is referred to as the PIOLA - KIRCHHOFF heat flux vector. If the absolute temperature Θ is constant over the entire deformation process, the process is called isothermal: the free HELMHOLTZ energy is equal to the elastic strain energy density function per unit mass, i.e. $\Psi = \rho\,\psi$. Since the CLAUSIUS - DUHEM inequality always needs to be fulfilled independent of the current deformation, this inequality is taken into account for the development of constitutive equations.

2.4 Material theory

As kinematics and balance laws are not sufficient to determine the unknown field quantities, namely the displacement, temperature, heat flux and stress field, additional equations are required to set up a boundary value problem (BVP). Since isothermal processes are investigated in this work, only the relation between the displacement and the stress field is described in this section.
The material behavior provides the missing set of equations required to solve the BVP and enable the determination of the stress field in terms of the strain field for each material point uniquely in time. The derivation of these equations for different materials as well as their underlying principles can be found in NOLL (1955), TRUESDELL & TOUPIN (1960), TRUESDELL & NOLL (1965), OGDEN (1984), CHADWICK (1999) and HAUPT (2002) among others.

The so-called constitutive equation correlates the process of deformation with the current stress state. These equations depend on the history of deformation or stress or even a combination of both. Knowing the body's motion in advance requires the application of a kinematic constraint to the material model. The assumption of incompressibility, meaning that the volume is preserved ($J = 1$), widely used in rubber elasticity as well as the assumption of a rigid body motion, i.e. all principle stretches are zero ($\lambda_i = 0$), are the most famous kinematic restrictions.

Furthermore the material model has to meet principles to follow the physical observations, of which the most popular are presented here:

Principle of material causality
In a thermomechanical process, the spatial coordinates $\boldsymbol{x} = \boldsymbol{\chi}(\mathcal{P}, t)$ and the temperature field $\Theta = \theta(\mathcal{P}, t)$ are the only independent variables in the system. All other variables are regarded as functions of $\boldsymbol{x}$ and Θ.

Principle of determinism
The current stress field $\boldsymbol{\sigma}(\boldsymbol{x}, \Theta, t)$ can be uniquely determined by the history of a body's motion and temperature.

Principle of local action
The stress in a material point $\mathcal{P}$ depends only on variables in its environment and not on the variables in the whole body.

Principle of material frame-indifference
Principle of material frame-indifference, or principle of material objectivity, states that

the constitutive equation needs to be invariant with respect to the change of the observer.

Principle of material symmetry
The material symmetry states the existence of a rotation tensor $\boldsymbol{Q}^{\star}$, for which the stress response equals, i.e.

$$\boldsymbol{\sigma}\left(\boldsymbol{F}\cdot\boldsymbol{Q}^{\star}\right)=\boldsymbol{\sigma}\left(\boldsymbol{F}\right) \quad . \tag{2.47}$$

In general, the proper orthogonal tensor $\boldsymbol{Q}^{\star}$ cannot be chosen, but it depends on the material itself. If (2.47) holds for arbitrary proper orthogonal tensors $\boldsymbol{Q}^{\star}$, the material is called isotropic: It deforms equally in all directions.

Isotropic elasticity

If the deformation of a body is an isothermal, reversible process, the CLAUSIUS - DUHEM inequality (2.44) reduces to an equality and thus the process is called elastic. Hence, the CAUCHY stress tensor $\boldsymbol{\sigma}$ depends only on the current deformation gradient $\boldsymbol{F}$ at a material point $\mathcal{P}$ at time t: $\boldsymbol{\sigma}=\boldsymbol{\sigma}\left(\boldsymbol{F}\left(\boldsymbol{x},t\right)\right)$.

Isotropic hyperelasticity

An isotropic, elastic body simplifies to a so-called hyperelastic, if the HELMHOLTZ energy $\psi=\psi\left(\boldsymbol{F}\right)$ serves as a potential. Hence, the stress power $\dot{\Psi}$ is independent of the deformation history. Defining the strain energy density function per unit mass as $\Psi=\rho_0\,\psi$, the second law of thermodynamics (2.46) leads to

$$-\dot{\Psi}+\boldsymbol{S}:\dot{\boldsymbol{E}}=0 \quad . \tag{2.48}$$

As the strain energy density Ψ only depends on $\boldsymbol{E}$, the stress power follows

$$\dot{\Psi}=\frac{\partial\Psi}{\partial\boldsymbol{E}}:\dot{\boldsymbol{E}} \quad . \tag{2.49}$$

Thus, the second law of thermodynamics (2.48) yields

$$\left(-\frac{\partial\Psi}{\partial\boldsymbol{E}}+\boldsymbol{S}\right):\dot{\boldsymbol{E}}=0 \quad , \tag{2.50}$$

exhibiting the relation between the 2nd PIOLA - KIRCHHOFF stress tensor $\boldsymbol{S}$, the potential Ψ and the GREEN - LAGRANGE strain tensor $\boldsymbol{E}$

$$\boldsymbol{S}=\frac{\partial\Psi}{\partial\boldsymbol{E}}=2\,\frac{\partial\Psi}{\partial\boldsymbol{C}} \quad , \tag{2.51}$$

for non-trivial solutions $\dot{\boldsymbol{E}}\neq\boldsymbol{0}$. The corresponding fourth order material tensor $\mathbb{C}$ in material coordinates reads

$$\mathbb{C}=\frac{\partial^2\Psi}{\partial\boldsymbol{E}\,\partial\boldsymbol{E}}=4\,\frac{\partial^2\Psi}{\partial\boldsymbol{C}\,\partial\boldsymbol{C}} \quad . \tag{2.52}$$

A similar setup can be derived for other conjugate pairings mentioned in (2.43). Note, before the deformation process ($\lambda_i = 0$), all stresses and strains as well as the strain energy need to vanish. The potential Ψ is furthermore restricted to be polyconvex, as discussed in BALL (1977). This functional might also be given in terms of the principle stretches λ_i or the three basic invariants of $\boldsymbol{C}$, namely $\mathrm{I}_C, \mathrm{II}_C$ and III_C, to define an isotropic hyperelastic material uniquely, as proven in e.g. HAUPT (2002): $\Psi = \Psi(\lambda_1, \lambda_2, \lambda_3)$, $\Psi = \Psi(\mathrm{I}_C, \mathrm{II}_C, \mathrm{III}_C)$. The three basic invariants can be either determined directly from the right CAUCHY - GREEN tensor $\boldsymbol{C}$ or the three principal stretches λ_i.
The choice of the potential depends on the real physical problem. One of the most general strain energy density functions is the OGDEN material, introduced in OGDEN (1972). With a special set of material parameters applied to the OGDEN material, one obtains the MOONEY - RIVLIN material introduced by MOONEY (1940) and RIVLIN (1948). A further simplification in the set of material parameters of the MOONEY - RIVLIN material model results in the potential of the Neo - HOOKEan solid (see e.g. TRELOAR (1943a), TRELOAR (1943b) and FLORY (1961)). In this work isotropic, linear elastic material behavior, i.e. a HOOKEan solid, in context of small displacements and rotations is assumed. The strain energy density in terms of LAMÉ's material constants Λ, μ reads

$$\Psi = \frac{\Lambda}{2} \operatorname{tr}^2(\boldsymbol{\varepsilon}) + \mu \operatorname{tr}\left(\boldsymbol{\varepsilon}^2\right) \quad . \tag{2.53}$$

With (2.51) and the small displacement theory, the CAUCHY stress tensor follows

$$\boldsymbol{\sigma} = \frac{\partial \Psi}{\partial \boldsymbol{\varepsilon}} = 2\,\mu\,\boldsymbol{\varepsilon} + \Lambda \operatorname{tr}(\boldsymbol{\varepsilon})\ \mathbf{1} \quad . \tag{2.54}$$

Applying (2.52) to (2.53) results in the material tensor

$$\mathbb{C} = \frac{\partial^2 \Psi}{\partial \boldsymbol{\varepsilon}\, \partial \boldsymbol{\varepsilon}} = \left[\mu\ (\delta_{ik}\,\delta_{j\ell} + \delta_{i\ell}\,\delta_{jk}) + \Lambda\,\delta_{ij}\,\delta_{k\ell}\right]\ \boldsymbol{e}_i \otimes \boldsymbol{e}_j \otimes \boldsymbol{e}_k \otimes \boldsymbol{e}_\ell \quad , \tag{2.55}$$

with δ_{ij} being the KRONECKER delta

$$\delta_{ij} = \begin{cases} 1 & \text{if} \quad i = j \\ 0 & \text{if} \quad i \neq j \end{cases} \quad . \tag{2.56}$$

Thus, the stress-strain relation for an isotropic, linear elastic solid can be rewritten

$$\boldsymbol{\sigma} = \mathbb{C} : \boldsymbol{\varepsilon} \quad . \tag{2.57}$$

2.5 Weak form of equilibrium

Since the so-called strong form of equilibrium, i.e. the balance of linear momentum (2.30), coupled with the chosen material model and the appropriate kinematics can in general not be solved analytically, numerical approaches are required. Therefore, a formulation of (2.30) by means of one single scalar equation is favorable. Multiplying the continuously differentiable

virtual displacement field $\delta\boldsymbol{u} = \delta\boldsymbol{u}(\boldsymbol{x})$, also known as test function or weighting function, with the balance of linear momentum (2.30)

$$[\operatorname{div}(\boldsymbol{\sigma}) + \boldsymbol{f} - \rho\,\ddot{\boldsymbol{x}}] \cdot \delta\boldsymbol{u} = 0 \quad , \tag{2.58}$$

and integrating over the domain $\mathcal{B}_t$ yields the weighted residuals

$$\int_{\mathcal{B}_t} [\operatorname{div}(\boldsymbol{\sigma}) + \boldsymbol{f} - \rho\,\ddot{\boldsymbol{x}}] \cdot \delta\boldsymbol{u}\,\mathrm{d}v = 0 \quad . \tag{2.59}$$

Integrating by parts and applying the divergence theorem as well as the CAUCHY theorem to (2.59) results in the weak form of equilibrium

$$\int_{\mathcal{B}_t} \rho\,\ddot{\boldsymbol{x}} \cdot \delta\boldsymbol{u}\,\mathrm{d}v + \int_{\mathcal{B}_t} \boldsymbol{\sigma} : \nabla\delta\boldsymbol{u}\,\mathrm{d}v = \int_{\mathcal{B}_t} \boldsymbol{f} \cdot \delta\boldsymbol{u}\,\mathrm{d}v + \int_{\partial\mathcal{B}_{t\sigma}} \overline{\boldsymbol{t}} \cdot \delta\boldsymbol{u}\,\mathrm{d}a \quad . \tag{2.60}$$

The virtual displacement vector $\delta\boldsymbol{u}$ needs to vanish on DIRICHLET boundaries $\partial\mathcal{B}_{tu}$, as the displacements are prescribed there: $\delta\boldsymbol{u} = \boldsymbol{0}$ and $\boldsymbol{u} = \overline{\boldsymbol{u}}$ on $\partial\mathcal{B}_{tu}$. In contrast to DIRICHLET boundaries, the weak form of balance of linear momentum still needs to be solved for the displacement field on NEUMANN boundaries $\partial\mathcal{B}_{t\sigma}$, on which tractions $\overline{\boldsymbol{t}}$ are prescribed: $\boldsymbol{t} = \boldsymbol{\sigma} \cdot \boldsymbol{n} = \overline{\boldsymbol{t}}$. With these boundary conditions the weak form of equilibrium can be solved for the body.

As in this work linear elastic, isotropic material behavior, as well as small displacements and rotations are assumed, the corresponding stress strain relation (2.57), (2.89) and strain displacement relation (2.19) are applied to the weak form (2.60). Furthermore, the acceleration vanishes $\ddot{\boldsymbol{x}} = \boldsymbol{0}$, as only quasi-static problems are investigated.

2.6 Linear elastic fracture mechanics

The phenomenon of fracture is the local splitting of a body in two or more pieces. Hence, additional internal traction free boundaries occur during the deformation process, which require special treatment in the concept of continuum solid mechanics. Assuming homogeneous, isotropic, linear elastic material behavior in this work, only the main aspects of linear elastic fracture mechanics (LEFM) in context of isotropy and homogeneity are introduced here. The interested reader is referred to ANDERSON (2005), GROSS & SEELIG (2007) among others, for additional information about fracture mechanics.

The mathematical solution for an elliptical internal boundary in an infinite plate is shown by INGLIS (1913), who extended the solution for an infinite plate with a circular hole by KIRSCH (1898). An improvement of the crack shape and the resulting stress and displacement field was made by WESTERGAARD (1939), assuming a crack as a slit instead of an elliptical hole. In the vicinity of the crack tip, the stress field blows up to infinity: The components of the stress tensor depend mostly on the distance r to the crack tip: $\sigma_{ij} \propto r^{-\frac{1}{2}}$. Changing the internal boundary condition from a traction free slit into a traction free notch with an opening angle α, results in a different order of singularity in the stress field in the vicinity of the notch as observed by WILLIAMS (1952): $\sigma_{ij} \propto r^{\lambda(\alpha)-1}$, with $\frac{1}{2} \leq \lambda(\alpha) \leq 1$. For $\alpha = 0$, i.e. a slit, the solution by WESTERGAARD is obtained with $\lambda = \frac{1}{2}$. Assuming $\alpha = \pi$, i.e. the notch degenerates into a straight boundary, the components of the stress tensor do not depend on r anymore, as $\lambda = 1$.

Balance of energy

The crack extension about an infinitesimal increment $\mathrm{d}A$ leads to the dissipation of energy, the energy release rate $\mathcal{G}$

$$\mathcal{G} = -\frac{\mathrm{d}\Pi}{\mathrm{d}A} \quad , \tag{2.61}$$

with overall potential $\Pi = \Pi^i + \Pi^e$ being the sum of the internal potential Π^i, or strain energy, and the potential of the external loads Π^e. Following GRIFFITH (1921), the extension of a crack requires a certain amount of effective fracture surface energy $\mathit{\Gamma}$ to create the additional crack surface A

$$\mathit{\Gamma} = \gamma\, A \quad , \tag{2.62}$$

with γ being the fracture surface energy density. This extra energy term effects the conservation law (2.40), such that the first law of thermodynamics reads

$$\frac{\mathrm{d}}{\mathrm{d}t}\left(K + U + \mathit{\Gamma}\right) = Q + P \quad . \tag{2.63}$$

As GRIFFITH assumes a fracture process zone A_p in the vicinity of a crack tip, the conservation of energy for this process zone follows

$$\dot{\mathit{\Gamma}} = -\hat{P} \quad , \tag{2.64}$$

while the mechanical power $\hat{P}$ is the transport of energy into the process zone

$$\hat{P} = \int_{A_p} \boldsymbol{t} \cdot \dot{\boldsymbol{x}}\, \mathrm{d}a \quad . \tag{2.65}$$

During material debonding, the tractions $\boldsymbol{t}$ vanish over time, as the created internal boundary remains traction free, which leads to a smooth dissipation of energy in time. Integration yields the required mechanical work $\mathrm{d}W = \hat{P}\,\mathrm{d}t$ to perform crack propagation of an increment $\mathrm{d}A$. As two crack surfaces appear during the propagation process, namely $\mathrm{d}A^+$ and $\mathrm{d}A^-$, the required incremental surface energy follows

$$\mathrm{d}\mathit{\Gamma} = \dot{\mathit{\Gamma}}\,\mathrm{d}t = 2\,\gamma\,\mathrm{d}A \quad . \tag{2.66}$$

Assuming a quasi-static, isothermal process, the kinetic energy K and the thermal power supply Q vanish. With $\dot{\Pi}^i\,\mathrm{d}t = \mathrm{d}\Pi^i$, $\dot{\mathit{\Gamma}}\,\mathrm{d}t = \mathrm{d}\mathit{\Gamma}$ and $P\,\mathrm{d}t = -\mathrm{d}\Pi^e$, the balance of energy (2.63) reads

$$\frac{\mathrm{d}\Pi}{\mathrm{d}A} + \frac{\mathrm{d}\mathit{\Gamma}}{\mathrm{d}A} = 0 \quad . \tag{2.67}$$

Applying equations (2.61), (2.66) to equation (2.67) and replacing the material constants $2\,\gamma$ with the material specific fracture toughness $\mathcal{G}_c$, the GRIFFITH criterion for fracture follows

$$\mathcal{G} \geq \mathcal{G}_c \quad , \tag{2.68}$$

i.e. the crack propagates if the condition is fulfilled. The energy release rate in LEFM is often referred to as material force or configurational force, acting on the singularity as described in ESHELBY (1951).

Crack loading conditions

The GRIFFITH criterion for LEFM states the stability of the current system, which can be directly related to the displacement field around the crack tip. Three different crack movements are distinguished, as illustrated in figure 2.3:

- Mode I describes a pure opening of the crack front, with the displacement jump perpendicular to the crack face (figure 2.3(a)).
- The second mode, depicted in figure 2.3(b), is a pure shearing mode: The displacement jump is in plane with the crack face and perpendicular to the crack front.
- Figure 2.3(c) shows the second shearing mode, namely mode III, with the displacement jump parallel to the crack front and in plane with the crack face.

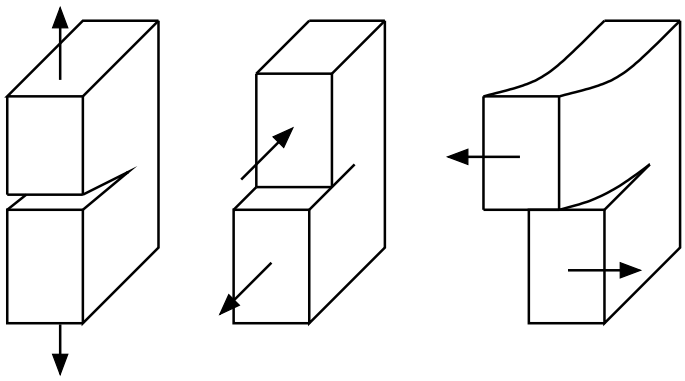

(a) Mode I (b) Mode II (c) Mode III

Figure 2.3: Crack loading conditions.

In general, the displacement field is a combination of all three modes depending on the boundary conditions and the material constants as well as the crack geometry. With the introduction of the so-called stress intensity factors (SIFs), namely K_{I}, K_{II} and K_{III}, by IRWIN (1957), the displacement field in the vicinity of a crack tip can be determined. The SIFs describe the intensity of how a crack deforms in a respective mode, but only in the vicinity of the crack tip, in the K-dominated domain.

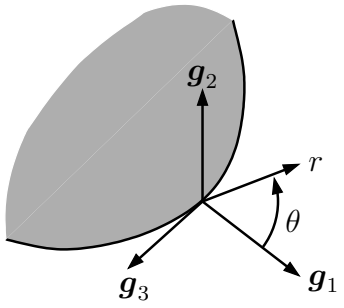

Figure 2.4: Local coordinate system at crack front.

The displacement field in the K-dominated domain, in terms of the SIFs for arbitrary crack configurations, is described in a local coordinate system $\boldsymbol{g}_i$ which is displayed in figure 2.4 with $\boldsymbol{g}_i \cdot \boldsymbol{g}_j = \delta_{ij}$. The vectors $\boldsymbol{g}_1$ and $\boldsymbol{g}_3$ are in plane with the crack, with $\boldsymbol{g}_3$ being the tangent, while $\boldsymbol{g}_2$ is perpendicular to the crack. The displacement field $\boldsymbol{u} = u_i\,\boldsymbol{g}_i$, given in polar coordinates in the $\boldsymbol{g}_1$-$\boldsymbol{g}_2$ plane, in the vicinity of the crack front containing the first order analytical solution by WESTERGAARD yields

$$\begin{aligned}
u_1 &= \frac{K_{\mathrm{I}}}{2\,\mu}\sqrt{\frac{r}{2\,\pi}}\,\cos\left(\frac{\theta}{2}\right)\left(\kappa - 1 + 2\,\sin^2\left(\frac{\theta}{2}\right)\right) \\
&\quad + \frac{K_{\mathrm{II}}}{2\,\mu}\sqrt{\frac{r}{2\,\pi}}\,\sin\left(\frac{\theta}{2}\right)\left(\kappa + 1 + 2\,\cos^2\left(\frac{\theta}{2}\right)\right) \\
u_2 &= \frac{K_{\mathrm{I}}}{2\,\mu}\sqrt{\frac{r}{2\,\pi}}\,\sin\left(\frac{\theta}{2}\right)\left(\kappa + 1 - 2\,\cos^2\left(\frac{\theta}{2}\right)\right) \\
&\quad - \frac{K_{\mathrm{II}}}{2\,\mu}\sqrt{\frac{r}{2\,\pi}}\,\cos\left(\frac{\theta}{2}\right)\left(\kappa - 1 - 2\,\sin^2\left(\frac{\theta}{2}\right)\right) \\
u_3 &= \frac{K_{\mathrm{III}}}{2\,\mu}\sqrt{\frac{r}{2\,\pi}}\,\sin\left(\frac{\theta}{2}\right)
\end{aligned} \tag{2.69}$$

with the KOLOSOV constant κ

$$\kappa = \begin{cases} \frac{3-\nu}{1+\nu} & \text{plane stress} \\ 3 - 4\,\nu & \text{plane strain} \end{cases} \quad , \tag{2.70}$$

and the shear modulus μ as well as POISSON's ratio ν. In concept of small strains (2.19) and linear, elastic, isotropic material behavior (2.54), one can see easily from (2.69), that $\sigma_{ij} \propto r^{-\frac{1}{2}}$, which reflects the WESTERGAARD solution.
Within the concept of LEFM, the energy release rate $\mathcal{G}$ can be directly rewritten in terms of the SIFs (see e.g. GROSS & SEELIG (2007))

$$\mathcal{G} = \frac{1}{E^\star}\left(K_{\mathrm{I}}^2 + K_{\mathrm{II}}^2\right) + \frac{1}{2\,\mu}K_{\mathrm{III}}^2 \quad , \tag{2.71}$$

with

$$E^\star = \begin{cases} E & \text{plane stress} \\ \frac{E}{1-\nu^2} & \text{plane strain} \end{cases} \quad , \tag{2.72}$$

with E denoting YOUNG's modulus. For three-dimensional problems, κ is set to $\kappa = 3 - 4\,\nu$ and $E^\star$ is set to $E^\star = E/\left(1-\nu^2\right)$.

Crack propagation using the J-integral

For the crack growth criterion (2.68) in a linear elastic medium the J-integral, introduced by RICE (1968), needs to be evaluated as in LEFM

$$\mathcal{G} = J \quad . \tag{2.73}$$

In order to explain the main aspects, the theory is only introduced for two-dimensional problems. The extension to three-dimensional problems can be found in e.g. MORAN & SHIH (1987a), MORAN & SHIH (1987b). The path-independent ring integral J

$$J = \int_C \left(W\,\delta_{1j} - \sigma_{ij}\,\frac{\partial u_i}{\partial \boldsymbol{g}_1} \right) n_j \,\mathrm{d}s \quad , \tag{2.74}$$

with the strain energy

$$W = \frac{1}{2}\,\sigma_{ij}\,\varepsilon_{ij} \tag{2.75}$$

is illustrated in figure 2.5, with the outward normal $\boldsymbol{n}$ and the path C.

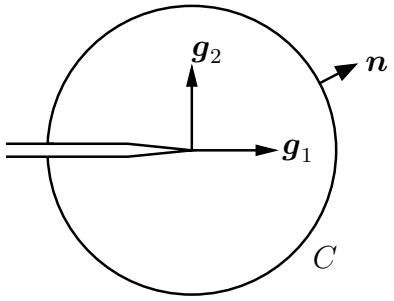

Figure 2.5: Contour C and outward normal $\boldsymbol{n}$ in local coordinate system with $\boldsymbol{g}_1 \cdot \boldsymbol{g}_2 = 0$.

Assuming two states of the domain with the current state $(\cdot)^{(1)}$ and an auxiliary state $(\cdot)^{(2)}$ yields the asymptotic fields for mode I/II. The superposition of both states leads to a different equilibrium and furthermore to a different integral

$$J^{(1+2)} = \int_C \left(W^{(1+2)}\,\delta_{1j} - \left(\sigma_{ij}^{(1)} + \sigma_{ij}^{(2)}\right) \left(\frac{\partial u_i^{(1)}}{\partial \boldsymbol{g}_1} + \frac{\partial u_i^{(2)}}{\partial \boldsymbol{g}_1} \right) \right) n_j \,\mathrm{d}s \quad , \tag{2.76}$$

with the superposed strain energy

$$W^{(1+2)} = \frac{1}{2}\left(\sigma_{ij}^{(1)} + \sigma_{ij}^{(2)}\right) \left(\varepsilon_{ij}^{(1)} + \varepsilon_{ij}^{(2)}\right) \quad . \tag{2.77}$$

Rewriting (2.76) identifies J for state (1), state (2) and the interaction integral $I^{(1,2)}$

$$J^{(1+2)} = J^{(1)} + J^{(2)} + I^{(1,2)} \quad , \tag{2.78}$$

with the interaction integral

$$I^{(1,2)} = \int_C \left(W^{(1,2)}\,\delta_{1j} - \sigma_{ij}^{(1)}\,\frac{\partial u_i^{(2)}}{\partial \boldsymbol{g}_1} - \sigma_{ij}^{(2)}\,\frac{\partial u_i^{(1)}}{\partial \boldsymbol{g}_1} \right) n_j \,\mathrm{d}s \quad , \tag{2.79}$$

and the strain energy

$$W^{(1,2)} = \frac{1}{2}\left(\sigma_{ij}^{(1)}\,\varepsilon_{ij}^{(2)} + \sigma_{ij}^{(2)}\,\varepsilon_{ij}^{(1)}\right) \quad . \tag{2.80}$$

Expanding (2.71) yields J for state (1), state (2) and a mixed term

$$J^{(1+2)} = J^{(1)} + J^{(2)} + \frac{2}{E^\star}\left(K_{\mathrm{I}}^{(1)}\,K_{\mathrm{I}}^{(2)} + K_{\mathrm{II}}^{(1)}\,K_{\mathrm{II}}^{(2)}\right) \quad , \tag{2.81}$$

which can be identified as the interaction integral by applying (2.78) to (2.81)

$$I^{(1,2)} = \frac{2}{E^\star}\left(K_{\mathrm{I}}^{(1)}\,K_{\mathrm{I}}^{(2)} + K_{\mathrm{II}}^{(1)}\,K_{\mathrm{II}}^{(2)}\right) \quad . \tag{2.82}$$

Choosing state (2) as pure mode I/II

$$K_{\mathrm{I}}^{(1)} = \frac{E^\star}{2}\,I^{(1,\text{mode I})} \quad , \quad K_{\mathrm{II}}^{(1)} = \frac{E^\star}{2}\,I^{(1,\text{mode II})} \quad , \tag{2.83}$$

yields a unique solution for the SIFs K_{I} and K_{II} in terms of the known field variables $\boldsymbol{\sigma}$, $\boldsymbol{\varepsilon}$ and $\boldsymbol{u}$. Here, the auxiliary state variables $(\cdot)^{(2)}$ are the WESTERGAARD solution (2.69) and their corresponding strains and stresses. Applying the SIFs to (2.71) and subsequently to (2.68) determines directly whether the crack propagates.
However, the SIFs do not yield a direction of growth at hand. Among the three most popular criteria to determine the direction θ_c of crack growth,

- the criterion of maximum hoop stress by ERDOGAN & SIH (1963),
- the criterion of minimum strain energy density by SIH (1974) and
- the criterion of maximum energy release by NUISMER (1975),

the criterion of maximum hoop stress is used here: the crack grows in the direction of the highest circumferential stress once the hoop stress exceeds the critical value σ_c. The stresses in terms of the SIFs can be determined easily, by computing the strains (2.19) in terms of the displacement field (2.69) and applying the constitutive model (2.54). The hoop stress $\sigma_{\theta\theta}$, defined in the local basis of the crack front according to figure 2.4, in terms of the coordinates r and θ follows

$$\begin{aligned}\sigma_{\theta\theta} = \frac{1}{4\sqrt{2\,\pi\,r}}\Bigg[K_{\mathrm{I}}\left(3\,\cos\left(\frac{\theta}{2}\right) + \cos\left(\frac{3\,\theta}{2}\right)\right) + \\ K_{\mathrm{II}}\left(3\,\sin\left(\frac{\theta}{2}\right) + 3\,\sin\left(\frac{3\,\theta}{2}\right)\right)\Bigg]\end{aligned} \quad , \tag{2.84}$$

while the critical stress σ_c can be reformulated in terms of the material constant $K_{\mathrm{I}c}$

$$\sigma_c = \frac{K_{\mathrm{I}c}}{\sqrt{2\,\pi\,r}} \quad , \tag{2.85}$$

yielding a reformulation of the initially introduced growth criterion (2.68)

$$\sigma_{\theta\theta}\left(\theta_c\right) \geq \sigma_c \quad \text{with} \quad \sqrt{\frac{\mathcal{G}}{\mathcal{G}_c}} = \frac{\sigma_{\theta\theta}\left(\theta_c\right)}{\sigma_c} \quad . \tag{2.86}$$

The direction of maximum hoop stress does clearly not depend on the distance r, such that the direction of crack growth yields

$$\left.\frac{\partial \sigma_{\theta\theta}}{\partial \theta}\right|_{\theta_c} = 0 \quad . \tag{2.87}$$

Applying (2.87) to (2.84) the direction of crack growth can be expressed in terms of the SIFs

$$\theta_c = \begin{cases} 2 \arctan \frac{1}{4}\left(\frac{K_{\mathrm{I}}}{K_{\mathrm{II}}} - \frac{K_{\mathrm{II}}}{||K_{\mathrm{II}}||}\sqrt{\frac{K_{\mathrm{I}}^2}{K_{\mathrm{II}}^2}+8}\right) & \text{for } K_{\mathrm{II}} \neq 0 \\ 0 & \text{for } K_{\mathrm{II}} = 0 \end{cases} , \tag{2.88}$$

displayed in figure 2.6. Hence, the deviation in the crack path for pure mode I loading vanishes as $\theta_c = 0$. For pure mode II loading the crack deflects about $\pm 70.5^{\circ}$, since $K_{\mathrm{I}} = 0$.

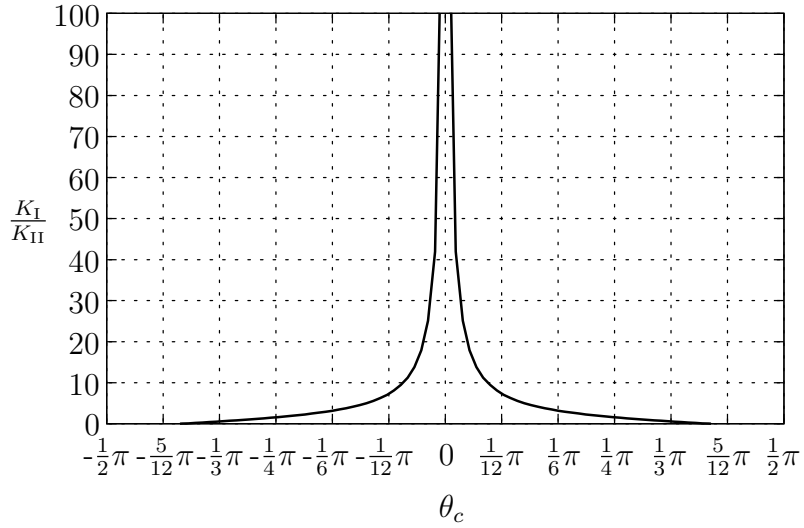

Figure 2.6: Angle of crack growth θ_c depending on ratio of SIFs.

Different models to predict the crack path for three-dimensional problems are discussed in RICHARD ET AL. (2005).

Crack propagation based on continuum damage mechanics

An alternative approach towards modeling brittle fracture are continuum damage models, introduced by KACHANOV (1958) for brittle, linear elastic, isotropic solids: Void growth and coalescence lead to degradation of the material, described by a certain scalar variable D, such that (2.57) reads

$$\boldsymbol{\sigma} = (1 - D)\, \mathbb{C} : \boldsymbol{\varepsilon} \quad . \tag{2.89}$$

Here, the damage variable D is zero for virgin material and $D = 1$ for completely broken material, such that $0 \leq D \leq 1$. Thus, a traction free boundary at the crack face is traditionally introduced via material softening and not via creation of new discrete crack surfaces. For

isotropic damage, the damage variable is usually driven by a scalar, depending on the current load state. Relating this scalar directly to the damage variable leads to localization, such that once fracture occurs the body breaks completely without requiring any work, despite the fact that energy dissipates. Furthermore, this localization leads to mesh dependent solutions in proceeding numerical analysis, as demonstrated by PEERLINGS (1999) among others. In order to overcome this inconvenience, a gradient enhanced damage model by LASRY & BELYTSCHKO (1988), PEERLINGS ET AL. (1996) is applied. The key idea of non-local models is to solve a HELMHOLTZ-type equation

$$\overline{\epsilon} - \operatorname{div}\left(c \operatorname{grad}\left(\overline{\epsilon}\right)\right) = \tilde{\epsilon} \quad , \tag{2.90}$$

with the boundary condition introduced by PEERLINGS ET AL. (1996)

$$\operatorname{grad}\left(\overline{\epsilon}\right) \cdot \boldsymbol{n} = 0 \quad \text{on } \partial\Omega \cup \Gamma \quad , \tag{2.91}$$

for the non-local equivalent strain $\overline{\epsilon} = \overline{\epsilon}\left(\boldsymbol{x}\right)$, which drives a damage variable D with $\dot{D} \geq 0$ instead of its local counterpart $\tilde{\epsilon}$. In (2.90) the variable c denotes the internal length scale and $\tilde{\epsilon}$ is the equivalent strain, which maps the strain tensor onto a scalar variable. A variety of different equivalent strain formulations are suitable for brittle fracture, according to LEMAITRE (1986), MAZARS & PIJAUDIER-CABOT (1989), BAŽANT ET AL. (1984), PIJAUDIER-CABOT & BAŽANT (1987), DE VREE ET AL. (1995), SIMO & JU (1987a) among others:

$$\tilde{\epsilon} = \sqrt{\Psi} = \sqrt{\boldsymbol{\varepsilon} : \mathbb{C} : \boldsymbol{\varepsilon}} \quad , \tag{2.92}$$

$$\tilde{\epsilon} = \sqrt{\Psi^{+}} = \sqrt{\boldsymbol{\varepsilon}_{+} : \mathbb{C} : \boldsymbol{\varepsilon}_{+}} \quad , \tag{2.93}$$

$$\tilde{\epsilon} = \sqrt{\sum_{i=1}^{3} \langle \varepsilon_i \rangle^2} \quad , \tag{2.94}$$

$$\tilde{\epsilon} = f\left(\mathrm{I}_1, \mathrm{J}_2, k\right) = \frac{\left(k-1\right)\mathrm{I}_1}{2\,k\left(1-2\,\nu\right)} + \sqrt{\left[\frac{\left(k-1\right)\mathrm{I}_1}{2\,k\left(1-2\,\nu\right)}\right]^2 + \frac{3\,\mathrm{J}_2}{k\left(1+\nu\right)^2}} \quad . \tag{2.95}$$

The value of the energy based equivalent strain measure (2.92) depends equally on compression and tension. Taking only positive eigenvalues ε_i of the strain tensor $\boldsymbol{\varepsilon}$ into account, i.e.

$$\boldsymbol{\varepsilon}_{+} = \sum_{i=1}^{3} \langle \varepsilon_i \rangle \, \boldsymbol{n}_i \otimes \boldsymbol{n}_i \quad , \tag{2.96}$$

with the MCAULEY brackets $\langle \bullet \rangle = \frac{1}{2}\left(\bullet + \| \bullet \|\right)$, yields an equivalent strain measure (2.93) which is more sensitive to tension. A similar procedure is to sum only positive eigenvalues as in (2.94), leading to different weights of positive strain components. Introducing the additional material parameter k, accounting for a relation of compression strength to tensile strength, i.e. if $k < 1$ the material is more sensitive to tension than to compression and vice versa, is used in the so-called modified VON MISES criterion (2.95). It depends on the first invariant I_1 of the strain tensor as well as on the second invariant J_2 of the deviatoric part of the strain tensor

$$\mathrm{I}_1 = \operatorname{tr}\left(\boldsymbol{\varepsilon}\right) \quad , \quad \mathrm{J}_2 = \frac{1}{2}\,\boldsymbol{\varepsilon} : \boldsymbol{\varepsilon} - \frac{1}{6}\left[\operatorname{tr}\left(\boldsymbol{\varepsilon}\right)\right]^2 \quad . \tag{2.97}$$

With one of these four approaches for the equivalent strain, (2.90) can be solved for the non-local equivalent strain.
A well known model to relate the damage variable D to this non-local quantity is

$$D = \begin{cases} 0 & \text{if } \bar{\epsilon} < \kappa_0 \\ \frac{\kappa_c}{\bar{\epsilon}} \frac{\bar{\epsilon}-\kappa_0}{\kappa_c-\kappa_0} & \text{if } \kappa_0 \leq \bar{\epsilon} \leq \kappa_c \\ 1 & \text{if } \bar{\epsilon} > \kappa_c \end{cases} , \tag{2.98}$$

sketched by LEMAITRE (1986) among others. As long as $\bar{\epsilon}$ is less than the threshold value κ_0 the material remains undamaged. Once this value is exceeded, material softening is induced according to (2.98) until the non-local equivalent strain reaches the second threshold value κ_c. At this stage of damage, $D = 1$, the material is completely broken, i.e. a crack emerges.
Assuming now purely brittle fracture, i.e. no softening occurs, the limiting case $\kappa_0 \to \kappa_c$ of (2.98) yields a simplified $\bar{\epsilon}$-D relation

$$\lim_{\kappa_0 \to \kappa_c} (D) = \begin{cases} 0 & \text{if } \bar{\epsilon} \leq \kappa_c \\ 1 & \text{if } \bar{\epsilon} > \kappa_c \end{cases} , \tag{2.99}$$

displayed together with (2.98) in figure 2.7. Until the non-local equivalent strain does not exceed the threshold value κ_c, the material remains undamaged. Once $\bar{\epsilon}$ is greater than this threshold value, the material is completely broken, which means that a crack emerges.

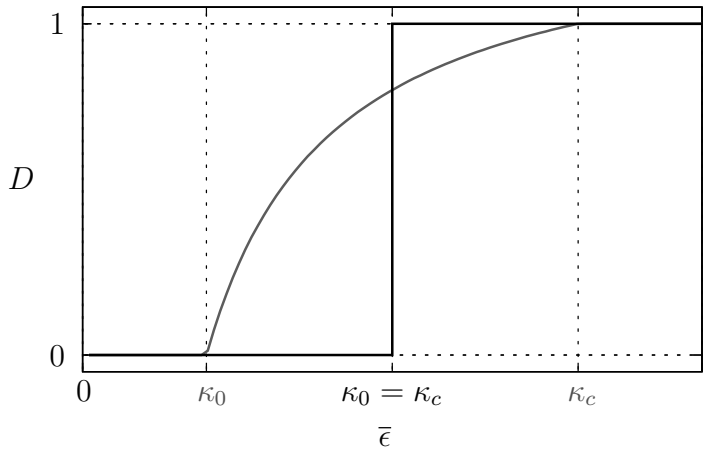

Figure 2.7: Gray: Classical damage approach following equation (2.98). Black: Approach without material softening (2.99).

In LEFM the relation between distance to the crack front r and strains is $\varepsilon_{ij} \propto r^{-\frac{1}{2}}$, which justifies the assumption that the non-local equivalent strain $\bar{\epsilon}$ is always highest at the crack front. The energetic equivalence of discrete fracture and material softening allows the coupling of both approaches, as shown by MAZARS & PIJAUDIER-CABOT (1996). Thus, the damage growth, i.e. crack growth, is not modeled via reduction of the tangent stiffness matrix, but by extending the current crack front discretely: An internal variable such as D is not required anymore. Consequently, the criterion for crack propagation reads

$$\begin{aligned} &\bar{\epsilon} > \kappa_c \quad \text{crack propagation} \quad , \\ &\bar{\epsilon} \leq \kappa_c \quad \text{no crack propagation} \quad . \end{aligned} \tag{2.100}$$

Advantageously, the presented approach can be applied to different constitutive models by an appropriate choice of the equivalent strain $\tilde{\epsilon}$ in (2.90), which was captured by e.g. AREIAS ET AL. (2003) and MEDIAVILLA ET AL. (2006a) for plasticity.
On the downside, the proposed method does not yield the direction of crack growth at hand and it can hardly be extracted from the introduced damage model as pointed out by DAWICKE ET AL. (1995) and MEDIAVILLA ET AL. (2006b) among others. This minor drawback can be overcome by applying the method proposed by FRIES & BAYDOUN (2012) to this model: Assuming pure mode I and mode II loading, the criterion of maximum hoop stress by ERDOGAN & SIH (1963) can be applied. Spanning a local coordinate system at the crack front as displayed in figure 2.4, the direction θ_c of maximum hoop stress $\max(\sigma_{\theta\theta})$ in the $\boldsymbol{g}_1$–$\boldsymbol{g}_2$ plane can be found.

Weak form

Besides the balance of linear momentum, the solution of a second equation is now required to determine crack growth. Similar to the weak form of the balance of linear momentum, a test function $\delta\overline{\epsilon} = \delta\overline{\epsilon}(\boldsymbol{x})$ is multiplied with (2.90) and integrated over the whole domain, yielding

$$\int_\Omega \left[\overline{\epsilon} - c\,\nabla^2\overline{\epsilon} - \tilde{\epsilon}\right] \cdot \delta\overline{\epsilon}\,\mathrm{d}v = 0 \quad . \tag{2.101}$$

The derivative

$$\nabla\left(\delta\overline{\epsilon} \cdot \nabla\overline{\epsilon}\right) = \delta\overline{\epsilon} \cdot \nabla^2\overline{\epsilon} + \left(\nabla\delta\overline{\epsilon}\right)^{\mathrm{T}} \cdot \nabla\overline{\epsilon} \quad , \tag{2.102}$$

the divergence theorem and the application of (2.91) yield the weak form

$$\int_\Omega \delta\overline{\epsilon} \cdot \overline{\epsilon}\,\mathrm{d}v + c\int_\Omega \left(\nabla\delta\overline{\epsilon}\right)^{\mathrm{T}} \cdot \nabla\overline{\epsilon}\,\mathrm{d}v = \int_\Omega \delta\overline{\epsilon} \cdot \tilde{\epsilon}\,\mathrm{d}v \quad . \tag{2.103}$$

Further information about the concept of non-local and gradient enhanced damage models is well explained e.g. by PEERLINGS (1999).

Chapter 3

Finite Element Method

As continuous elliptic partial differential equations (PDE), here the conservation of linear momentum (2.29), (2.60) and the damage approach (2.90), (2.103), are in general not analytically solvable for arbitrary boundary conditions and geometries, numerical methods are usually applied to these type of problems. The finite element method (FEM) is a tool for solving elliptic PDEs and has gained attention within recent decades as being a robust, flexible, comparably fast and accurate solution method. Consequently a huge variety of literature is available, covering different aspects of the finite element method. Hence, in this chapter only the fundamentals of a displacement FE formulation are briefly summarized. The interested reader is referred to ZIENKIEWICZ & TAYLOR (2005b), ZIENKIEWICZ & TAYLOR (2005a), BATHE (1986), SIMO & HUGHES (1998), BELYTSCHKO ET AL. (2000), WRIGGERS (2008) among others.
Within the concept of LEFM, singular stress fields occur naturally as explained in section 2.6. However, the standard FEM is not able to capture these singular stress fields accurately using an acceptable amount of computation time. Thus, the FEM needs to be extended using more suitable ansatz functions. The so-called extended finite element method (XFEM) overcomes these issues and is therefore frequently used in the concept of computational fracture mechanics. STROUBOULIS ET AL. (2001), FRIES & BELYTSCHKO (2010), POMMIER ET AL. (2011) among others give a precise overview of this method.

3.1 Bilinear/trilinear displacement Finite Element approach

To solve the weak form of equilibrium (2.60) numerically using the FEM requires the approximation of different measures. A main idea of the finite element method is the subdivision of a body $\mathcal{B}$ into finite elements e with their volume Ω_e

$$\mathcal{B} \approx \bigcup_{e=1}^{n_e} \Omega_e \quad , \tag{3.1}$$

with n_e being the total number of elements in the whole domain. A subdivision of a domain is illustrated in figure 3.1: The elements are connected via their nodes $\boldsymbol{x}_I$, while all nodes

that are attached to one element need to be part of this element in standard FE approaches. Depending on the element shape and size, discretization errors of the boundary of the domain occur. Consequently, the DIRICHLET and NEUMANN boundary conditions are affected by this approximation: The smaller the finite elements are, or the better they can reflect the outer boundary of the domain by using higher order interpolation functions, the smaller the discretization error becomes.

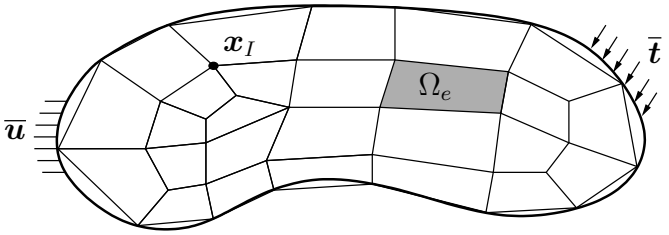

Figure 3.1: Body discretized with elements Ω_e containing nodes $\boldsymbol{x}_I$ with prescribed tractions $\overline{\boldsymbol{t}}$ and displacements $\overline{\boldsymbol{u}}$.

3.1.1 Isoparametric concept

Defining locally supported ansatz functions, also known as shape functions, used to interpolate the initial as well as current coordinates in the discretized domain, leads to an approximation of the coordinates

$$\boldsymbol{X} = \sum_{I=1}^{n_n} N_I(\boldsymbol{\xi})\, \boldsymbol{X}_I \quad , \quad \boldsymbol{x} = \sum_{I=1}^{n_n} N_I(\boldsymbol{\xi})\, \boldsymbol{x}_I \quad . \tag{3.2}$$

Here, n_n denotes the number of nodes in the whole domain. The focus in this thesis is to develop new techniques and improve existing methods for the 4-node quadrilateral Q1 element for two and the 8-node hexahedral Q1 element for three-dimensional problems.

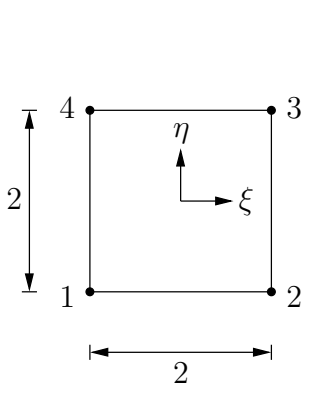

(a) 4-node quadrilateral element.

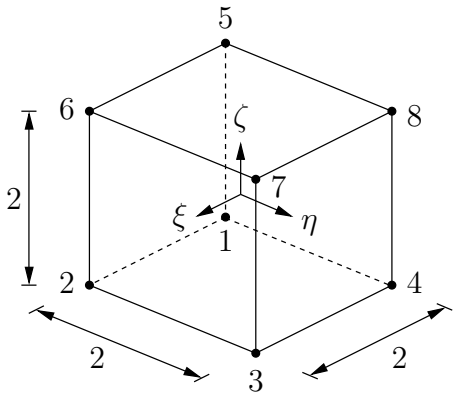

(b) 8-node hexahedral element.

Figure 3.2: 2D/3D isoparametric reference elements $\Omega_\square$.

These elements are defined in the isoparametric reference configuration denoted by the subscript $(\cdot)_\square$, displayed in figure 3.2. This configuration has no physical meaning, but facilitates the fast implementation of finite elements, applicable to arbitrary geometries: The nodal shape functions $N_I(\boldsymbol{\xi})$ and the evaluation of the weak form of equilibrium are formulated in the isoparametric reference configuration and are mapped to the initial or current configuration. Within the isoparametric concept, the displacement and virtual displacement field are approximated using the same shape functions as used for the geometry

$$\boldsymbol{u} = \sum_{I=1}^{n_n} N_I(\boldsymbol{\xi})\, \boldsymbol{u}_I \quad , \quad \delta\boldsymbol{u} = \sum_{I=1}^{n_n} N_I(\boldsymbol{\xi})\, \delta\boldsymbol{u}_I \quad . \tag{3.3}$$

The chosen ansatz should fulfill the partition of unity – the sum of all nodal shape functions are one everywhere – and the shape function N_I should be one only at node I and zero at all other nodes

$$\sum_{I=1}^{n_n} N_I(\boldsymbol{\xi}) = 1 \quad , \tag{3.4}$$

$$N_I(\boldsymbol{x}_J) = \delta_{IJ} \quad \text{for} \;\; I, J = 1, \ldots, n_n \quad . \tag{3.5}$$

A popular choice for the ansatz functions are the LAGRANGE polynomials, which fulfill the above mentioned requirements (3.5). For a one-dimensional problem, the shape function for node I reads

$$N_I(\xi) = \prod_{J=1\,,\; J\neq I}^{n_{ne}} \frac{\xi_J - \xi}{\xi_J - \xi_I} \quad \text{with} : -1 \leq \xi \leq 1 \quad . \tag{3.6}$$

Here, n_{ne} denotes the number of nodes belonging to a single finite element, with $n_{ne} = 4/8$ in this work for 2D/3D problems respectively. Thus, the order of the polynomial shape function depends on the number of nodes per element: $(n_{ne} - 1)$. Choosing the introduced Q1 elements results in bi-/trilinear shape functions for 2D/3D problems respectively

$$\begin{aligned} N_I(\boldsymbol{\xi}) &= \frac{1}{4}\,(1 + \xi_I\,\xi)\,(1 + \eta_I\,\eta) \quad , \\ N_I(\boldsymbol{\xi}) &= \frac{1}{8}\,(1 + \xi_I\,\xi)\,(1 + \eta_I\,\eta)\,(1 + \zeta_I\,\zeta) \quad , \end{aligned} \tag{3.7}$$

with ξ_I, η_I and ζ_I being the nodal coordinates of the reference configuration. As many computations are performed in the reference configuration, a mapping from the isoparametric space to the initial or current configuration is required. With the JACOBIan tensors

$$\boldsymbol{J} = \frac{\partial \boldsymbol{X}}{\partial \boldsymbol{\xi}} = \sum_{I=1}^{n_n} \boldsymbol{X}_I \otimes \frac{\partial N_I(\boldsymbol{\xi})}{\partial \boldsymbol{\xi}} \quad , \quad \boldsymbol{j} = \frac{\partial \boldsymbol{x}}{\partial \boldsymbol{\xi}} = \sum_{I=1}^{n_n} \boldsymbol{x}_I \otimes \frac{\partial N_I(\boldsymbol{\xi})}{\partial \boldsymbol{\xi}} \quad , \tag{3.8}$$

and the relation to the deformation gradient $\boldsymbol{F} = \boldsymbol{j} \cdot \boldsymbol{J}^{-1}$, all measures can be mapped to any coordinate system, as sketched in figure 3.3.

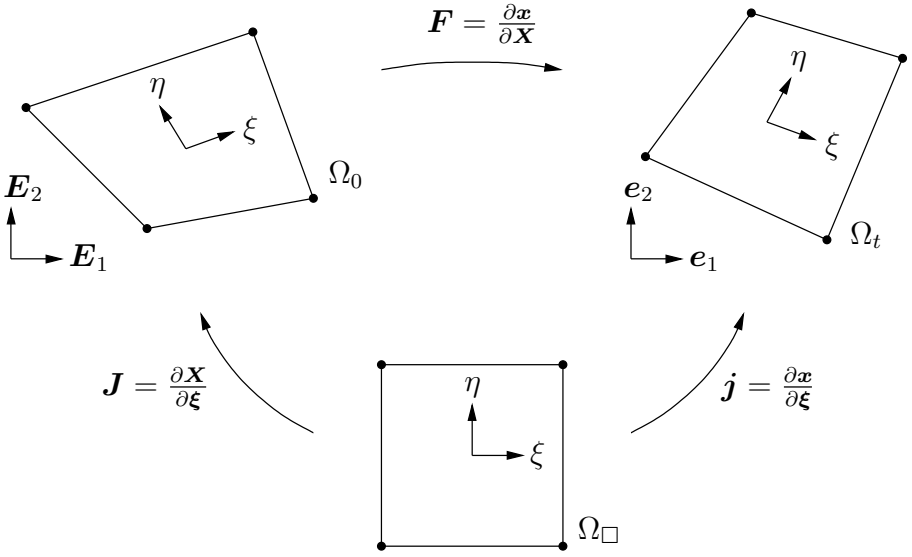

Figure 3.3: Isoparametric mapping applied to one deformed element.

3.1.2 Discretization of the weak form

Applying the FE approach to (2.60), the discretized weak form follows

$$\int_{\mathcal{B}_t} \boldsymbol{\sigma} : \nabla \delta \boldsymbol{u} \, \mathrm{d}v \approx \bigcup_{e=1}^{n_e} \sum_{I=1}^{n_{ne}} \delta \boldsymbol{u}_I \cdot \int_{\Omega_t} \boldsymbol{B}_I \cdot \boldsymbol{\sigma}^e \, \mathrm{d}v = \delta \tilde{\boldsymbol{u}} \cdot \boldsymbol{r}\left(\boldsymbol{u}\right) \quad , \tag{3.9}$$

$$\int_{\mathcal{B}_t} \boldsymbol{f} \cdot \delta \boldsymbol{u} \, \mathrm{d}v \approx \bigcup_{e=1}^{n_e} \sum_{I=1}^{n_{ne}} \delta \boldsymbol{u}_I \cdot \int_{\Omega_t} N_I \cdot \boldsymbol{f}^e \, \mathrm{d}v = \delta \tilde{\boldsymbol{u}} \cdot \boldsymbol{P}_\Omega \quad , \tag{3.10}$$

$$\int_{\partial \mathcal{B}_{t\sigma}} \bar{\boldsymbol{t}} \cdot \delta \boldsymbol{u} \, \mathrm{d}a \approx \bigcup_{e=1}^{n_e} \sum_{I=1}^{n_{ne}} \delta \boldsymbol{u}_I \cdot \int_{\partial \Omega_t} N_I \cdot \boldsymbol{t}^e \, \mathrm{d}a = \delta \tilde{\boldsymbol{u}} \cdot \boldsymbol{P}_{\partial\Omega} \quad , \tag{3.11}$$

which is the basis for the implementation of the finite element method. The superscript $(\cdot)^e$ denotes the respective variable on the FE level, and the virtual displacement vector $\delta\tilde{\boldsymbol{u}}$ indicates the virtual displacement after assembling all elements in the domain. The matrix $\boldsymbol{B}_I$ contains the derivatives of the nodal shape functions of node I, such that

$$\frac{1}{2}\left(\nabla \delta \boldsymbol{u} + \nabla^{\mathrm{T}} \delta \boldsymbol{u}\right) = \sum_{I=1}^{n_n} \boldsymbol{B}_I \cdot \delta \boldsymbol{u}_I \quad . \tag{3.12}$$

The variable $\boldsymbol{r}\left(\boldsymbol{u}\right)$ is called the internal nodal force vector, which depends on the nodal unknowns $\boldsymbol{u}_I$. The force vectors $\boldsymbol{P}_\Omega$ and $\boldsymbol{P}_{\partial\Omega}$ are the discretized volume forces and the discretized tractions respectively.

3.1.3 Numerical integration and solution procedure

In order to obtain a fast integration algorithm, the GAUSSIAN quadrature rule is applied. For one-dimensional problems, this method yields exact integration of the polynomial functions

of order $2\,n_{\mathrm{GP}} - 1$, with n_{GP} being the number of integration points. The integral of an arbitrary function $\boldsymbol{f}$ over the current element domain Ω_t, is mapped to the isoparametric element $\Omega_\square$ using the JACOBIan and finally approximated as a sum over all quadrature points n_{GP} with $\boldsymbol{f}$ evaluated at these points and multiplied with a weighting function w

$$\int_{\Omega_t} \boldsymbol{f}\,\mathrm{d}v = \int_{\Omega_\square} \boldsymbol{f}\det\left(\boldsymbol{j}^{\,e}\right)\,\mathrm{d}v_\square \approx \sum_{i=1}^{n_{\mathrm{GP}}} \boldsymbol{f}\left(\boldsymbol{\xi}_i\right)\det\left(\boldsymbol{j}^{\,e}\left(\boldsymbol{\xi}_i\right)\right)\,w\left(\boldsymbol{\xi}_i\right) \quad . \tag{3.13}$$

As the mapping from the isoparametric configuration to the initial or current configuration does not generally lead exactly to a polynomial, the numerical integration undergoes minor errors.
With the discretized weak form and the integration scheme at hand, the problem can be solved. Applying equations (3.9), (3.10), (3.11) to (2.60), with $\boldsymbol{P} = \boldsymbol{P}_\Omega + \boldsymbol{P}_{\partial\Omega}$, the weak form can be rewritten

$$\boldsymbol{g}\left(\boldsymbol{u}\right) = \boldsymbol{r}\left(\boldsymbol{u}\right) - \boldsymbol{P} = \boldsymbol{0} \tag{3.14}$$

assuming $\delta\boldsymbol{u}$ as being arbitrary, but non-zero. The generally non-linear system of equations can be solved using the NEWTON - RAPHSON method. Expanding (3.14) in a TAYLOR series, with neglection of the quadratic and higher order terms,

$$\boldsymbol{g}\left(\boldsymbol{u}_{k+1}\right) \approx \boldsymbol{g}\left(\boldsymbol{u}_k\right) + \left.\frac{\partial \boldsymbol{g}\left(\boldsymbol{u}_k\right)}{\partial \boldsymbol{u}}\right|_{\boldsymbol{u}=\boldsymbol{u}_k} \cdot \left(\boldsymbol{u}_{k+1} - \boldsymbol{u}_k\right) = \boldsymbol{0} \tag{3.15}$$

the non-linear system of equations can be solved iteratively for $\boldsymbol{u}$. The GÂTEAUX derivative in (3.15), often referred to as tangent stiffness matrix $\boldsymbol{K}_T$, is in this work independent of $\boldsymbol{P}$, since conservative forces are assumed. As all problems are reduced to linear ones here, the NEWTON - RAPHSON scheme needs one iteration until convergence is achieved, i.e. $\boldsymbol{g}\left(\boldsymbol{u}_1\right) \approx \boldsymbol{0}$.

3.2 Fundamentals of the eXtended Finite Element Method

Modeling cracks in the concept LEFM using the FEM has major drawbacks. In order to approximate the correct order of stress singularity at the crack front occurring in elasticity, a fine mesh is required, as LAGRANGE polynomials are generally not able to capture these singular behaviors. To overcome this drawback, moving the mid-side nodes of the crack tip elements to their quarter points and degenerate the quadrilateral to triangular elements as shown by HENSHELL & SHAW (1975), BARSOUM (1976), results in a $1/\sqrt{r}$ stress singularity. Secondly, the finite elements need to be aligned with the crack. Once the crack propagates, the region around the crack front requires remeshing and if the circumstances require, mapping of history data.
In order to obtain the desired singular stress field at the crack front, finite elements can be enriched with the analytical solution as shown by BENZLEY (1974), BABUŠKA ET AL. (1994), MELENK & BABUŠKA (1996) among others, which is an essential ingredient of todays extended finite element method. Depending on the choice of singular enrichment functions, the approach is either called generalized finite element method (GFEM) or extended finite

element method (XFEM). The key aspect, the use of enrichment functions and the initial application to fracture mechanics, remains. The GFEM/XFEM was successfully introduced by BELYTSCHKO & BLACK (1999), MOËS ET AL. (1999), DOLBOW (1999), DOLBOW ET AL. (2000), STROUBOULIS ET AL. (2000) to two-dimensional problems and by DUARTE ET AL. (2000), SUKUMAR ET AL. (2000), MOËS ET AL. (2002) to three-dimensional problems. Consequently, the desired stress singularity is captured accurately, but the XFEM itself does not provide mesh-independent crack path descriptions naturally. To overcome this drawback, nowadays the XFEM is mostly coupled with the level set method (LSM) by OSHER & SETHIAN (1988) in order to avoid remeshing during crack propagation computations: The crack is described using level set functions, i.e. signed distance functions, which are coupled with the problem specific enrichment functions as shown by STOLARSKA ET AL. (2001). Hence, the crack surface, i.e. the level set functions, needs to be updated after each propagation step, while the finite element mesh remains untouched. A vast amount of crack descriptions and level set updates have been successfully applied to computational fracture mechanics, e.g. the fast marching method by SUKUMAR ET AL. (2003), a geometrical approach by FRIES & BAYDOUN (2012) or solving the HAMILTON–JACOBI equation by GRAVOUIL ET AL. (2002). Alternatively, the crack can be described using a triangular mesh for three-dimensional problems instead of a level set function as demonstrated by DUARTE ET AL. (2001). Thus, remeshing is avoided during the numerical fracture process.
Additionally, the XFEM can be applied independently of the constitutive equations, briefly introduced in section 2.4. It was successfully applied to hyperelasticity by LEGRAIN ET AL. (2005), LOEHNERT ET AL. (2011), plasticity by ELGUEDJ ET AL. (2006), cohesive models by MOËS & BELYTSCHKO (2002) and damage mechanics by AREIAS & BELYTSCHKO (2005) among others. Besides fracture mechanics, a wide range of various problems such as thermal problems, inhomogeneous materials, solidification problems, two-fluid flows and dislocations as reported by FRIES & BELYTSCHKO (2010) can be solved with this numerical method.
Due to its mesh independent crack description, its applicability to different material models and its accurate solution at the crack front, the XFEM is the method chosen to model discrete fracture.

3.2.1 Level set method

In order to track moving interfaces such as cracks, the level set method by OSHER & SETHIAN (1988) is applied to the XFEM. A level set function $\psi = \psi(\boldsymbol{x})$ of an interface Γ_c is the signed distance function to the interface

$$\psi(\boldsymbol{x}) = \pm \min \|\boldsymbol{x} - \boldsymbol{x}_{\Gamma_c}\| \quad , \tag{3.16}$$

with $\boldsymbol{x}_{\Gamma_c}$ being a point on the interface, illustrated in figure 3.4. As a crack in general has at least one crack front, a second level set $\phi = \phi(\boldsymbol{x})$ is needed to model a crack via level sets: Its gradient is chosen to be orthogonal to the gradient of the first level set value, i.e. $\nabla\psi \cdot \nabla\phi = 0$, such that the position of the crack Γ_c and its front $\partial\Gamma_c$ can be determined

$$\begin{aligned} \phi < 0 \ \wedge \ \psi = 0 \quad &\Leftrightarrow \quad \boldsymbol{x} \in \Gamma_c \backslash \partial\Gamma_c \quad , \\ \phi = 0 \ \wedge \ \psi = 0 \quad &\Leftrightarrow \quad \boldsymbol{x} \in \partial\Gamma_c \quad . \end{aligned} \tag{3.17}$$

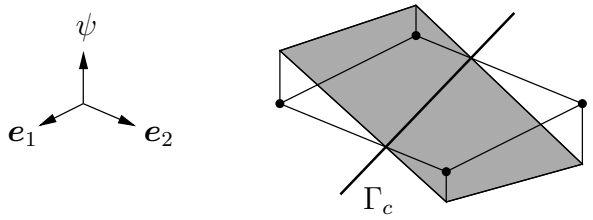

Figure 3.4: Bilinear level set function $\psi(\boldsymbol{x})$ of a one-dimensional interface Γ_c in a two-dimensional domain.

With this orthogonal construction of the second level set field, the distance r to the crack front as well as the angle θ of a point $\boldsymbol{x}$ illustrated in figure 2.4 can be determined directly from the level set values

$$r = \sqrt{\psi^2 + \phi^2} \quad , \quad \theta = \arctan\left(\frac{\psi}{\phi}\right) \quad . \tag{3.18}$$

In this work, the level set fields are stored nodalwise and interpolated over the domain using the same mesh and the same shape functions as applied to the displacement field approximation introduced in section 3.1.1. Thus, the level set approximation reads

$$\psi(\boldsymbol{\xi}) = \sum_{I=1}^{n_n} N_I(\boldsymbol{\xi})\,\psi_I \quad , \quad \phi(\boldsymbol{\xi}) = \sum_{I=1}^{n_n} N_I(\boldsymbol{\xi})\,\phi_I \quad . \tag{3.19}$$

For two-dimensional problems, a crack is a one-dimensional interface and assumed to be a straight line in a finite element in the reference configuration $\Omega_\square$. Consequently, the crack becomes a bilinear function in an element in the initial and current configuration due to the choice of its interpolation. This features a fast level set update and an accurate integration, introduced in section 3.2.3. However, this methodology is not applied to three-dimensional problems.

3.2.2 Enrichment functions

Once the level set fields have been determined, certain sets of nodes are enriched to incorporate the analytical solution (2.69) in the FE problem. Generally, the displacement field approximation in terms of the XFEM

$$\boldsymbol{u}(\boldsymbol{x}) = \underbrace{\sum_{I\in\mathcal{I}} N_I(\boldsymbol{x})\;\boldsymbol{u}_I}_{\text{Standard FE approx.}} + \underbrace{\sum_{I\in\mathcal{I}^\star} M_I(\boldsymbol{x})\;\boldsymbol{a}_I}_{\text{XFEM enrichment}} \quad , \tag{3.20}$$

is an extension to the standard FE approximation (3.3). Following BELYTSCHKO & BLACK (1999) as well as MOËS ET AL. (1999) the extended displacement field approximation for discrete cracks reads

$$\begin{aligned}\boldsymbol{u}(\boldsymbol{x}) = &\sum_{I\in\mathcal{I}} N_I(\boldsymbol{x})\;\boldsymbol{u}_I + \sum_{J\in\mathcal{J}}\sum_{j=1}^{4} N_J(\boldsymbol{x})\,f_j(\boldsymbol{x})\;R(\boldsymbol{x})\;\boldsymbol{a}_{Jj} \\ &+ \sum_{K\in\mathcal{K}} N_K(\boldsymbol{x})\;H(\boldsymbol{x})\;\boldsymbol{b}_K \quad .\end{aligned} \tag{3.21}$$

Here, the first term is the standard FE displacement approximation (3.3) applied to all nodes $\mathcal{I}$, while the following terms are the enrichments including their shape functions. In (3.21), the nodal subset $\mathcal{J} \subset \mathcal{I}$ contains only tip enriched nodes and the nodal subset $\mathcal{K} \subset \mathcal{I}$ contains all HEAVISIDE enriched nodes. The enrichment scheme is displayed in figure 3.5, where the nodes belonging to $\mathcal{K}$ are encircled and nodes belonging to $\mathcal{J}$ are marked with a square. Similar to (3.3), the approximation of the virtual displacement field $\delta\boldsymbol{u}$ receives additional nodal unknowns using the same enrichment scheme and shape functions as applied to the displacement field approximation (3.21).

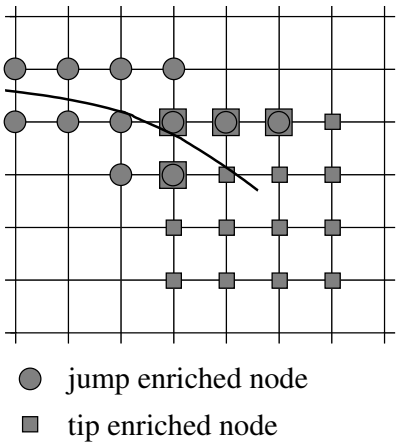

Figure 3.5: XFEM enrichment scheme.

The terms $\boldsymbol{u}_I$, $\boldsymbol{a}_{Jj}$ and $\boldsymbol{b}_K$ in (3.21) are the nodal unknowns, multiplied with their corresponding ansatz. The ansatz of the second term of the displacement field approximation is often referred to as crack tip enrichment function. Besides the bilinear/trilinear shape functions $N_I(\boldsymbol{x})$, it contains the so-called crack tip enrichment functions $f_j(\boldsymbol{x})$, with

$$f_{1-4}(\boldsymbol{x}) = \left\{ \sqrt{r}\sin\left(\frac{\theta}{2}\right), \sqrt{r}\cos\left(\frac{\theta}{2}\right), \sqrt{r}\sin\left(\frac{\theta}{2}\right)\sin(\theta), \sqrt{r}\cos\left(\frac{\theta}{2}\right)\sin(\theta) \right\} \tag{3.22}$$

spanning the near tip asymptotic fields of the WESTERGAARD problem and a ramp function $R(\boldsymbol{x})$. It can be seen easily, that the functions $f_j(\boldsymbol{x})$ yield the desired $r^{-\frac{1}{2}}$ singularity in the stress field as well as a traction free crack face Γ_c, i.e. $\boldsymbol{\sigma} \cdot \boldsymbol{n} = \boldsymbol{0}$ on Γ_c. With the application of the level set method and the relation (3.18), the angle θ as well as the distance r can be computed easily. The ramp function $R(\boldsymbol{x})$ introduced by LABORDE ET AL. (2005), FRIES (2008), LOEHNERT ET AL. (2011) ensures that the partition of unity is fulfilled in elements neighboring the crack tip/crack front elements, also known as blending elements. Therefore, these elements are included in the nodal subset $\mathcal{J}$ and multiplied with a ramp function sketched in figure 3.6

$$R(\boldsymbol{x}) = \sum_{I \in \mathcal{J}^\star} N_I(\boldsymbol{x}) \quad , \tag{3.23}$$

fading out the effect of the enrichment functions. Here, the nodal subset $\mathcal{J}^\star$ contains all nodes belonging to a crack tip element, i.e. an element in which a crack tip/crack front ends. Consequently, the partition of unity is fulfilled in the whole domain. As shown by FRIES (2008), the application of the ramp function results in linearly dependent enrichment functions $f_{1-4}(\boldsymbol{x})$ in blending elements. Omitting the enrichment functions $f_4(\boldsymbol{x})$, $f_3(\boldsymbol{x})$ and $f_{2-4}(\boldsymbol{x})$ was investigated by LOEHNERT ET AL. (2011): the system of equations is uniquely solvable and all three computations yield similar convergences. Note that the first enrichment function $f_1(\boldsymbol{x})$ cannot be dropped as it is the only one out of these four functions that is discontinuous on the crack face and is thus needed to preserve a jump in the displacement field. An alternative ramp function with less enriched nodes is introduced in section 5.2.2.

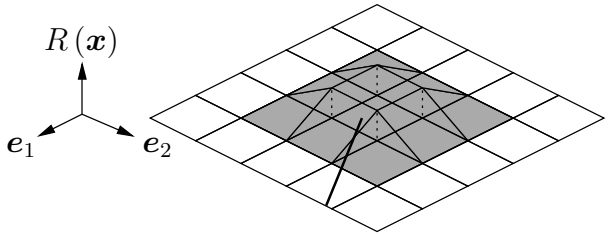

Figure 3.6: Ramp function $R(\boldsymbol{x})$.

The last term of (3.21), often referred to as HEAVISIDE enrichment function, is applied to nodes of completely cracked elements. This enrichment function ensures that the crack face remains traction free, i.e. $\boldsymbol{\sigma} \cdot \boldsymbol{n} = \boldsymbol{0}$ on Γ_c, and thus enforces a jump in the displacement field at the crack face. The enrichment function $H(\boldsymbol{x})$ is the modified HEAVISIDE function

$$H(\boldsymbol{x}) = H(\psi(\boldsymbol{x})) = \begin{cases} +1 & \text{if } \psi(\boldsymbol{x}) \geq 0 \\ -1 & \text{if } \psi(\boldsymbol{x}) < 0 \end{cases} , \tag{3.24}$$

which can be evaluated quickly by determining the sign of the level set function at the current integration point.

3.2.3 Integration

Apart from all its advantages in linear elastic fracture mechanics, the XFEM has two minor drawbacks, which are addressed in this section: The integration of cracked elements is not as straight forward as in standard FEM and the position of cracks in finite elements needs special attention to avoid linear dependencies.
Differentiating (3.21) with respect to $\boldsymbol{x}$ at node $\boldsymbol{x}_I$, what is needed for the $\boldsymbol{B}$-matrix, requires the derivative

$$\frac{\partial N_I(\boldsymbol{x})\ H(\boldsymbol{x})}{\partial \boldsymbol{x}} = \frac{\partial H(\boldsymbol{x})}{\partial \boldsymbol{x}} N_I(\boldsymbol{x}) + \frac{\partial N_I(\boldsymbol{x})}{\partial \boldsymbol{x}} H(\boldsymbol{x}) \quad . \tag{3.25}$$

Differentiating the HEAVISIDE function yields the DIRAC delta function $\delta(\boldsymbol{x})$ and thus

$$\frac{\partial H(\boldsymbol{x})}{\partial \boldsymbol{x}} N_I(\boldsymbol{x}) = \delta(\boldsymbol{x}) = \begin{cases} +\infty & \text{if } \boldsymbol{x} \in \Gamma_c \\ 0 & \text{if } \boldsymbol{x} \notin \Gamma_c \end{cases} \quad . \tag{3.26}$$

As infinity values are unexpedient in numerical simulations, these values need to be avoided. Therefore, all elements containing cracks are subdivided into triangles/tetrahedrons with the crack aligned with their edges/faces as shown for two-dimensional elements by MOËS ET AL. (1999) and three-dimensional elements by LOEHNERT ET AL. (2011). Performing the integral in these subcells avoids quadrature points on edges and faces of triangles/tetrahedrons such that infinite derivatives are prevented. Furthermore, this procedure ensures quadrature points on both sides of the crack to take into account the discontinuous displacement field. Splitting cracked and partly cracked elements is displayed in figure 3.7 for two-dimensional problems: Since there are two possibilities of how a linear function, e.g. a crack, can intersect with a quadrilateral, two subdivision options need to be thought of. Either a crack intersects neighboring sides or opposite sides of the element, resulting in a pentagon and a triangle or in two quadrilaterals respectively. Inserting a point in the center of both subdomains and connecting the center point to the nodes of the quadrilateral and the intersection points, as illustrated in figure 3.7(a), (b), results in the desired subdivision into triangles, with their edges aligned with the crack face Γ_c. Elements containing a crack tip, such as depicted in figure 3.7(c), are generally split into five triangles: The crack tip is connected to all four vertices and to the intersection point of crack and quadrilateral, resulting in triangles aligned with the crack face Γ_c. If the crack intersects the quadrilateral at one of its nodes, the number of triangles reduces to four. The extension for three-dimensional elements used in this work follows the same strategy as explained in detail by LOEHNERT ET AL. (2011).

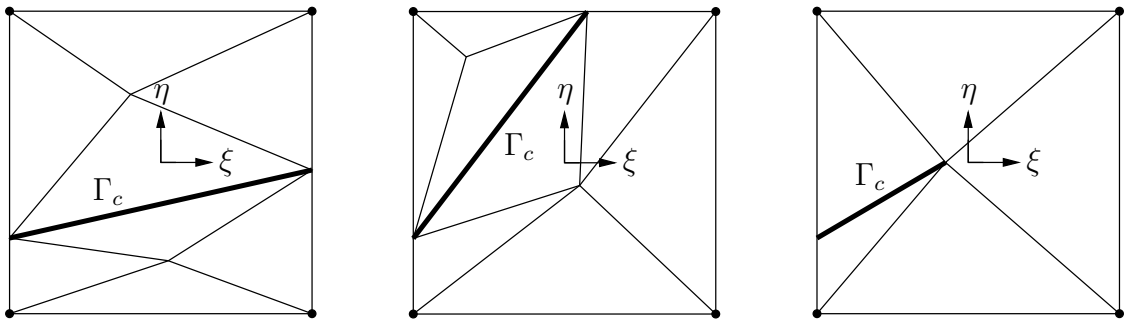

(a) Cracked element: Crack intersecting opposite sides of quadrilateral.

(b) Cracked element: Crack intersecting neighboring sides of quadrilateral.

(c) Element containing a crack tip.

Figure 3.7: Subdivision of cracked elements in isoparametric reference configurations.

A further improvement on the position of the quadrature points in elements containing a stress singularity was made by LABORDE ET AL. (2005): Using the DUFFY transformation by DUFFY (1982) yields a better approximation of the singular function and thus a better rate of convergence. This procedure was investigated by BÉCHET ET AL. (2005), MOUSAVI & SUKUMAR (2010) and MINNEBO (2012) in terms of the accuracy of the J-integral. As pointed out by MINNEBO (2012), standard integration still yields fairly good approximations of the J-integral using a reasonable number of integration points per tetrahedron. According to MINNEBO (2012), the benefits of the DUFFY transformation can only be seen using more

than 10^3 integration points per tetrahedron. To maintain fast computability, this transformation is not applied in this work.

3.2.4 Mesh regularization

As cracks may be distributed arbitrarily in the domain, nodal level set values ψ_I describing the crack face might be zero or approximately zero. The resulting HEAVISIDE and standard ansatz function for a one-dimensional problem are illustrated in figure 3.8, which demonstrates the ensuing problem: The HEAVISIDE enrichment function resembles the standard ansatz, which means that the functions are linearly dependent. Consequently, the system of equations cannot be solved uniquely.

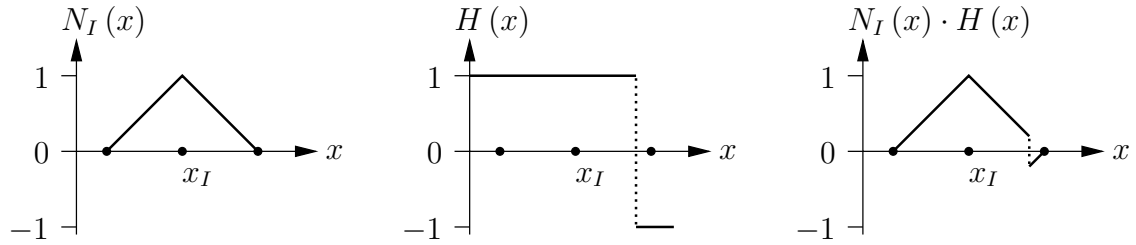

Figure 3.8: Standard shape function, HEAVISIDE function and HEAVISIDE enrichment function (1D).

A two-dimensional problem containing linear dependency due to crack geometry and finite element mesh is sketched in figure 3.9: The area A becomes so small, that the HEAVISIDE enrichment resembles the standard ansatz function.

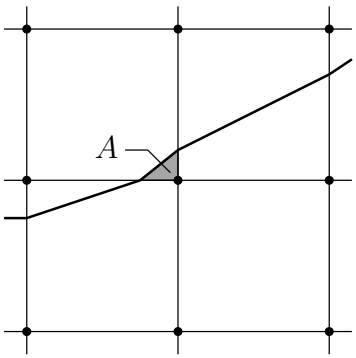

Figure 3.9: Linear dependent ansatz functions at center node.

To overcome this deficiency without changing the ansatz, four geometrical options can be considered following two main strategies: Either the area A needs to be enlarged or the area A is set to zero. Setting the area A to zero requires a special enrichment scheme for nodes intersected by the crack: Elements not intersected by the crack belonging to this node require either completely positive or completely negative level set values ψ_I, to maintain a traction free crack face. Thus, all nodes displayed in figure 3.9 will be enriched, which slightly increases the number of unknowns.

Setting the area A to zero can be achieved in two ways: Either the corresponding nodal level set value is set to zero as displayed in figure 3.10(a) or the respective node is shifted on to the crack face as sketched in figure 3.10(b). Setting the nodal level set to zero is easy to implement and does not cause any difficulties. Disadvantageously, this regularization changes the original geometry of the crack face and with it the original BVP. Shifting the node on to the crack face preserves the initially straight cracks, but for curved cracks, this regularization changes the original path as well, as displayed in figure 3.10(b).

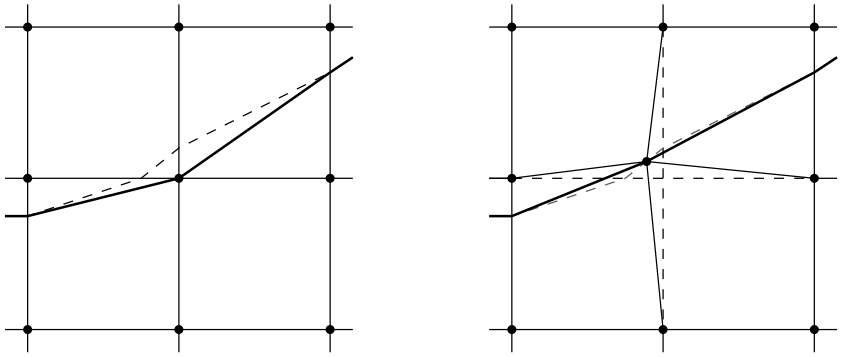

(a) Shift crack on to node.

(b) Shift node on to crack.

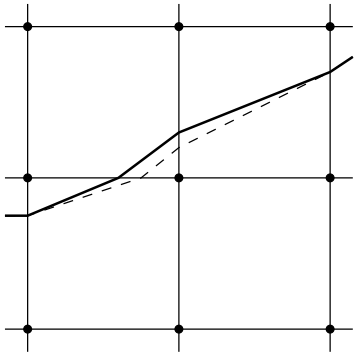

(c) Shift crack away from node.

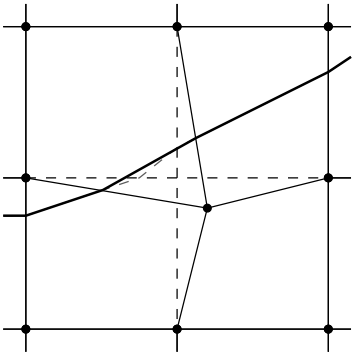

(d) Shift node away from crack.

Figure 3.10: Shifting mesh or node to avoid linear dependency.

The enlargement of area A can be obtained by either moving the crack or moving the corresponding finite element nodes: shifting the crack face in the direction of the gradient of the level set value $\psi(\boldsymbol{x})$ is displayed in figure 3.10(c). This adjustment changes the boundary value problem by changing the crack geometry. Moving the node in direction $\mathrm{grad}\,(\psi(\boldsymbol{x}))$ as illustrated in figure 3.10(d) does not change straight crack surfaces. However, the crack path approximation changes for curved cracks due to the bi-/trilinear level set field interpolation within one finite element. Furthermore, special attention is needed to be given to nodes on the boundary of the domain, in order to maintain the original outer boundary, when moving the node in direction $\mathrm{grad}\,(\psi(\boldsymbol{x}))$. Further details on this method are explained in detail by MUELLER-HOEPPE (2012).

As all four geometrical regularizations generally yield a slightly different BVP, the introduced methods are unfavorable. Preconditioning techniques by BÉCHET ET AL. (2005) and MENK & BORDAS (2011) avoid ill-posed systems of equations of nearly zero level set values

without changing any geometry. However, zero values cannot be treated with this technique such that a more elegant way by LOEHNERT (2013) is applied here: Instead of changing the geometry, the elemental stiffness matrix $\boldsymbol{K}^e$ is stabilized. Therefore, this symmetric matrix is decomposed into $\boldsymbol{V}$, containing its eigenvectors $\boldsymbol{v}^i$, and into $\boldsymbol{D}$, containing the eigenvalues d_i

$$\boldsymbol{K}^e = \boldsymbol{V} \cdot \boldsymbol{D} \cdot \boldsymbol{V}^{\mathrm{T}} \quad . \tag{3.27}$$

However, $\boldsymbol{D}$ naturally contains zero eigenvalues, e.g. due to rigid body motions, which have to be preserved. However, further physically and numerically meaningful zero modes might occur due to the fact that $\boldsymbol{K}^e$ contains contributions from enrichment functions and their corresponding DOFs as well. These modes strongly depend on the enrichment scheme in the finite element and on the position of the crack. On the other hand, unfavorable crack paths as displayed in figure 3.9 might yield very small or zero eigenvalues, which is physically and numerically meaningless. Stabilizing these modes yields a well conditioned systems of equations, without changing any geometrical properties. Decomposing (3.27) into non-zero eigenmodes $\bar{\boldsymbol{V}}$, referring to non-zero eigenvalues $\bar{\boldsymbol{D}}$ and into zero eigenmodes $\boldsymbol{V}_0$, containing n eigenvectors $\boldsymbol{v}_0^i$, yields

$$\boldsymbol{K}^e = \left(\bar{\boldsymbol{V}}, \boldsymbol{V}_0\right) \cdot \begin{pmatrix} \bar{\boldsymbol{D}} & \boldsymbol{0} \\ \boldsymbol{0} & \boldsymbol{0} \end{pmatrix} \cdot \begin{pmatrix} \bar{\boldsymbol{V}}^{\mathrm{T}} \\ \boldsymbol{V}_0^{\mathrm{T}} \end{pmatrix} \quad . \tag{3.28}$$

In order to keep the meaningful zero modes $\bar{\boldsymbol{V}}_0 \subset \boldsymbol{V}_0$, containing $\bar{n}$ eigenvectors $\bar{\boldsymbol{v}}_0^i$, and to stabilize meaningless zero modes $\hat{\boldsymbol{V}}_0 = \boldsymbol{V}_0 \backslash \bar{\boldsymbol{V}}_0$, distinguishing between physically and numerically meaningful and meaningless modes is necessary. As all eigenvectors in $\bar{\boldsymbol{V}}_0$ depend on the shape of the finite element, its enrichment scheme and the crack geometry, these vectors can be computed in advance. Orthonormalizing $\boldsymbol{v}_0^i$ with $\bar{\boldsymbol{v}}_0^i$ naturally eliminates physically and numerically meaningful modes yielding

$$\hat{\boldsymbol{v}}_0^i = \boldsymbol{v}_0^i - \sum_{j=1}^{\bar{n}} \frac{\boldsymbol{v}_0^i \cdot \bar{\boldsymbol{v}}_0^j}{\bar{\boldsymbol{v}}_0^j \cdot \bar{\boldsymbol{v}}_0^j} \bar{\boldsymbol{v}}_0^j \quad \forall\, i \in [1, n] \quad . \tag{3.29}$$

As the solution for $\boldsymbol{V}_0$ is not unique, i.e. it might be rotated arbitrarily within itself, there are $\bar{n}$ linearly dependent vectors $\hat{\boldsymbol{v}}_0^i$. Orthonormalizing $\hat{\boldsymbol{v}}_0^i$ with itself yields

$$\hat{\hat{\boldsymbol{v}}}_0^i = \hat{\boldsymbol{v}}_0^i - \sum_{j=1}^{i-1} \frac{\hat{\boldsymbol{v}}_0^i \cdot \hat{\boldsymbol{v}}_0^j}{\hat{\boldsymbol{v}}_0^j \cdot \hat{\boldsymbol{v}}_0^j} \hat{\boldsymbol{v}}_0^j \quad \forall\, i \in [1, n] \quad , \tag{3.30}$$

which leads to $n - \bar{n}$ zero eigenmodes $\hat{\hat{\boldsymbol{v}}}_0^i \in \hat{\hat{\boldsymbol{V}}}_0$ requiring stabilization.
Taking care of nearly zero eigenvalues d_j does not require any further computations, but only an evaluation of the already determined non-zero eigenvalues $\bar{\boldsymbol{D}}$

$$\gamma_j = \frac{||\epsilon\, d_1 - d_j||}{2} + \frac{\epsilon\, d_1 - d_j}{2} \geq 0 \quad . \tag{3.31}$$

Here, a comparison with the largest eigenvalue d_1 of the current element is chosen to ensure stabilization independent of the element shape. If the stabilization factor $\gamma_j > 0$, this mode

needs to be stabilized with its eigenvector $\bar{\boldsymbol{v}}_\epsilon^j \in \bar{\boldsymbol{V}}_\epsilon \subset \bar{\boldsymbol{V}}$, leading to m additional modes. As the resulting vector space $\bar{\boldsymbol{V}}_\epsilon$ is already orthogonal to the zero space $\boldsymbol{V}_0$, an additional orthonormalization is not necessary, leading to the vector space $\tilde{\boldsymbol{V}}$ requiring stabilization

$$\tilde{\boldsymbol{V}} = \left\{ \hat{\hat{\boldsymbol{V}}}_0, \bar{\boldsymbol{V}}_\epsilon \right\} \quad \tilde{\boldsymbol{v}}^j \in \tilde{\boldsymbol{V}} \quad . \tag{3.32}$$

Finally, the stiffness matrix and the residual vector $\boldsymbol{R}^e$ can be modified consistently yielding

$$\begin{aligned} \tilde{\boldsymbol{K}}^e &= \boldsymbol{K}^e + \sum_{j=1}^{n-\bar{n}+m} \gamma_j \, \tilde{\boldsymbol{v}}^j \otimes \tilde{\boldsymbol{v}}^j \quad , \\ \tilde{\boldsymbol{R}}^e &= \boldsymbol{R}^e + \sum_{j=1}^{n-\bar{n}+m} \gamma_j \, \tilde{\boldsymbol{v}}^j \otimes \tilde{\boldsymbol{v}}^j \cdot \hat{\boldsymbol{u}}^e \quad , \end{aligned} \tag{3.33}$$

with the displacement vector $\hat{\boldsymbol{u}}^e$ containing all nodal unknowns.
The tolerance ϵ is typically chosen to $\epsilon = 10^{-5}$, such that the impact on the solution is negligible, but the system of equations is well-conditioned.
Note that this technique only needs to be applied to completely enriched elements. As cracks are one dimension less than the dimension of the problem being solved, only a few elements are completely enriched. Thus, the eigenvalue decomposition, filtering the eigenvectors and modifying $\boldsymbol{K}^e$ and $\boldsymbol{R}^e$ only needs to be done for a few elements.
With this technique not only linear dependencies are avoided numerically, but also a significant speed-up for iterative solvers (here the GMRES) is gained. Here, the computation time for stabilized systems includes the time to determine $\tilde{\boldsymbol{K}}^e$ and $\tilde{\boldsymbol{R}}^e$. As this method holds for arbitrary meshes and cracks and furthermore neither changes any finite element geometry nor the crack path, this regularization method is the method of choice and thus applied in this work.

3.3 Discretization of non-local strain field

Besides the balance of linear momentum, the weak form of the HELMHOLTZ-type equation (2.103) is solved for $\overline{\epsilon}(\boldsymbol{x})$ using the finite element method. According to the introduced boundary conditions (2.91) and the presence of internal boundaries namely cracks, the non-local equivalent strain field is enriched similar to the displacement field approximation

$$\overline{\epsilon}(\boldsymbol{x}) = \sum_{I \in \mathcal{I}} N_I(\boldsymbol{x}) \, \overline{\epsilon}_I + \sum_{J \in \mathcal{J}} N_J(\boldsymbol{x}) \, f_1(\boldsymbol{x}) \, R(\boldsymbol{x}) \, \overline{\alpha}_J + \sum_{K \in \mathcal{K}} N_K(\boldsymbol{x}) \, H(\boldsymbol{x}) \, \overline{\beta}_K \quad . \tag{3.34}$$

Here, $\overline{\alpha}_J$ and $\overline{\beta}_K$ are the additional unknowns, which fulfill (2.91) in average on internal boundaries. The nodal sets $\mathcal{I}$, $\mathcal{J}$ and $\mathcal{K}$ are the same as in the displacement field approximation such that the enrichment scheme leads to three nodal unknowns at most describing the non-local equivalent strain field.
As $\overline{\epsilon}$ depends generally non-linearly on the strain tensor $\boldsymbol{\varepsilon}$ and as $\overline{\epsilon}$ drives usually non-linearly an internal damage variable D, the governing weak forms (2.60) and (2.103) are

strongly coupled. Furthermore, the system of equations is non-linear such that a NEWTON-RAPHSON scheme is applied, requiring a linearization of both weak forms. This linearization is explained in detail by PEERLINGS (1999), yielding

$$\begin{bmatrix} \boldsymbol{K}_{uu} & \boldsymbol{K}_{u\epsilon} \\ \boldsymbol{K}_{\epsilon u} & \boldsymbol{K}_{\epsilon\epsilon} \end{bmatrix} \cdot \begin{bmatrix} \Delta \boldsymbol{u} \\ \Delta \overline{\boldsymbol{\epsilon}} \end{bmatrix} = \begin{bmatrix} \boldsymbol{f}_u - \boldsymbol{K}_{uu}\, \boldsymbol{u}^{(i)} \\ \boldsymbol{f}_\epsilon - \boldsymbol{K}_{\epsilon\epsilon}\, \overline{\boldsymbol{\epsilon}}^{(i)} \end{bmatrix} \quad . \tag{3.35}$$

Here, the system matrix consists of two symmetric matrices $\boldsymbol{K}_{uu}$ and $\boldsymbol{K}_{\epsilon\epsilon}$ referring to the left-hand side of the weak forms (2.60) and (2.103) and to two rectangular matrices $\boldsymbol{K}_{u\epsilon}$ and $\boldsymbol{K}_{\epsilon u}$ referring to the coupling between those governing equations. With the matrices

$$\begin{aligned} \boldsymbol{K}_{uu} &= \int_\Omega \boldsymbol{B}^{\mathrm{T}}\, (1-D)\, \mathbb{C}\boldsymbol{B}\, \mathrm{d}v \quad , \\ \boldsymbol{K}_{u\epsilon} &= -\int_\Omega \boldsymbol{B}^{\mathrm{T}}\, \mathbb{C}\, \boldsymbol{\varepsilon}^{(i)}\, q\, N\, \mathrm{d}v \quad , \\ \boldsymbol{K}_{\epsilon u} &= -\int_\Omega N\, \boldsymbol{s}^{\mathrm{T}}\, \boldsymbol{B}\, \mathrm{d}v \quad , \\ \boldsymbol{K}_{\epsilon\epsilon} &= \int_\Omega N\, N + c\, \overline{\boldsymbol{B}}^{\mathrm{T}}\, \overline{\boldsymbol{B}}\, \mathrm{d}v \quad , \end{aligned} \tag{3.36}$$

and the load vectors

$$\begin{aligned} \boldsymbol{f}_u &= \int_{\partial\Omega_t} N\, \boldsymbol{t}\, \mathrm{d}a \quad , \\ \boldsymbol{f}_\epsilon &= \int_\Omega N\, \tilde{\epsilon}\, \mathrm{d}v \quad , \end{aligned} \tag{3.37}$$

the coupled system of equation exhibits another feature besides non-linearity: Due to the coupling terms $\boldsymbol{K}_{u\epsilon}$ and $\boldsymbol{K}_{\epsilon u}$ with $\boldsymbol{K}_{u\epsilon} \neq \boldsymbol{K}_{\epsilon u}^{\mathrm{T}}$, the global tangent matrix becomes non-symmetric and thus computationally expensive to solve. In (3.36), the matrix $\overline{\boldsymbol{B}}_I$ contains the derivatives of N_I such that

$$\overline{\boldsymbol{B}}_I^{\mathrm{T}} = \begin{bmatrix} \dfrac{\partial N_I}{\partial x} & \dfrac{\partial N_I}{\partial y} & \dfrac{\partial N_I}{\partial z} \end{bmatrix} \quad , \tag{3.38}$$

for a non-enriched node I. The definition of $\boldsymbol{s}$

$$\boldsymbol{s} = \left. \frac{\partial \tilde{\epsilon}}{\partial \boldsymbol{\varepsilon}} \right|_{\boldsymbol{\varepsilon}=\boldsymbol{\varepsilon}^{(i)}} \quad , \tag{3.39}$$

and q

$$q = \frac{\partial D}{\partial \bar{\epsilon}} \quad , \tag{3.40}$$

displays clearly the link between both governing equations. Applying (2.94) to (3.39) yields

$$\boldsymbol{s} = \frac{1}{\tilde{\epsilon}} \sum_{i=1}^{3} \langle \varepsilon_i \rangle\ \boldsymbol{n}_i \otimes \boldsymbol{n}_i \quad \forall\, \tilde{\epsilon} \neq 0 \quad . \tag{3.41}$$

Choosing the equivalent strain according to (2.95) yields

$$\boldsymbol{s} = \frac{(k-1)}{2\,k\,(1-2\,\nu)}\,\mathbf{1} + \frac{\left(\frac{(k-1)}{2\,k(1-2\,\nu)}\right)^2 \mathrm{I}_1\,\mathbf{1} + \frac{3}{2\,k\,(1+\nu)^2}\left(\frac{1}{6}\,\mathbf{1} - \boldsymbol{\varepsilon}\right)}{\sqrt{\left(\frac{(k-1)\mathrm{I}_1}{2\,k(1-2\,\nu)}\right)^2 + \frac{3\,\mathrm{J}_2}{k(1+\nu)^2}}} \quad . \tag{3.42}$$

Applying the damage model to crack propagation as introduced in section 2.6 means that the discrete crack is elongated following the criterion of maximum hoop stress with an amplitude depending on $\overline{\epsilon}$, introduced in section 5.3.1. Consequently, damage does not need to be taken into account via an internal variable D, such that it remains constant in this work with $D = 0$. Therefore, the derivative

$$q = \frac{\partial D}{\partial \overline{\epsilon}} = 0 \quad , \tag{3.43}$$

vanishes, such that $\boldsymbol{K}_{u\epsilon} = \mathbf{0}$. Thus, (3.35) leads to the following staggered solution scheme

$$\begin{array}{ll} (1) & \boldsymbol{K}_{uu} \cdot \Delta\boldsymbol{u} = \boldsymbol{f}_u - \boldsymbol{K}_{uu} \cdot \boldsymbol{u}^{(i)} \\ (2) & \boldsymbol{K}_{\epsilon\epsilon} \cdot \Delta\overline{\boldsymbol{\epsilon}} = \boldsymbol{f}_\epsilon - \boldsymbol{K}_{\epsilon\epsilon}\,\overline{\boldsymbol{\epsilon}}^{(i)} - \boldsymbol{K}_{\epsilon u} \cdot \Delta\boldsymbol{u} \end{array} \quad . \tag{3.44}$$

As the displacement field does not depend directly on the damage evolution, it reduces to a linear equation solved in the first step. Following, the right-hand side of the HELMHOLTZ-type equation is updated using the current displacement field and the non-local equivalent strain from the previous step $(\bullet)^{(i)}$. In a second solution step, $\Delta\overline{\boldsymbol{\epsilon}}$ can be determined, such that crack propagation can be investigated.

Chapter 4

Multiscale approach

Microcracks might induce crack shielding and crack amplification effects of macrocracks such that their SIFs decrease and increase respectively, as pointed out by RUBINSTEIN (1985, 1986), ROSE (1986b,a) and HUTCHINSON (1987) among others. This effect on the SIFs depends strongly on the position and the orientation of microcracks, such that microcracks are not negligible. Assuming macrocracks as well as microcracks, i.e. cracks of different length scales, in this work requires, despite the application of the XFEM, a relatively fine finite element mesh unless the mesh is refined adaptively: The higher the difference in the length of microcracks and macrocracks, the finer the FE mesh required. As the mesh resolution depends mainly on the size of the microcracks in relation to the size of the overall problem, the computational effort increases intensely using quadrilateral/hexahedral elements.
Using adaptive refinement via hanging nodes as shown by FRIES ET AL. (2011) as well as PRANGE ET AL. (2012) reduces the computational costs as long as crack propagation is prevented. In case of crack propagation, the existing hanging nodes are kept, while additional hanging nodes need to be created in order to capture microcrack growth precisely. Thus, the number of nodal unknowns increases with each propagation step depending on the initial crack configuration and the growth, which makes this method comparably expensive.
Alternatively a multiscale method capturing micro effects can be applied. Disadvantageously methods like the FE^2 method by FEYEL & CHABOCHE (2000) and by MIEHE ET AL. (1999) as well as the variational multiscale method by HUGHES (1995) are not able to capture localization effects at the fine scale as pointed out by GEERS ET AL. (2010). A so-called continuous–discontinuous approach, successfully applied in the context of damage mechanics by MASSART ET AL. (2007), can handle localization effects such as microcracks. Similar methods were successfully applied to discrete fracture using the XFEM: The multiscale aggregating discontinuity method (MAD) introduced by BELYTSCHKO ET AL. (2008) and extended by COENEN ET AL. (2012) among others averages the localization effects on the fine scale and maps those results to the coarse scale. Hence, macrocracks are created using the aggregated micro effects. The multiscale projection method by LOEHNERT & BELYTSCHKO (2007b) considers cracks of different length scales from the beginning of the computation which allows scale separation: Microcracks are taken into account in a region of interest, i.e. around the macrocrack tips, and are independent of macrocracks. Allowing scale separation yields another advantage: As long as the micro domains do not overlap, all micro domains can be computed independently of the macro domain and all other micro domains. Thus, the

computational costs can be dramatically reduced as micro computations can be computed in parallel. The assumption that microcracks are of length scales smaller than macrocracks in this work, makes the multiscale projection method the method of our choice, which will be introduced in this chapter.

4.1 Weak form

Even though the multiscale projection method is theoretically applicable to an infinite number of scales, this work is restricted to a two-scale approach, as the primal ideas as well as arising difficulties can be transferred one-to-one to further scales. In the following, the superscript $(\cdot)^0$ denotes macro variables, while the superscript $(\cdot)^1$ denotes micro variables. Splitting the displacement field into a macro displacement field $\boldsymbol{u}^0(\boldsymbol{x})$ and a micro displacement field $\boldsymbol{u}^1(\boldsymbol{x})$, yields

$$\boldsymbol{u}^1(\boldsymbol{x}) = \boldsymbol{u}^0(\boldsymbol{x}) + \tilde{\boldsymbol{u}}^1(\boldsymbol{x}) \quad . \tag{4.1}$$

Here, $\tilde{\boldsymbol{u}}^1(\boldsymbol{x})$ denotes the micro fluctuation field being non-zero in the fine scale domain Ω^1. As displayed in figure 4.1, this domain is set within a user defined radius r_{MS} around the macrocrack tips/fronts, since the highest stress concentrations and gradients in Ω^0 occur around the macrocrack tips. In this part of the domain micro effects, such as microcracks, are considered, while in the rest of the domain $\Omega^0 \setminus \Omega^1$, their influence is negligible, i.e. $\tilde{\boldsymbol{u}}^1(\boldsymbol{x}) = \boldsymbol{0}$. In Ω^1 the microcracks are modeled explicitly, while on the coarse scale they are taken into account implicitly by means of a projection of the stress field from the fine scale Ω^1 onto the coarse scale Ω^0. The size of the radius r_{MS} depends strongly on the size difference of the macrocracks to the microcracks as well as their location, orientation and quantity, as investigated by LOEHNERT & BELYTSCHKO (2007b).

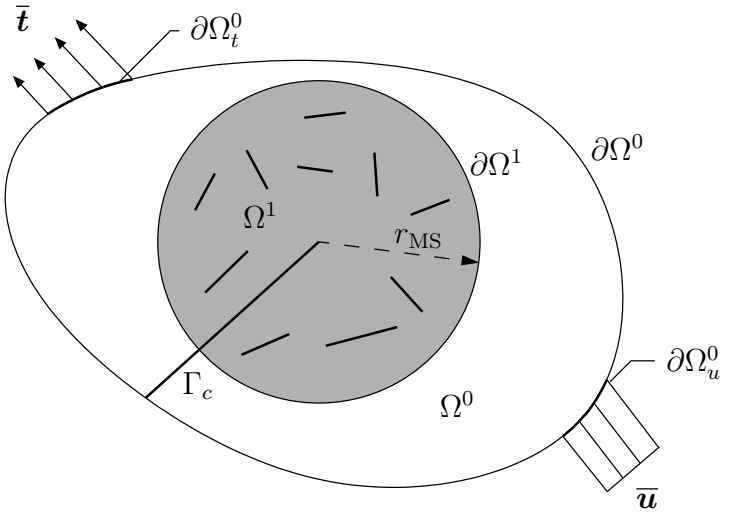

Figure 4.1: Coarse scale domain Ω^0 and fine scale domain Ω^1 containing microcracks and a macrocrack.

Applying the displacement field (4.1) to the balance of linear momentum (2.30), yields the weak forms of equilibrium for the coarse scale (4.2) and the fine scale (4.3) for static analysis as introduced in section 2.5

$$\int_{\Omega^0} \boldsymbol{\sigma}\left(\boldsymbol{u}^0 + \tilde{\boldsymbol{u}}^1\right) : \nabla \delta \boldsymbol{u}^0 \,\mathrm{d}v = \int_{\Omega^0} \boldsymbol{f} \cdot \delta \boldsymbol{u}^0 \,\mathrm{d}v + \int_{\partial\Omega_t^0} \overline{\boldsymbol{t}} \cdot \delta \boldsymbol{u}^0 \,\mathrm{d}a \quad , \tag{4.2}$$

$$\int_{\Omega^1} \boldsymbol{\sigma}\left(\boldsymbol{u}^0 + \tilde{\boldsymbol{u}}^1\right) : \nabla \delta \boldsymbol{u}^1 \,\mathrm{d}v = \int_{\Omega^1} \boldsymbol{f} \cdot \delta \boldsymbol{u}^1 \,\mathrm{d}v + \int_{\partial\Omega_t^1} \overline{\boldsymbol{t}} \cdot \delta \boldsymbol{u}^1 \,\mathrm{d}a \quad . \tag{4.3}$$

One can see easily from (4.2) that the coarse scale stresses, i.e. the residual, depends not only on $\boldsymbol{u}^0(\boldsymbol{x})$, but also on the fluctuation field $\tilde{\boldsymbol{u}}^1(\boldsymbol{x})$.
Discretizing both domains is depicted in figure 4.2: In elements intersected or enclosed by the circle spanned with r_{MS} around the crack tips/fronts, the fluctuation field $\tilde{\boldsymbol{u}}^1(\boldsymbol{x})$ is non-zero. Consequently these elements belong to the fine scale domain and are refined elementwise depending on the size of the microcracks for the fine scale computation. Furthermore microcracks are taken into account on the fine scale, displayed gray in figure 4.2.

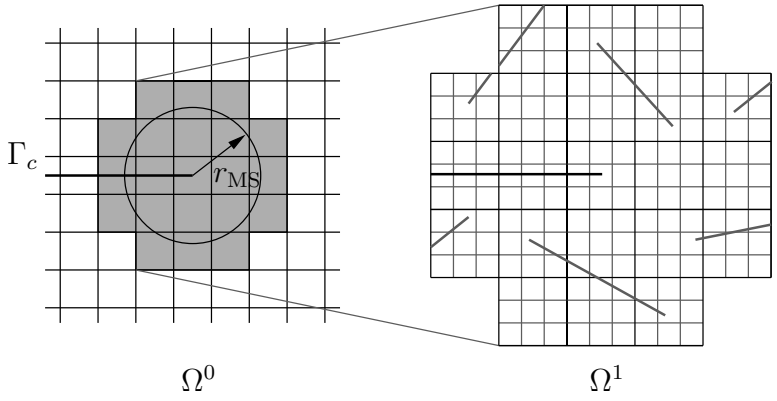

Figure 4.2: Discretized coarse scale domain Ω^0 and fine scale domain Ω^1. In Ω^1, coarse scale elements and macrocracks are depicted black, fine scale elements and microcracks are depicted gray. Here, each macro element is subdivided into 3×3 micro elements.

As cracks are modeled in this work, the displacement fields $\boldsymbol{u}^0(\boldsymbol{x})$ and $\boldsymbol{u}^1(\boldsymbol{x})$ as well as the virtual displacement fields $\delta\boldsymbol{u}^0(\boldsymbol{x})$ and $\delta\boldsymbol{u}^1(\boldsymbol{x})$ are discretized according to the XFEM approach (3.21) such that

$$N_I^0\left(\boldsymbol{x}_J^0\right) = \delta_{IJ} \quad \text{in } \Omega^0, \tag{4.4}$$

$$N_I^1\left(\boldsymbol{x}_J^1\right) = \delta_{IJ} \quad \text{in } \Omega^1, \tag{4.5}$$

holds for the bi-/trilinear shape functions $N_I^0(\boldsymbol{x})$ and $N_I^1(\boldsymbol{x})$. Here, $\boldsymbol{x}_J^0$ and $\boldsymbol{x}_J^1$ are the nodal supports of the coarse and the fine scale respectively. Thus, both sets of shape functions resemble each other, i.e. $N_I^0(\boldsymbol{x}) = N_I^1(\boldsymbol{x})$, only if the fine scale mesh matches the coarse scale mesh. The enrichment scheme is adopted from the XFEM approach as introduced in section 3.2.2 and is applied according figure 3.5 for both domains yielding the discretized weak forms for both domains.

4.2 Continuity condition

While the coarse scale domain Ω^0 undergoes deformation due to externally applied loads $\overline{\boldsymbol{t}}$ and displacements $\overline{\boldsymbol{u}}$ on its NEUMANN boundaries $\partial\Omega_t^0$ and its DIRECHLET boundaries $\partial\Omega_u^0$ respectively, the fine scale domain Ω^1 generally does not contain these boundaries. The fine scale domain deforms due to the macro displacement field or due to tractions acting on $\partial\Omega^1$. In order to maintain continuity in the displacement field $\boldsymbol{u}^1(\boldsymbol{x})$ and with the assumption $\tilde{\boldsymbol{u}}^1(\boldsymbol{x}) = \boldsymbol{0}$ in $\Omega^0 \setminus \Omega^1$, physically consistent boundary conditions for the fine scale can be formulated using (4.1)

$$\tilde{\boldsymbol{u}}^1(\boldsymbol{x}) = \boldsymbol{0} \quad \Leftrightarrow \quad \boldsymbol{u}^1(\boldsymbol{x}) - \boldsymbol{u}^0(\boldsymbol{x}) = \boldsymbol{0} \quad \text{for } \boldsymbol{x} \in \partial\Omega^1 \quad . \tag{4.6}$$

As the macro displacement field $\boldsymbol{u}^0(\boldsymbol{x})$ can be computed, the micro displacement field on the boundary $\partial\Omega^1$ can be determined and applied as displacement boundary conditions. Thus, all degrees of freedom of all nodes on $\partial\Omega^1$ have a prescribed displacement value, i.e.

$$\partial\Omega_u^1 = \partial\Omega^1 \quad , \quad \overline{\boldsymbol{u}}^1(\boldsymbol{x}) = \boldsymbol{u}^1(\boldsymbol{x}) \quad \text{for } \boldsymbol{x} \in \partial\Omega^1 \quad . \tag{4.7}$$

Applying pure displacement boundary conditions on $\partial\Omega^1$, the last term of (4.3) vanishes naturally as long as the crack face remains totally traction free, i.e.

$$\int_{\partial\Omega_t^1} \overline{\boldsymbol{t}} \cdot \delta\boldsymbol{u}^1 \, \mathrm{d}a = 0 \quad . \tag{4.8}$$

When using a standard FE approach and the multiscale projection method, the micro displacement field on the boundary can be extracted from the macro displacement field in a postprocessing step using (4.6) by evaluating the macro displacement field via the nodal shape functions $N_I^0(\boldsymbol{x})$ at the nodal supports of the micro domain on its boundary

$$\boldsymbol{u}^1\left(\boldsymbol{x}_J^1\right) = \sum_{I=1}^{n_n} N_I^0\left(\boldsymbol{x}_J^1\right) \, \boldsymbol{u}_I^0 \quad \text{for } \boldsymbol{x}_J^1 \in \partial\Omega^1 \quad . \tag{4.9}$$

However, when combining the XFEM and the proposed multiscale method, the above mentioned procedure is not applicable as enriched nodes on $\partial\Omega^1$, appearing naturally due to the existing macrocracks in Ω^1, contain more than one degree of freedom per mesh direction and can thus not simply be evaluated as when non-enriched nodes. Multiplying (4.6) with the virtual displacement $\delta\boldsymbol{u}^1$, i.e. fulfilling (4.6) not exactly but in a least-square sense, and integrating over the domain Ω^1 yields a projection of the displacement boundary conditions

$$\int_{\Omega^1} \left(\boldsymbol{u}^1(\boldsymbol{x}) - \boldsymbol{u}^0(\boldsymbol{x})\right) \cdot \delta\boldsymbol{u}^1(\boldsymbol{x}) \, \mathrm{d}v = 0 \quad . \tag{4.10}$$

The reason for integrating over the domain Ω^1 instead of the surface $\partial\Omega^1$ or a small strip of elements $\tilde{\Omega}^1 \subset \Omega^1$ is illustrated in figure 4.3: Node A and B are both HEAVISIDE enriched, since the macrocrack Γ_c intersects the corresponding element. Integrating only over $\partial\Omega^1$ would result in linear dependency of standard degrees of freedom and HEAVISIDE enriched degrees of freedom as the crack does not intersect the boundary between node A and B. To

overcome this issue, the crack geometry with respect to the whole element needs to be taken into account by integrating over element e. Assuming an integration over the subdomain $\tilde{\Omega}^1$ still results in linear dependency of standard degrees of freedom and HEAVISIDE enriched degrees of freedom: Node C in figure 4.3 is HEAVISIDE enriched, but the discontinuity requiring this enrichment function is in element g, with $g \notin \tilde{\Omega}^1$. Thus, integration over $\tilde{\Omega}^1$ leads to linear dependency of standard and enriched degrees of freedom of node C. Enlarging the width of $\tilde{\Omega}^1$ does not ensure that these linear dependencies do not occur anymore. Consequently the integration is performed over the whole fine scale domain Ω^1, as suggested by LOEHNERT & MUELLER-HOEPPE (2008).

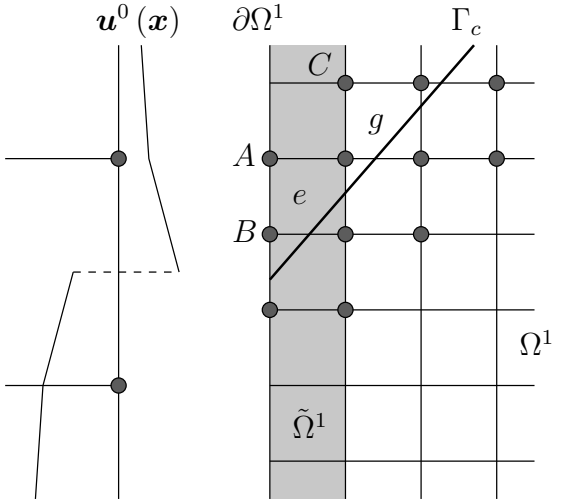

Figure 4.3: Applying macro displacement field $\boldsymbol{u}^0(\boldsymbol{x})$ on the boundary of the fine scale domain $\partial\Omega^1$. HEAVISIDE enriched nodes are encircled.

Applying the displacement field approximations to (4.10) yields a linear system of equations. The solution of (4.10) for non-enriched nodal displacements is known, once the coarse scale problem is solved and can be determined in a single postprocessing step using the introduced XFEM interpolation

$$\begin{aligned}\boldsymbol{u}^1\left(\boldsymbol{x}_L^1\right) = &\sum_{I\in\mathcal{I}^0} N_I^0\left(\boldsymbol{x}_L^1\right)\,\boldsymbol{u}_I^0 + \sum_{J\in\mathcal{J}^0}\sum_{j=1}^{4} N_J^0\left(\boldsymbol{x}_L^1\right) f_j\left(\boldsymbol{x}_L^1\right)\,R^0\left(\boldsymbol{x}_L^1\right)\,\boldsymbol{a}_{Jj}^0 \\ &+ \sum_{K\in\mathcal{K}^0} N_K^0\left(\boldsymbol{x}_L^1\right)\,H\left(\boldsymbol{x}_L^1\right)\,\boldsymbol{b}_K^0 \qquad \text{for } \boldsymbol{x}_L^1 \in \Omega^1 \text{ with } L \notin \mathcal{K}^1, \mathcal{J}^1.\end{aligned} \tag{4.11}$$

Thus, the least-square projection problem (4.10) is comparably small as merely a few degrees of freedom are unknown. The solution of (4.10) and (4.11) yields the required displacement boundary conditions $\overline{\boldsymbol{u}}^1\left(\boldsymbol{x}_I^1\right) = \boldsymbol{u}^1\left(\boldsymbol{x}_I^1\right)$ with $\boldsymbol{x}_I^1 \in \partial\Omega^1$ to solve the fine scale domain problem (4.3).

4.3 Solution procedure

Even though the coarse and fine scale domains as well as the fine scale boundary conditions,

i.e. the continuity condition, can be solved, the overall solution procedure requires special attention as a consequence of the weak coupling of the scales: Due to the generally non-zero micro fluctuation field $\tilde{\boldsymbol{u}}^1$ resulting from the presence of microcracks, the coarse scale residual will not decrease below the desired tolerance within one iteration step, not even for linear elastic problems. Consequently, an iterative solution procedure over i steps needs to be applied here:

1. Initialize values:

   $$i = 0 \quad , \quad \tilde{\boldsymbol{u}}_i^1 = \boldsymbol{0} \quad , \quad \boldsymbol{u}_i^0 = \boldsymbol{0}$$

2. Solve coarse scale problem (4.2):

   $$\boldsymbol{K}_T^0 \cdot \Delta \boldsymbol{u}_i^0 = \boldsymbol{f}^0 \left(\boldsymbol{u}_i^1 \right) \quad \rightarrow \quad \boldsymbol{u}_{i+1}^0 = \boldsymbol{u}_i^0 + \Delta \boldsymbol{u}_i^0$$

3. Project coarse scale displacement field onto the boundary of fine scale domains (4.10), (4.11):

   $$\int_{\Omega^1} \left(\boldsymbol{u}^1 \left(\boldsymbol{x} \right) - \boldsymbol{u}^0 \left(\boldsymbol{x} \right) \right) \cdot \delta \boldsymbol{u}^1 \left(\boldsymbol{x} \right) \, \mathrm{d}v = 0 \quad \rightarrow \quad \overline{\boldsymbol{u}}_i^1 \text{ on } \partial\Omega^1$$

4. Solve fine scale problems (4.3):

   $$\boldsymbol{K}_T^1 \cdot \boldsymbol{u}_{i+1}^1 = \boldsymbol{f}^1 \quad \rightarrow \quad \boldsymbol{u}_{i+1}^1 \quad \rightarrow \quad \boldsymbol{f}^0 \left(\boldsymbol{u}_{i+1}^1 \right)$$

5. Check coarse scale residual for the updated micro fluctuation field $\boldsymbol{f}^0 \left(\boldsymbol{u}_{i+1}^1 \right)$

   (a) Convergence $\rightarrow$ stop computation.

   (b) No convergence $\rightarrow$ $i = i + 1$, goto step 2.

One can see easily from the above sketched solution scheme, that the weak coupling between the scales, due to the non-consistent linearized tangent $\boldsymbol{K}_T^0$ in Ω^1, might involve several iteration steps until convergence is achieved.
Advantageously, in linear elasticity the tangent stiffness matrices $\boldsymbol{K}_T^0$ and $\boldsymbol{K}_T^1$ do not change during computation: If iterative solvers are used, all tangent stiffness matrices needs to be assembled once, such that $\boldsymbol{K}_T^0$ and $\boldsymbol{K}_T^1$ could be stored and used until convergence is achieved. In case direct solvers are applied even the LU decomposition could be stored, decreasing the computational costs extremely. Once cracks propagate within the multiscale framework as explained in sections 5.1.2 and 5.3.2, the tangent stiffness matrices require an update.
Due to the weak coupling, all non-overlapping fine scale domains are independent of each other such that their computation could be parallelized relatively easily. In this work, the projection of the coarse scale displacement field as well as solving the fine scale problem is performed on one CPU for each fine scale region using OPENMP. Even though parallelizations with OPENMP are restricted to one computer core, the computations in this work are performed on systems with up to 64 CPUs such that 64 fine scale domains can be computed in parallel leading to a significant speedup compared to sequential computations.

Reviewing the geometrical regularization techniques, introduced in section 3.2.4 in figure 3.10, in terms of the multiscale projection method reveals once more the benefit of the applied stabilization technique introduced by LOEHNERT (2013). Applying one of these geometrical mesh regularization techniques to the multiscale projection method requires special attention, when the fine scale mesh requires regularization. If this fine scale regularization requires that the node being moved is on the surface of the corresponding coarse scale element, the fine scale element does not match its coarse scale element boundaries. Therefore, integrations of refined coarse scale elements, performed as a sum over their fine scale elements,

$$\int_{\Omega_e^0} (\dots)\, \mathrm{d}v = \sum_{i=1}^{n_e^1} \int_{\Omega_{e;i}^1} (\dots)\, \mathrm{d}v \quad , \tag{4.12}$$

might yield incorrect results. Here, n_e^1 is the number of fine scale elements in the current coarse scale element.

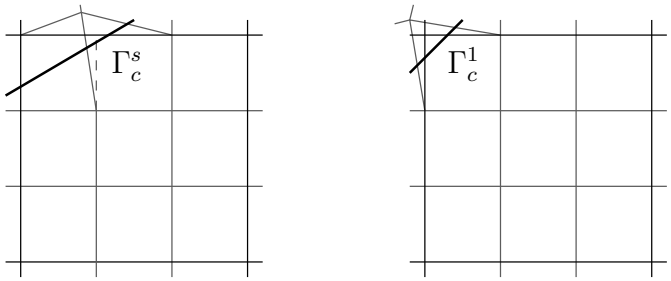

(a) Crack of scale s yields fine scale regularization.

(b) Microcrack requires regularization.

Figure 4.4: Coarse scale elements (solid, black); fine scale elements (solid, gray); initial fine scale elements (solid, gray, dashed); fine or coarse scale crack (solid, black, bold).

Examples of such situations are displayed in figure 4.4: In (a) either a fine or coarse scale crack is cutting off a node of a fine scale element, such that the volume of the coarse scale element remains, while a fine scale node needs to be moved. This situation could be overcome by moving nodes only on the surface of coarse scale elements, which is unfortunately not applicable to the second example displayed in figure 4.4(b): Since the coarse scale element incorporates the microcrack only implicitly, i.e. via the projection of the stress field, the coarse scale node is not moved. As the volume of the fine scale element needs to be enlarged and the node cannot be moved on the surface of the coarse scale element while keeping this volume, the node needs to be moved in or against normal direction. Thus, the volume of coarse scale element does not match the sum over the corresponding fine scale elements, such that (4.12) would not be applicable. To overcome this issue, the coarse scale element should be modified instead of fine scale elements especially when fine scale nodes on the coarse scale element boundary need a shift. The strategy is applicable to all possible crack configurations, but involves a computationally expensive communication between scales.
Other geometrical regularization techniques do not overcome this issue. Moving the crack instead of the FE mesh leads to similar problems for macrocracks: Some quadrature points

on the fine scale might lie on the other side of the crack than on the coarse scale. This feature would yield a non-converging overall problem. In contrast to geometrical regularization methods, the applied stabilization technique does neither change the crack geometry nor the FE mesh, which makes it highly suitable in the context of the multiscale projection method. However, the projection matrix (4.10) requires stabilization as well, which can be computed analogously to the introduced procedure.

Chapter 5

Crack propagation using the XFEM

This chapter introduces crack propagation and crack coalescence using the extended finite element method. In section 5.1, crack propagation is discussed for two-dimensional problems on one scale, followed by multiscale crack propagation. Merging cracks are introduced in section 5.2 with an extension to the multiscale framework. Finally, crack propagation for three-dimensional problems is presented in section 5.3. After setting the basis for computations on one scale, the approach is embedded into the multiscale projection method.

5.1 2D crack propagation

For two-dimensional problems, crack propagation in quasi-static linear elastic fracture mechanics using the XFEM has been successfully applied by MOËS ET AL. (1999) among others. Here, the XFEM reveals its great benefit of mesh independent crack description: Only the level set functions and with it the enrichment functions require an update, while the mesh remains untouched. In this section, the numerical implementation of the crack growth algorithm for singlescale analysis 5.1.1 and for multiscale problems 5.1.2 are introduced.

5.1.1 Crack propagation on one scale

Even though the theory of LEFM as well as XFEM have been briefly revisited in previous chapters, their coupling to model fracturing solids requires a manipulation of the J-integral, a scheme to update crack path and nodal enrichments as well as a strategy to solve the global problem.

Numerical application of the *J*-integral

In order to evaluate the proposed crack growth criteria, the interaction integral $I^{(1,2)}$ needs to be computed. A precise numerical integration of singular functions, i.e. stresses and strains, is most difficult and usually inaccurate according to MORAN & SHIH (1987a). As these line integrals are path-independent, the contour of the integration is chosen to be outside the singular enriched domain. Disadvantageously, line integrals performed in the finite element method, usually lead to inaccuracies as denoted by MORAN & SHIH (1987a), MOËS ET AL.

(1999) among others. Multiplying (2.79) with an arbitrary smoothing function $q(\boldsymbol{x})$ and applying the divergence theorem yields the domain form of the interaction integral following MORAN & SHIH (1987a)

$$I^{(1,2)} = \int_A \left(\sigma_{ij}^{(1)} \frac{\partial u_i^{(2)}}{\partial \boldsymbol{g}_1} + \sigma_{ij}^{(2)} \frac{\partial u_i^{(1)}}{\partial \boldsymbol{g}_1} - W^{(1,2)} \delta_{1j} \right) \frac{\partial q}{\partial \boldsymbol{g}_j} \, \mathrm{d}A \quad . \tag{5.1}$$

The arbitrary smoothing function $q(\boldsymbol{x})$ is set to zero on non-front enriched nodes and to one on front enriched nodes

$$q(\boldsymbol{x}_I) = \begin{cases} 0 & \text{if } I \notin \mathcal{J} \\ 1 & \text{if } I \in \mathcal{J} \end{cases} \quad . \tag{5.2}$$

In between these nodal sets, $q(\boldsymbol{x})$ is interpolated using the finite element shape functions (3.7) leading to a C^0-continuous distribution of $q(\boldsymbol{x})$, displayed in figure 5.1. The integration only needs to be carried out in elements, in which $q(\boldsymbol{x})$ is not constant: In elements with a constant weighting function $q(\boldsymbol{x})$, the integral (5.1) is zero, as $\frac{\partial q(\boldsymbol{x})}{\partial \boldsymbol{g}_j} = \boldsymbol{0}$. Ensuring non-singular shape functions within the integrated domain leads to excellent results as demonstrated by e.g. MOËS ET AL. (1999). With this highly accurate computation of the SIFs, the criterion for crack propagation (2.68), (2.86) as well as the direction of crack growth (2.88) can be determined.

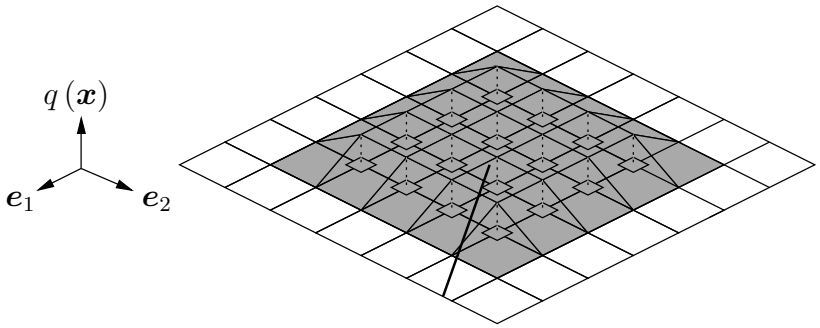

Figure 5.1: Weighting function $q(\boldsymbol{x})$ for two-dimensional problems. Here, crack front enriched nodes are boxed.

Instead of the computation of J, HÄUSLER ET AL. (2011) apply the material force concept to model crack growth in LEFM with the XFEM, achieving a similar accurate criterion for crack growth. These similar results are consistent with balance of energy at the crack front introduced in section 2.6, such that the material force concept seems to be an appropriate alternative to the ring integral.

Updating crack path and enrichment scheme

If the criterion for crack growth is fulfilled, i.e. $\mathcal{G} \geq \mathcal{G}_c$, the crack is advancing in direction of θ_c. While the angle is known, the increment of growth Δa is unknown and needs to be set in quasi-static analysis. As cracking is an irreversible process in this work, the increment of crack growth needs to be small enough to follow the correct path, but it still should be large

enough to keep computation time within reasonable bounds. In this work the increment of growth is chosen to be about half the characteristic length h_e of the finite element containing the crack tip, i.e. $\Delta a \approx h_e/2$.
Due to the representation of cracks via level sets, the update of the crack surface does not require remeshing and thus is a fairly simple process, displayed in figure 5.2. Evaluating the criterion of maximum hoop stress (2.88) yields the new position of the crack tip, which is connected to the intersection point $\boldsymbol{x}_p$ of the crack tip element with the crack. All nodes of elements that are intersected by this new segment are updated according to the level set definition (3.16). As cracks are straight in the reference element and thus bilinear in the current configuration, nodal level sets are updated in the isoparametric configuration to avoid the need for an iterative scheme to determine the distance in new crack tip elements. The enrichment scheme, i.e. the nodal subsets $\mathcal{K}$, $\mathcal{J}$ and $\mathcal{J}^\star$, are updated as introduced in section 3.2.2, such that the enrichment scheme matches the new crack configuration.

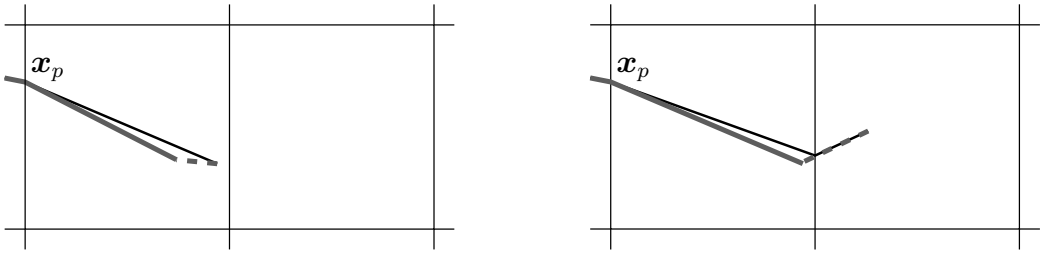

(a) Crack tip remains in finite element. (b) Crack tip advances in other element.

Figure 5.2: Level set update: Old crack path (solid, gray); extension of old path (dashed, gray); new crack path (solid, black).

Overall numerical procedure

The new crack configuration naturally leads to new SIFs for all crack tips in the domain and often to the growth of numerous cracks as well as to instabilities, since the criterion of crack growth might be always fulfilled. To avoid this instability and to follow the solution path, which might be a snap-back problem, load control introduced by MOËS & BELYTSCHKO (2002) and BUDYN ET AL. (2004) is applied. Multiplying the current boundary conditions with a load factor λ

$$\begin{aligned} \overline{\boldsymbol{t}}_{(j+1)} &= \lambda\, \overline{\boldsymbol{t}}_{(j)} \quad , \\ \overline{\boldsymbol{u}}_{(j+1)} &= \lambda\, \overline{\boldsymbol{u}}_{(j)} \quad , \\ \lambda &= \sqrt{\frac{\mathcal{G}_c}{\max\left(\mathcal{G}\right)}} = \frac{\sigma_c}{\max\left(\sigma_{\theta\theta}\left(\theta_c\right)\right)} \quad , \end{aligned} \tag{5.3}$$

yields $\max\left(\mathcal{G}\right) = \mathcal{G}_c$, such that crack growth is just occurring in the next load step $(j+1)$. Here, $\max\left(\sigma_{\theta\theta}\left(\theta_c\right)\right)$ and $\max\left(\mathcal{G}\right)$ are the maximum hoop stress and the maximum energy release rate respectively, among all crack tips at step $(j+1)$. Thus, the highest hoop stress in

the system is equal to its threshold value σ_c resulting in a stable system. As in linear elastic fracture mechanics, the boundary conditions depend linearly on the SIFs and thus linearly on the hoop stress, such that no iteration of λ is needed.
Since this instability might occur in the beginning of the computation, the load of the initial configuration requires adjustment as well. This procedure furthermore ensures crack propagation at each time step, as the load is adopted such that the crack just propagates. Due to numerical inaccuracies in the order of 10^{-13}, the criterion for crack propagation might not be fulfilled exactly. With an infinitesimal small amount of additional load in the following solution step, at least one crack tip fulfills the criterion for crack growth. Thus, the number of propagation steps n_{prop} becomes a user defined variable to control the computational time. This finally yields the numerical implementation displayed in table 5.1.

loop, number of propagation steps n_{prop}	
solve for displacement field	(2.60)
update boundary conditions	(5.3)
solve for displacement field	(2.60)
perform crack propagation according to section 5.1.1	
end loop	
solve for displacement field	(2.60)
update boundary conditions	(5.3)
solve for displacement field	(2.60)

Table 5.1: Overall numerical procedure to perform crack propagation.

Three-point bending test

A famous experiment in the XFEM community to test accuracy was proposed by INGRAFFEA & GRIGORIU (1990): The two-dimensional structure, given in figure 5.3 with a thickness of $12.7\,\text{mm}$ and $a = 25.4\,\text{mm}$, is made of the brittle material CYRO ACRYLITE FF PLEXIGLAS MC with YOUNG's modulus $E = 3.1\,\text{GPa}$ and POISSON's ratio $\nu = 0.4$. Unfortunately, for this test neither a load deflection curve nor an energy release is published, but only the resulting crack path. Therefore no critical SIFs K_{Ic}, hoop stresses σ_c or energy release rates $\mathcal{G}_c$ are required and only the crack paths are compared. As the crack path strongly depends on the SIFs K_{I} and K_{II} (2.88), similar crack paths state their correct evaluation.
As displayed in figure 5.3, the structure contains a slit, i.e. it is precracked, which is an essential ingredient for XFEM applications. Furthermore, the structure contains three holes, which are points of stress concentrations and thus affect the crack trajectory.
The experimental and the computed crack paths are displayed in figure 5.3: The crack tip is attracted by the hole reached first, but its influence on the direction of growth is insufficient for turning the crack into the hole. The path turns towards the centered hole until the tip finally reaches this hole.
These observations hold true for the experiment as well as numerical model. In the center of the paths some minor differences are noticed, but both paths coincide: The model is capturing the effects of the LEFM remarkably well.

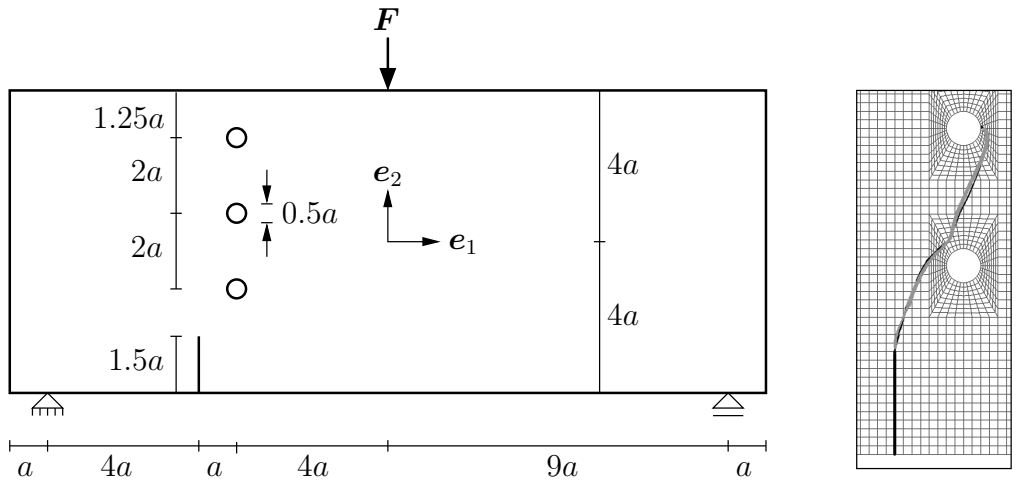

Figure 5.3: Left: Setup of experiment performed by INGRAFFEA & GRIGORIU (1990). Right: Experimental crack path (black) and numerical crack path (gray) for 10,912 elements.

Limits of the proposed model

Even though this model sounds generally applicable in the context of LEFM, it is still limited in some cases: A precise computation of the interaction integral can only be performed in a mesh dependent distance of the crack tip. Thus, an accurate evaluation is not possible close to the boundary of the domain. BUDYN ET AL. (2004) and BUDYN (2004) connect the crack tip to the free surface regardless of the applied boundary conditions, as the tip approaches the boundary of the domain and thus avoid inaccurate SIFs. As only a small strip of elements remains before complete failure, the computation is stopped in this work instead of searching the closest point on the boundary of the domain.
Additionally, the proposed crack propagation model is not able to compute merging cracks: If crack trajectories intersect, the computation is stopped as soon as some nodes require two enrichment functions as well as four level set functions, to describe two cracks within a single finite element. As enrichments cannot simply be added to the displacement field approximation, but influence each other depending on the crack geometry, merging cracks require special treatment, introduced by DAUX ET AL. (2000) and revisited in this work in section 5.2.1. Similar to the above mentioned restriction of a crack advancing towards the boundary of a domain, the J-integral cannot be evaluated precisely, if another singular function is inside the domain, in which this integral is carried out. Consequently, crack fronts must keep a certain distance, depending on the finite element mesh at the crack fronts.
Furthermore, this model does not avoid penetrating crack faces naturally: A contact formulation would provide a remedy as shown by DOLBOW ET AL. (2001) among others, but also lead to non-linear systems of equations and thus to time consuming iterative solution procedures. Contact problems are not the main objective of this work and are thus omitted for simplicity. An elegant way to estimate crack face penetration without solving a contact problem is done via the SIFs: If $K_{\mathrm{I}} < 0$ crack faces penetrate. Since curved cracks are investigated as well, this statement does not hold vice versa, as the penetration might occur far away from the crack tip.

5.1.2 Multiscale crack propagation

Utilizing this proposed method to the introduced multiscale projection method requires extension of existing theory and FEM code, introduced by HOLL ET AL. (2013):
As two scales are considered here, the criterion for crack propagation might be fulfilled on the fine scale, but not on the coarse scale, in case of propagating microcracks: These cracks are only known implicitly on the coarse scale, such that the J-integral cannot be evaluated there. Therefore, the criterion of crack propagation needs to be evaluated on the fine scale. Furthermore, computations on fine scales are more accurate than coarse scale computations. In contrast to microcracks, advancing macrocracks influence the coarse scale explicitly, such that the macrocrack geometry, computed on the fine scale, needs to be transferred to the coarse scale. Generally, propagation of coarse scale cracks does not yield a single bilinear function in one coarse scale element, as displayed in figure 5.4, with the possibilities of a crack remaining in the same coarse scale element (figure 5.4(a)) and entering a new coarse scale element (figure 5.4(b)). Here, the level set update for an advancing macrocrack follows the same strategy as explained in section 5.1.1, while the crack interpolation, using bilinear shape functions, is carried out on the coarse scale mesh instead of the fine scale mesh. Interpolating a macrocrack using shape functions N^1, would yield a more accurate macrocrack geometry approximation but also the loss of bilinearity in one element and thus a fairly complicated crack description. As scale coupling is the main interest here, this feature is omitted for brevity. Thus, in this work, a higher macrocrack resolution can only be achieved with coarse scale mesh refinement.
Propagating microcracks do not necessitate special treatment, as the implicit microcrack description on the coarse scale does neither influence the coarse scale geometry nor the coarse scale enrichment scheme.

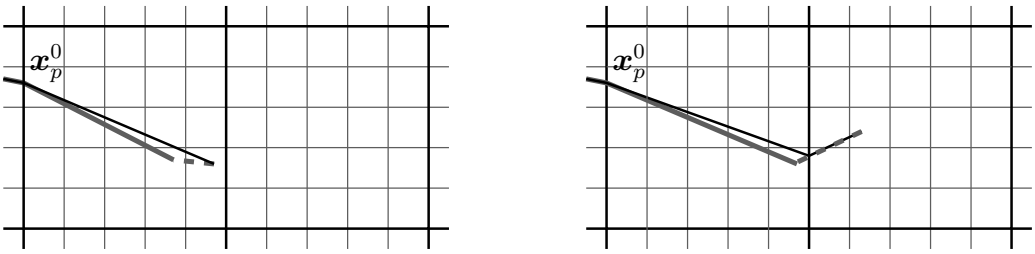

(a) Crack tip remains in finite element. (b) Crack tip advances in other element.

Figure 5.4: Level set update: Old crack path (solid, gray); extension of old path (dashed, gray); new crack path (solid, black). Each coarse scale element (black) is subdivided into 5×5 fine scale elements (gray).

Analogous to section 5.1.1, each propagation step is followed by an adaption of the coarse scale load factor λ^0 to maintain stability, i.e.

$$\max\left(\sigma_{\theta\theta}^1\left(\theta_c, \lambda^0\right)\right) = \sigma_c \quad . \tag{5.4}$$

Since the load is applied on the boundary of the coarse scale mesh, but the maximum hoop stress is evaluated on the fine scale, an iterative solution scheme needs to be applied to

determine the new load factor λ^0 within the presented multiscale framework. In the following equations, the superscript $(\cdot)^0$ denotes coarse scale variables, while the superscript $(\cdot)^1$ denotes fine scale variables. Rewriting (5.4)

$$R\left(\lambda^0\right) = \max\left(\sigma^1_{\theta\theta}\left(\theta_c, \lambda^0\right)\right) - \sigma_c = 0 \quad , \tag{5.5}$$

and application of a NEWTON scheme

$$\lambda^0_{(i+1)} = \lambda^0_{(i)} + \left(\frac{\partial R\left(\lambda^0_{(i)}\right)}{\partial \lambda^0}\right)^{-1} \cdot R\left(\lambda^0_{(i)}\right) \quad , \tag{5.6}$$

yields the next iterate $\lambda^0_{(i+1)}$ for the unknown load factor λ^0. With the finite difference approximation

$$\left(\frac{\partial R\left(\lambda^0_{(i)}\right)}{\partial \lambda^0}\right)^{-1} \approx \frac{\lambda^0_{(i)} - \lambda^0_{(i-1)}}{R\left(\lambda^0_{(i)}\right) - R\left(\lambda^0_{(i-1)}\right)} \quad , \tag{5.7}$$

the unknown load factor can be determined for the next load step. Once the residual $R\left(\lambda^0_i\right)$ decreases below a user defined tolerance TOL

$$\| R\left(\lambda^0_{(i)}\right) \| < \text{TOL} \approx 0 \quad , \tag{5.8}$$

the iteration is stopped. Initializing the iterates appropriately, i.e. $\lambda^0_{(1)} = \lambda^1_{(1)}$, $\lambda^0_{(0)} = 0$ and $\max\left(\sigma^1_{\theta\theta}\left(\theta_c, \lambda^0_{(0)}\right)\right) = 0$, yields a solution of the problem using an adequate number of iteration steps $i = 1, 2, 3, ...n$. Analogously to singlescale computations, the current traction and displacement boundary conditions on the coarse scale, i.e. $\overline{\boldsymbol{t}}^0_{(j)}$, $\overline{\boldsymbol{u}}^0_{(j)}$, are finally multiplied with the converged load factor $\lambda^0_{(i)}$

$$\overline{\boldsymbol{t}}^0_{(j+1)} = \lambda^0_{(i)}\, \overline{\boldsymbol{t}}^0_{(j)} \quad , \quad \overline{\boldsymbol{u}}^0_{(j+1)} = \lambda^0_{(i)}\, \overline{\boldsymbol{u}}^0_{(j)} \quad , \tag{5.9}$$

such that crack propagation is just occurring in the next load step $(j+1)$.
Note that the maximum hoop stress for each microcrack tip as well as macrocrack tip needs to be evaluated on the fine scale. This might involve several fine scale domain computations within each propagation step for the current global load factor, since the crack tip with the highest hoop stress needs to be found. Due to the fact that the criterion for crack propagation as well as the direction of crack growth is computed on the fine scale, the crack development on the coarse scale is fully driven by the fine scale results.
Apart from the computation of the coarse scale load factor λ^0 and the evaluation of crack propagation on the fine scale, the multiscale crack propagation technique presented here can be easily implemented in the finite element program, with its solution procedure summarized in table 5.2.

loop, number of propagation steps n_{prop}	
solve for displacement field	section 4.3
update boundary conditions	section 5.1.2
solve for displacement field	section 4.3
perform crack propagation	section 5.1.2
end loop	
solve for displacement field	section 4.3
update boundary conditions	section 5.1.2
solve for displacement field	section 4.3

Table 5.2: Overall numerical procedure to perform multiscale crack propagation.

5.2 2D crack coalescence

Considering fracturing processes containing more than one crack in the investigated domain might result in crack coalescence, reported and numerically investigated by BUDYN (2004), BUDYN ET AL. (2004), MOËS ET AL. (2011), BYFUT & SCHRÖDER (2012) and GARZON ET AL. (2013) among others. In two-dimensional space either two crack tips merge to one longer crack or a crack tip coalesces with a crack face. While the first case does not require any change of the above introduced theory besides a criterion for coalescence, the introduction of new enrichments becomes mandatory for merging a crack tip with a crack face as two cracks and thus two discontinuities in the displacement field need to be approximated. Introducing this extension in section 5.2.1 reveals its sufficiency for singlescale analysis. Following HOLL ET AL. (2013), the assumption of coalescing cracks within the introduced multiscale projection method requires additional enrichments for nearing macrocrack tips, as the criterion for coalescence is investigated on the fine scale. In order to use the coarse scale level set interpolation, a mapping strategy is needed to incorporate a microcrack merged with a macrocrack into the coarse scale domain. The extensions made for crack coalescence within the multiscale projection method are introduced in 5.2.2. Symbols used to illustrate crack coalescence schemes in figures 5.14, 5.13, 5.24 - 5.27 are explained in table 5.3.

Coarse scale mesh	
Fine scale mesh	
Macrocrack	
Microcrack	
Crack propagation	
Shortest distance from new crack tip to crack	
First identified crack path	
Enriched node belonging to propagated crack	
Enriched node of all other cracks	
Enrichment of already propagated crack (the old enrichments (•) will be deleted)	

Table 5.3: Symbols used for crack coalescence sketches.

Even though the following strategy is applicable to an infinite number of cracks per element, this work is restricted to two cracks per element. However, this procedure is still able to demonstrate the major aspects of crack coalescence, as two lines, i.e. cracks, can only intersect at one point. Further cracks will complicate the enrichment scheme but will not yield another intersection geometry than a point.

5.2.1 Crack coalescence on one scale

Two cases of crack coalescence on one scale exist: Either a crack tip merges with another crack tip, resulting in one final crack, or a crack tip coalesces with a crack face, such that the paths of both cracks remain. Merging a crack tip with a crack face naturally yields an intersection point of both cracks. Thus, a single finite element needs to be able to capture the two discontinuities resulting from both cracks, leading to an extension of the extended finite element displacement approximation (3.21), introduced by DAUX ET AL. (2000).
Thus, the integration introduced in section 3.2.3 is not applicable anymore, as integration points on both discontinuities have to be avoided. Since the displacement field approximation for multiscale problems requires consideration of a random combination of crack tips and crack faces, still restricted to two cracks, a hard coded subdivision into triangles as in section 3.2.3 is not favorable. The constrained DELAUNAY triangulation by CHEW (1989) automatically subdivides a quadrilateral into triangles, and with the choice of the crack faces being constrained, quadrature points on crack faces are avoided. The standard DELAUNAY triangulation algorithm is adopted from DE BERG ET AL. (2008), while the constraints are implemented according to CHEW (1989).
Finally, the crack coalescence criterion is embedded into the crack propagation scheme according to table 5.1. In contrast to BUDYN ET AL. (2004) and BUDYN (2004), the crack coalescence criterion depends on the element size, meaning that the finer the finite element mesh, the closer the cracks grow before merging.

Displacement field approximation

Extending the XFEM displacement field approximation for branched cracks yields

$$\begin{aligned}\boldsymbol{u}(\boldsymbol{x}) = &\sum_{I\in\mathcal{I}} N_I(\boldsymbol{x})\ \boldsymbol{u}_I + \sum_{J\in\mathcal{J}}\sum_{j=1}^{4} N_J(\boldsymbol{x})\, f_j(\boldsymbol{x})\ R(\boldsymbol{x})\ \boldsymbol{a}_{jJ} \\ &+ \sum_{i=1}^{n_{\text{cracks}}} \left(\sum_{K\in\mathcal{K}} N_K(\boldsymbol{x}) \left[H^i(\boldsymbol{x}) - H^i_K\right] \left|\left|H^i(\boldsymbol{x})\right|\right| \boldsymbol{b}^i_K \right) \quad ,\end{aligned} \tag{5.10}$$

with $n_{\text{cracks}} = 2$ at the maximum considered in this work. Here, $H^i(\boldsymbol{x})$ is a modified HEAVISIDE enrichment function $H^i = H^i(\boldsymbol{x}) = H(\psi_i(\boldsymbol{x}))$ of the i-th crack. Subtracting the nodal value H^i_K from H^i leads to the so-called shifted HEAVISIDE enrichment function, which is zero outside cracked elements. The formulation of this enrichment function depends on the configuration of the two cracks in the corresponding finite element. For an

element containing intersecting cracks, this function reads

$$H^i = \begin{cases} +1 & \text{if } \psi_i(\boldsymbol{x}) \geq 0 \ \wedge \operatorname{sgn}\left(\frac{\nabla\phi_i}{||\nabla\phi_i||} \cdot \frac{\nabla\psi_j}{||\nabla\psi_j||}\right) \cdot \operatorname{sgn}(\psi_j) = -1 \\ -1 & \text{if } \psi_i(\boldsymbol{x}) < 0 \ \wedge \operatorname{sgn}\left(\frac{\nabla\phi_i}{||\nabla\phi_i||} \cdot \frac{\nabla\psi_j}{||\nabla\psi_j||}\right) \cdot \operatorname{sgn}(\psi_j) = -1 \quad \text{for } i \neq j \ , \\ 0 & \text{if } \operatorname{sgn}\left(\frac{\nabla\phi_i}{||\nabla\phi_i||} \cdot \frac{\nabla\psi_j}{||\nabla\psi_j||}\right) \cdot \operatorname{sgn}(\psi_j) = +1 \end{cases} \tag{5.11}$$

which is applied instead of the so-called junction function by DAUX ET AL. (2000), yielding the same enrichment function in a different notation. In elements with two non-intersecting discontinuities, the second level set functions ϕ_i do not yield an adequate solution for H^i. Hence, a different strategy is applied to set the appropriate enrichment function to zero in the respective domain for elements cracked twice, with non-intersecting cracks. The enrichment function is evaluated using the level set values of the reference point $\boldsymbol{x}_c$

$$H^i = \begin{cases} +1 & \text{if } \psi_i(\boldsymbol{x}) \geq 0 \ \wedge \operatorname{sgn}(\psi_j(\boldsymbol{x})) = \operatorname{sgn}(\psi_j(\boldsymbol{x}_c)) \\ -1 & \text{if } \psi_i(\boldsymbol{x}) < 0 \ \wedge \operatorname{sgn}(\psi_j(\boldsymbol{x})) = \operatorname{sgn}(\psi_j(\boldsymbol{x}_c)) \quad \text{for } i \neq j \ , \\ 0 & \text{if } \operatorname{sgn}(\psi_j(\boldsymbol{x})) \neq \operatorname{sgn}(\psi_j(\boldsymbol{x}_c)) \end{cases} \tag{5.12}$$

which is determined via the intersection points $\boldsymbol{a}_i$ of the cracks, with the finite element

$$\boldsymbol{x}_c = \frac{1}{4}\left(\boldsymbol{a}_1 + \boldsymbol{a}_2 + \boldsymbol{a}_3 + \boldsymbol{a}_4\right) \quad . \tag{5.13}$$

Since the intersection points $\boldsymbol{a}_i$ always form a convex quadrilateral, $\boldsymbol{x}_c$ is always between both cracks, as depicted in figure 5.5.

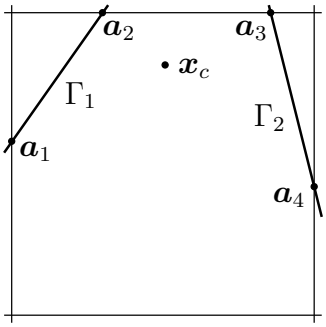

Figure 5.5: Non-intersecting cracks.

The modified HEAVISIDE enrichment function when applied to the displacement field approximation (5.10) yields zero values in domains where the corresponding crack is physically inactive, i.e. by another crack shielded area. From (5.11), (5.12) one can see that the new enrichment function can be evaluated in terms of the level set function and thus provides a fast computational framework. HEAVISIDE enrichment functions of elements containing one crack are evaluated using the standard XFEM approach (3.24). The difference of the introduced modified HEAVISIDE enrichment function to the standard XFEM approach is displayed in figure 5.6 and 5.7. Consider a domain Ω cut by two intersecting cracks Γ_1 and Γ_2. These cracks subdivide the domain in three subdomains, i.e. Ω_1, Ω_2 and Ω_3, displayed in figure 5.6.

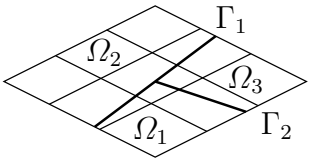

Figure 5.6: Domain Ω divided into subdomains Ω_1, Ω_2 and Ω_3.

As the crack Γ_1 is active in all subdomains, the corresponding HEAVISIDE enrichment function $H^1(\boldsymbol{x})$, displayed in figure 5.7(a), does not change compared to the standard XFEM approach. In contrast to $H^1(\boldsymbol{x})$, the second enrichment function $H^2(\boldsymbol{x})$, responsible for modeling the second displacement discontinuity, is changed compared to the standard XFEM approach: The second discontinuity cannot act in the subdomain Ω_2 and therefore the enrichment function needs to vanish there. By evaluating the level set fields according to (5.11), this enrichment function vanishes, i.e. $H^2(\boldsymbol{x}) = 0,\ \forall\ \boldsymbol{x} \in \Omega_2$, displayed in figure 5.7(b). With the multiplication of the absolute value of $H^2(\boldsymbol{x})$ in (5.10), the displacement field approximation of this crack is zero in the corresponding domain.

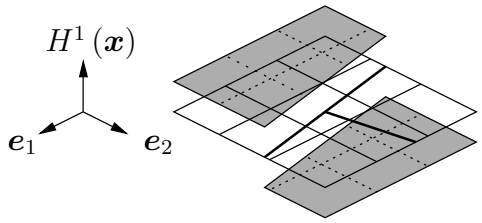

(a) First modified HEAVISIDE enrichment function.

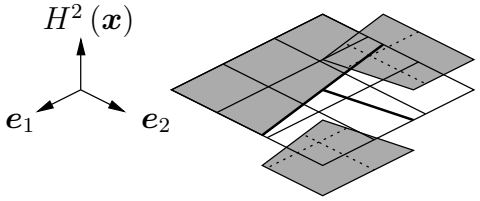

(b) Second modified HEAVISIDE enrichment function.

Figure 5.7: Enrichment functions for intersecting cracks.

To maintain consistent enrichment functions in the whole domain, non-intersecting cracks as displayed in figure 5.8 are enriched as introduced in (5.12). Here, neither of the two cracks Γ_1, Γ_2 have an influence on all subdomains Ω_1, Ω_2 and Ω_3 of the whole domain Ω.

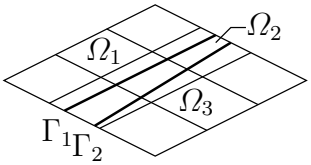

Figure 5.8: Domain Ω divided into subdomains Ω_1, Ω_2 and Ω_3.

Since Γ_2 cuts off Ω_3 from the whole domain, the first enrichment function $H^1(\boldsymbol{x})$ is not active, as displayed in figure 5.9(a). The subdomains Ω_1 and Ω_2 are divided by Γ_1, such that here $H^1(\boldsymbol{x}) = \pm 1$ respectively. The enrichment function $H^2(\boldsymbol{x})$ is determined analogously,

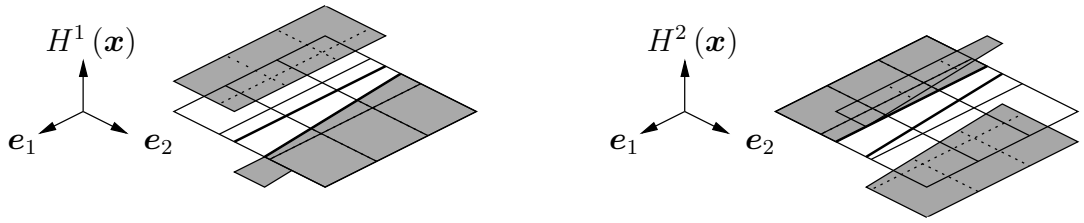

(a) First modified HEAVISIDE enrichment function.

(b) Second modified HEAVISIDE enrichment function.

Figure 5.9: Enrichment functions for non-intersecting cracks.

as Γ_1 cuts off Ω_1, displayed in figure 5.9(b).
In (5.10), the HEAVISIDE enrichments are shifted according to FRIES (2008), leading to non-zero enrichment functions in elements containing cracks, and zero in their neighboring elements due to subtraction of the nodal value $H_K^i = H^i(\boldsymbol{x}_K)$. The application of the shifted basis is beneficial, as less nodal level set values need to be stored and the evaluation in neighboring elements does not require any computation.

Assignment of DOFs and cracks

Furthermore, an assignment between level sets and enrichment functions becomes necessary to ensure that for instance a twice HEAVISIDE enriched node uses the same set of unknowns in all elements containing this node. Therefore, the intersection points of the cracks with the finite elements are determined in a preprocessing step as illustrated in figure 5.10.

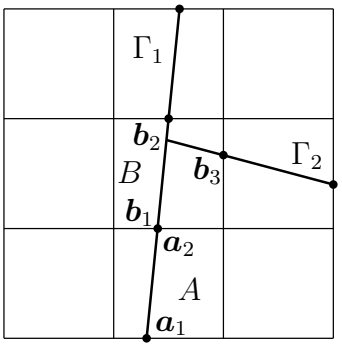

Figure 5.10: Elementwise segmented crack paths.

Here, the intersection points $\boldsymbol{a}_1$ and $\boldsymbol{a}_2$ of element A are compared to the intersection points $\boldsymbol{b}_1$, $\boldsymbol{b}_2$ and $\boldsymbol{b}_3$ of element B. If element A and B have one point in common, one can identify easily which nodal level set values to use in the following computation. A single integer per element stores which crack belongs to which DOFs. If this integer is e.g. $[13]_{10} = [1\,1\,0\,1]_2$, the first set of DOFs of node 1, 3 and 4 belong to the second crack in the element and vice versa. On node 2, the first crack is assigned to the first set of DOFs and the second crack to the second set of DOFs. This preprocessing step only needs to be performed once, as in the ongoing crack propagation computation, one can determine directly which

level set fields are already assigned. With that procedure, a unique assignment from DOFs to the cracks is ensured.

Numerical integration

The "hardcoded" subdivision of cracked elements into triangles/tetrahedrons, introduced in section 3.2.3, is not feasible once two cracks in one element are considered: a vast amount of different subregions with totally different shapes exists, depending on the position of the cracks. With the knowledge that the multiscale analysis will require the consideration of two crack tips in a single element (section 5.2.2) yielding even more cases of crack positions, the "hardcoded" subdivision of twice cracked elements is not applied for elements containing two cracks. An elementwise DELAUNAY triangulation of element nodes, crack tips and intersection points of cracks with the finite element in the reference configuration provides an accurate mesh of triangles within one cracked element, but is naturally not prohibiting quadrature points on cracks: Generated triangles might be flipped to ensure an optimal grid with given points. A constrained DELAUNAY triangulation based on the work of CHEW (1989), with crack faces being constrained triangle sides, avoids quadrature points on the crack face. As this procedure is highly flexible and applicable even to all desired crack geometries for the coming multiscale analysis, it is applied to all twice cracked elements. Figure 5.11 displays a constrained DELAUNAY triangulation for a few different crack positions.

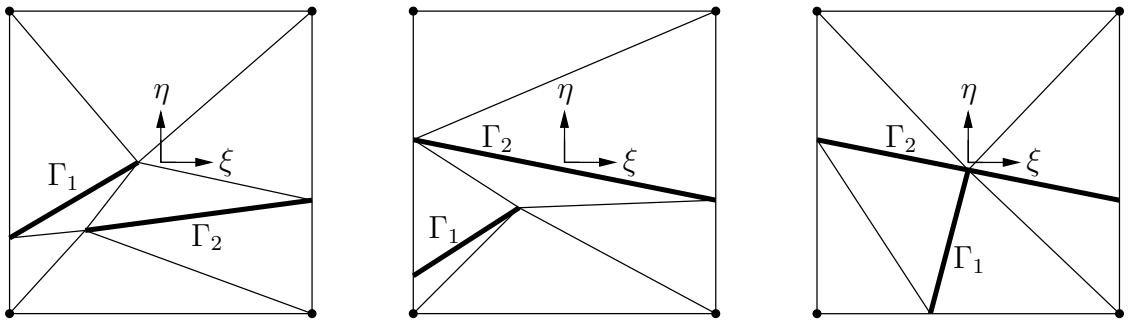

(a) Cracked element containing two crack tips.

(b) Splitted element containing a crack tip.

(c) Two discontinuities in one finite element.

Figure 5.11: Subdivision of twice cracked elements in isoparametric reference configurations.

Computational example

A computational example is given in figure 5.12: A square domain of length 2×2 is loaded uniaxially in $\boldsymbol{e}_1$-direction and is clamped at its top, as displayed in figure 5.12(a). It contains one branched crack ending in eight crack tips. The resulting VON MISES stress is displayed in figure 5.12(b): Stress concentrations occur only at the outer crack tips, as the more centered cracks only open a bit due to crack shielding of the outer cracks. Only slight

stress oscillations can be detected at these crack tips. Negligible small stress gradients occur at the opened bottom branch, meaning that the presented modified HEAVISIDE enrichment function yields traction free crack faces. By taking several branches into account using only two HEAVISIDE enrichment functions, this example demonstrates the great flexibility of the implemented finite element program.

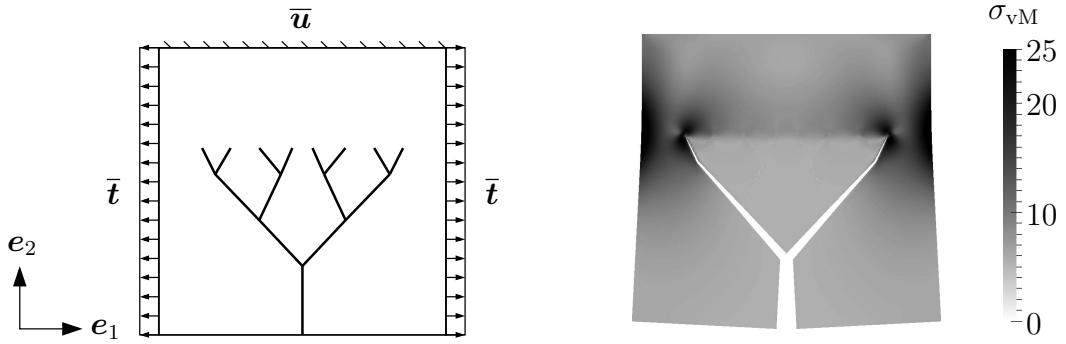

(a) Crack configuration and applied boundary conditions $\overline{\boldsymbol{t}} = \pm\boldsymbol{e}_1$, $\overline{\boldsymbol{u}} = \boldsymbol{0}$.

(b) Distribution of VON MISES stress σ_{vM} on deformed domain.

Figure 5.12: Domain Ω with meshed with 125×125 quadratic elements.

Crack coalescence

Advancing crack tips in a domain with more than one crack induces merging cracks. Here, two different cases are distinguished: Either a crack tip merges with another crack tip, or a crack tip coalesces with a crack face. After setting a new load factor λ, computing crack propagation (- - -) and updating the level set functions according to section 5.1.1, new enrichment functions (◯) need to be set, while the old ones (•) are deleted. If one node requires enrichments from two cracks (◉), these cracks coalesce. From the propagated crack tip, the shortest distance (- - -) to the corresponding crack is determined, and the level set functions are extended, such that both cracks merge at this point. The final crack path (——) as well as new enrichments (•) are set appropriately. Due to bilinear crack description per element, the final crack path slightly differs from the first approximated one (- - -). With mesh refinement, this negligible inaccuracy will vanish.
An example where two crack tips merge is considered in figure 5.13, with symbols used according to table 5.3. In figure 5.13(a), the left crack propagates, such that the resulting enrichments would yield a node being enriched with functions belonging to different cracks. As in this case, the resulting crack path would lead to an inaccurate SIF extraction in the following step, since within the integrated domain of the J-integral only one singular function is allowed, both cracks merge. Connecting both crack tips results in one long crack, with its path displayed in figure 5.13(b).

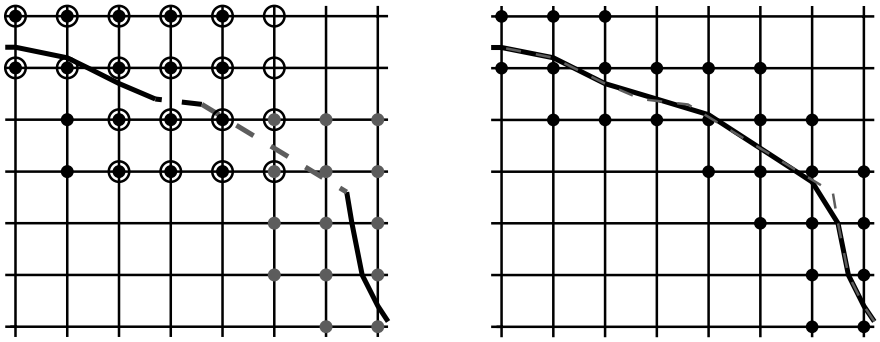

(a) One step before coalescence. (b) Final crack path.

Figure 5.13: Crack coalescence on one scale: Two crack tips merge.

Even though an accurate SIF extraction is generally possible in the second coalescence scenario depicted in figure 5.14(a), the criterion for crack coalescence is retained. Here, an advancing crack tip yields an enrichment scheme, which requires nodal enrichments with functions belonging to different cracks. As only one set of singular functions is needed, the computation of the energy release rate is still possible, but in order to have only one criterion for coalescence, the introduced criterion is kept. Connecting the propagated crack tip via the shortest distance to the crack face of the second crack is displayed in figure 5.14(b).

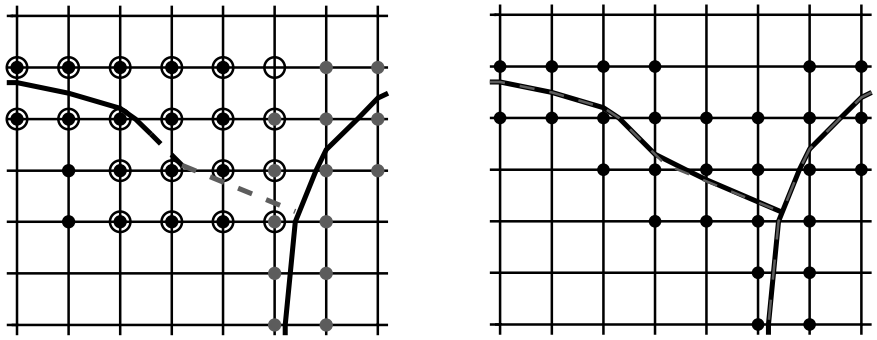

(a) One step before coalescence. (b) Final crack path.

Figure 5.14: Crack coalescence on one scale: Crack tip and crack face coalesce.

Remarks

This procedure allows the modeling crack of coalescence on a singlescale. As the criterion for crack coalescence as well as the domain integrals needed for the evaluation of the energy release rates depends on the finite element mesh, this technique is highly suitable in the XFEM framework. With minor extensions of the displacement field approximation (5.10) and the integration scheme, the presented crack coalescence algorithm can be easily incorporated into the XFEM code. The solution procedure is summarized in table 5.4.

loop, number of propagation steps n_{prop}	
solve for displacement field	(2.60)
update boundary conditions	(5.3)
solve for displacement field	(2.60)
perform crack propagation according to section 5.1.1	
check for crack coalescence according to section 5.2.1	
end loop	
solve for displacement field	(2.60)
update boundary conditions	(5.3)
solve for displacement field	(2.60)

Table 5.4: Overall numerical procedure to perform crack propagation and crack coalescence.

5.2.2 Multiscale crack coalescence

Combining the presented multiscale method with the introduced crack coalescence scheme requires, besides new theoretical tasks, an extensive modification of the FE program:
As microcracks are only known explicitly on the fine scale, crack propagation as well as crack coalescence need to be modeled on the finest scale. This might lead to two approaching crack tips in one coarse scale element, requiring an extension of the introduced displacement field approximation (5.10).
With two crack tips in one finite element, the enrichment scheme and nodal level set storage becomes complicated. To simplify the enrichment scheme and with it the required storage of nodal level set values, a new ramp function $R^\star(\boldsymbol{x})$ is introduced. It is only applied on the coarse scale while the fine scale ramp function remains, i.e. $R^0(\boldsymbol{x}) = R^\star(\boldsymbol{x})$ and $R^1(\boldsymbol{x}) = R(\boldsymbol{x})$. Furthermore, $R^\star(\boldsymbol{x})$ is defined such that only coarse scale elements containing cracks require enrichment functions and nodal level set values.
Finally, crack coalescence is applied on the fine scale. Thus, this model is able to capture different combinations of crack coalescence, i.e. coalescence of cracks on different length scales, which requires an upscaling of fine scale properties to the coarse scale.

Displacement field approximation

As the properties of multiple approaching crack tips on the coarse scale need to be captured, a single finite element must be capable of describing these properties as well. Compared to a standard XFEM approach, a higher amount of nodal level sets and enrichment functions is needed in a single finite element, leading to the following displacement field approximation for scale s

$$\begin{aligned}\boldsymbol{u}^s(\boldsymbol{x}) = \sum_{I\in\mathcal{I}^s} N_I^s(\boldsymbol{x})\ \boldsymbol{u}_I^s + \sum_{i=1}^{n_{\text{cracks}}} \Bigg(\sum_{J\in\mathcal{J}^s} N_J^s(\boldsymbol{x}) \sum_{j=1}^{4} f_j^i(\boldsymbol{x})\ R^s(\boldsymbol{x})\ \boldsymbol{a}_{jJ}^{is} \\ + \sum_{K\in\mathcal{K}^s} N_K^s(\boldsymbol{x}) \left[H^i(\boldsymbol{x}) - H_K^i\right] \left|\left|H^i(\boldsymbol{x})\right|\right| \boldsymbol{b}_K^{is} \Bigg) \quad .\end{aligned} \tag{5.14}$$

Alternative ramp function

To simplify the introduced assignment of cracks to nodal DOFs, especially in blending elements, and to reduce the number of unknowns in the hole domain, a modified ramp function $R^\star = R^\star(\boldsymbol{x})$ is introduced here. It is non-zero in cracked blending and crack tip elements and zero in the rest of the domain. Thus, the following conditions need to be met by this fading out function:

1. Fulfillment of the partition of unity in all elements.
2. Keeping the order of stress singularity at the crack tip.
3. Being zero in elements not cut by a crack.

Reducing the non-zero area of a fading out function to crack tip elements, such that this function is zero on the boundary of these elements, would suppress crack opening as $f_1^0\, R^\star = 0 \,\forall\, \boldsymbol{x} \in \partial\Omega_e$. Thus, the element beyond the crack front element is front enriched as well and multiplied with the fading out function. Consequently, the modified ramp function $R^\star(\boldsymbol{x})$ leads to a different enrichment scheme on the respective scale, displayed in figure 5.15. In contrast to the original version of the ramp function, only six instead of 16 nodes per crack tip belong to the nodal subset $\mathcal{J}^s$ reducing the numerical cost. Furthermore, the evaluation of the J-integral can be performed over a smaller number of elements, as only one blending element of the original set remains enriched with singular functions, yielding a further reduction of the numerical effort.

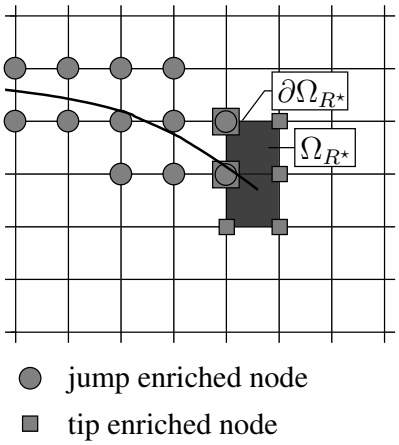

Figure 5.15: Modified ramp function $R^\star(\boldsymbol{x})$.

In order to keep the order of stress singularity of the crack tip,

$$\frac{\partial R^\star(\boldsymbol{x})}{\partial \boldsymbol{x}} = \mathbf{0} \quad \forall \boldsymbol{x} \in \left(\Gamma_c \cap \Omega_{1-4}^{\mathrm{tip}}\right) \quad , \tag{5.15}$$

with $\Omega_{1-4}^{\mathrm{tip}}$ being subdomains of the crack tip element, displayed in figure 5.16(a). In total six subdomains are considered, in which $R^\star(\boldsymbol{x}) \neq 0$: Two domains in the crack tip element in front of the crack tip (Ω_1^{tip}, Ω_3^{tip}), two domains in the crack tip element with their boundary

being the crack path (Ω_2^{tip}, Ω_4^{tip}) and two domains in the blending element (Ω_5^{tip}, Ω_6^{tip}). In each domain two quadratic functions, $r_1(\boldsymbol{x})$ and $r_2(\boldsymbol{x})$, are constructed, which are zero on opposite edges and one on the crack in the crack tip element, displayed in figure 5.16(b), (c). Multiplying both functions yields $R^\star(\boldsymbol{x}) = r_1(\boldsymbol{x}) \cdot r_2(\boldsymbol{x})$, with the desired above mentioned properties, displayed in figure 5.16(d).

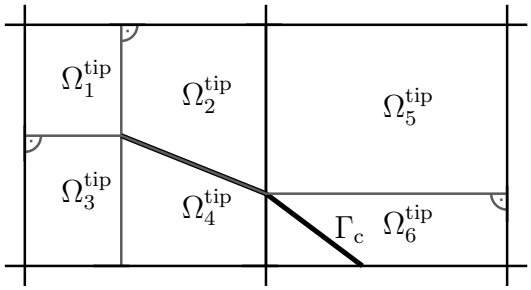

(a) Splitting elements into subdomains.

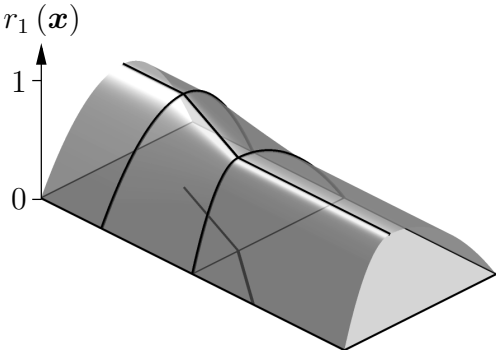

(b) $r_1(\boldsymbol{x})$.

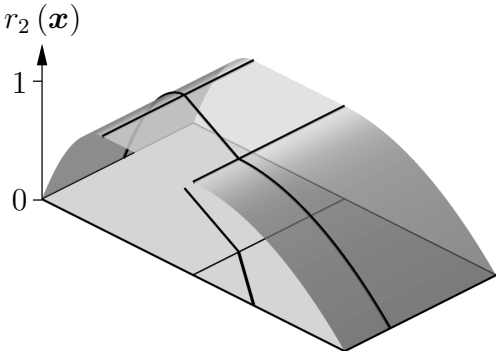

(c) $r_2(\boldsymbol{x})$.

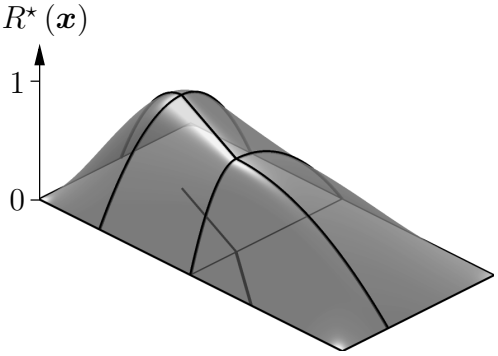

(d) $R^\star(\boldsymbol{x}) = r_1(\boldsymbol{x}) \cdot r_2(\boldsymbol{x})$.

Figure 5.16: Constructing an alternative ramp function $R^\star(\boldsymbol{x})$.

To test the accuracy of the proposed fading out function in terms of the SIFs, pure mode I displacement boundary conditions are applied onto the surface of a quadratic plate. As illustrated in figure 5.17(a), this plate contains a crack, with its tip ending in the center of the plate. In order to ensure that the proposed fading out functions yield sufficiently accurate results in terms of the SIFs also for varying orientations of mesh and crack, the crack is rotated in each computation by $\Delta\alpha = 0.04\,\pi$, as displayed figure 5.17(a). Here, the underlying finite element mesh, consisting of 39×39 quadratic shaped elements, remains fixed in all SIF computations. As only pure mode I displacement boundary conditions are applied, the ratio between the computed SIF K_{I} and its corresponding material parameter K_{Ic} should be equal to one, i.e. $K_{\text{I}}/K_{\text{Ic}} \stackrel{!}{=} 1$. The computed SIFs for both introduced ramp functions are displayed in figure 5.17(b): For rotations of $\alpha = \{1/4\,\pi,\ 3/4\,\pi,\ 5/4\,\pi,\ 7/4\,\pi\}$, with $k = 1, ...4$, the highest mismatch of SIFs for both fading out functions occurs, i.e. 1.1% using $R^\star(\boldsymbol{x})$ and 0.9% using $R(\boldsymbol{x})$. For cracks aligned with the finite element, i.e.

$\alpha = \{1/2\,\pi,\ \pi,\ 3/2\,\pi,\ 2\,\pi\}$, both simulations lead to more precise computations of the SIFs. Here, the qualitative behavior of both functions is similar, while a quantitative difference remains, as the nodal subset $\mathcal{J}^s$ contains more nodes using the enrichment scheme corresponding to the standard ramp function. This is consistent with observations made by LABORDE ET AL. (2005), comparing so-called "geometrical" with "topological" enrichment schemes.
As multiple crack tips in a single fine scale element are prohibited to maintain an accurate solution of the energy release rate, the introduced ramp function is not required on the fine scale. Therefore, $R^\star(\boldsymbol{x})$ and the corresponding enrichment scheme are only applied on the coarse scale.

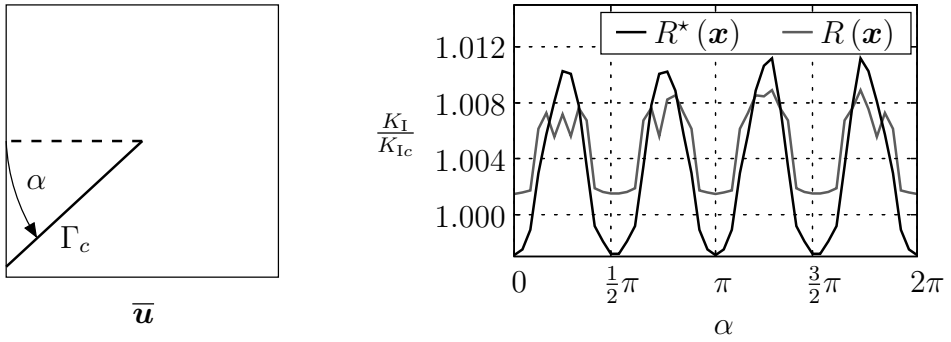

(a) Straight crack Γ_c, rotated with angle α.

(b) SIFs for both introduced ramp functions.

Figure 5.17: SIFs for pure mode I boundary conditions $\overline{\boldsymbol{u}}$, which are applied on the boundary of the domain.

A more detailed analysis of the introduced functions in terms of the position of the crack tip in the crack tip element was performed by HOLL ET AL. (2013). The authors found a maximum error in terms of the SIFs of 3% for both ramp functions, denoting that the alternative ramp function yields an accurate solution of the displacement field.

Coarse scale enrichment

Allowing any combination of two cracks in a finite element on the coarse scale yields a vast amount of different enrichment schemes. This extension becomes necessary for modeling crack coalescence within the proposed multiscale method. Before cracks merge on the fine scale both tips might lie within the same coarse scale element. Here, only the most important cases are demonstrated, even though all of them are considered in the finite element program. The following six examples cover all possibilities how a node might be enriched, illustrated in figures 5.18 - 5.23.
Figure 5.18 displays the enrichment scheme for two already merged cracks, occurring on the fine scale domain as well. As introduced in section 5.2.1, all nodes of the element (A) receive two HEAVISIDE enrichments, modifying their functions according to figure 5.7. In the neighboring element (B), the modified HEAVISIDE enrichment is applied as illustrated in figure 5.9, as both crack segments do not intersect in this element. Furthermore, elements

like element (C) exist, which are cracked once, but still have more than one HEAVISIDE enrichment per node as another crack is located in its neighboring element. Due to shifting the basis of the HEAVISIDE enrichment functions, only one set of enrichment functions is non-zero in element (C). Some elements which are not cracked might be enriched even with two enrichment functions, but the enrichment functions value is zero in these elements. Thus, element (D) receives additional DOFs, with the corresponding shape functions being zero, allowing a fast evaluation of those functions.
The enrichment scheme for two merging cracks, with a crack tip close to the intersection point is illustrated in figure 5.19. Due to the application of the modified ramp function and the appropriate enrichment scheme, all nodes of element (A) and (B) are enriched with the crack tip functions. Additionally, all nodes of element (B) are enriched with the introduced modified HEAVISIDE function (figure 5.7), to ensure a zero enrichment function above the intersection point. Thus, all enrichment functions in non-cracked elements are zero.
The consideration of two coarse scale crack tips in one coarse scale element is displayed in figure 5.20. Here, all nodes of element (A) receive two sets of crack front enrichment functions. Due to the curvature of both cracks and the modified ramp enrichment scheme, two nodes of element (A) additionally require HEAVISIDE enrichments. Thus, a node of this element has either $2\ (1+4+4) = 18$ DOFs for two crack tip enrichments or $2\ (1+4+4+1) = 20$ DOFs for two crack tips and a HEAVISIDE enrichment. Blending elements such as element (B) have the same unknowns as their neighbors, but the enrichment functions referring to the other crack tip vanish due to the modified ramp function. One node of element (C) still has 22 DOFs, but only HEAVISIDE enrichments referring to the discontinuity inside this element are non-zero.

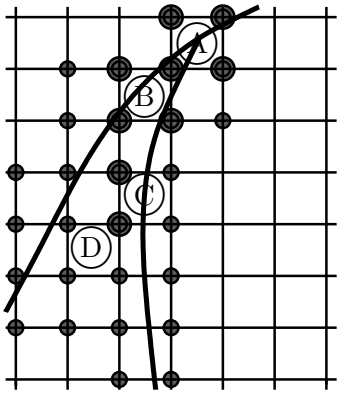

Figure 5.18: Intersecting cracks: Only HEAVISIDE enrichments.

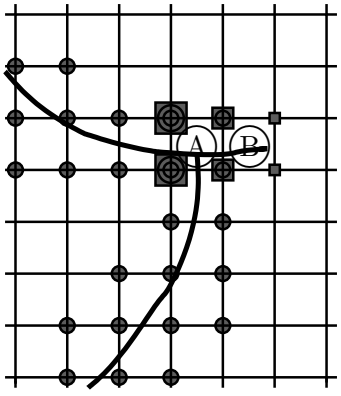

Figure 5.19: Intersecting cracks: HEAVISIDE and tip enrichments.

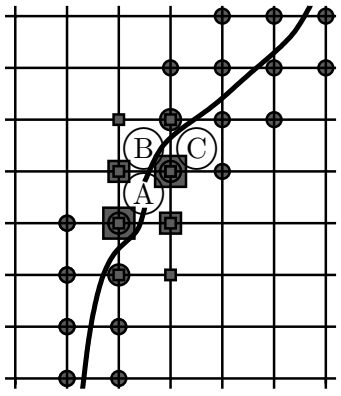

Figure 5.20: Two interacting crack tips.

The enrichment scheme for nearly merged cracks, e.g. one time step before the situation displayed in figure 5.18, is captured in figure 5.21. The nodes attached to element (A) and element (B) are enriched with the crack tip functions as well as with the HEAVISIDE function. The ramp function $R^0(\boldsymbol{x}) = R^\star(\boldsymbol{x})$ and the shifted HEAVISIDE enrichments yield zero enrichment functions in element (A) and zero crack tip enrichment in element (B). Thus, two non-zero enrichment functions occur in none of the displayed elements.

A similar case is considered in figure 5.22: Element (B) is not only a completely cracked element, but also a blending element referring to the upper crack tip. Thus, the nodes this element has in common with element (A) receive two sets of crack tip enrichments and one node is additionally HEAVISIDE enriched. This leads to $2\ (1+4+4) = 18$ DOFs for one node and $2\ (1+4+4+1) = 20$ DOFs for the other node. Note that no element receives two non-zero sets of enrichment functions as these functions are restricted to cracked elements.
The last presented crack configuration yields the highest number of unknowns per node considered in this work. Two nearly parallel cracks, with no element being twice cracked, lead to a rather complex enrichment scheme, as depicted in figure 5.23. The neighboring elements of element (A) which contain a crack are both blending elements. Thus, their node in common receives $2\ (1+4+4+1+1) = 22$ DOFs, which is the highest number of DOFs taken into account in this work. As none of the elements is cracked twice, none of them receive two sets of non-zero enrichment functions.

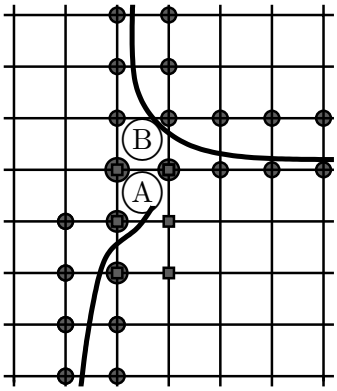

Figure 5.21: Crack tip interacting with crack face.

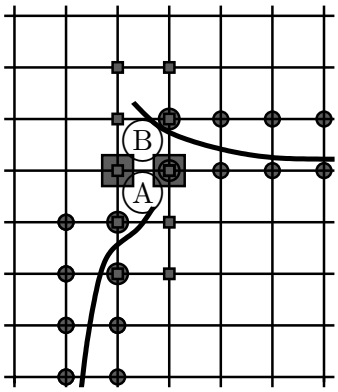

Figure 5.22: Just before intersection.

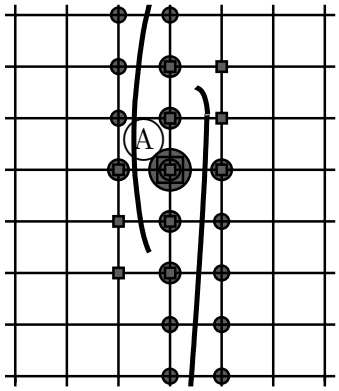

Figure 5.23: Highest number of DOFs.

From the above examples it can be seen that the shifted basis of the modified HEAVISIDE enrichment function and the modified ramp function $R^{\star}(\boldsymbol{x})$ yield easy evaluation of these functions, especially in non-cracked elements. Even though this short passage does not cover all possible crack configurations, it still demonstrates the great flexibility of the proposed method, without making any restrictions to the positions of two cracks in a finite element.

Crack coalescence

The crack coalescence scheme is now adopted within the introduced multiscale method which allows modeling multiple microcracks as well as macrocracks within one coarse scale element accurately. The criterion for crack coalescence, introduced in section 5.2.1, can be adopted one-to-one on the finest scale, such that the finest scale fully drives crack growth and crack coalescence. As the coarse scale crack is interpolated using coarse scale shape functions N^0, but the fine scale crack is interpolated using its respective shape functions N^1, the resulting coarse scale crack path needs to be mapped onto the coarse scale. Merging microcracks do not influence the coarse scale path, such that their coalescence can be

captured by the introduced singlescale approach. However, due to the size difference of the microcracks to the macrocracks, propagating microcracks are rare: In none of the examples investigated in section 5 does a single microcrack propagate. Thus, four different scenarios of merging cracks on two scales are considered and introduced here:

- Two macrocrack tips merge.
- A macrocrack tip merges with a macrocrack face.
- A macrocrack tip merges with a microcrack tip.
- A macrocrack tip merges with a microcrack face.

These cases are sketched in figures 5.24 - 5.27, with symbols used according to table 5.3. For the purpose of the overview the enrichment schemes are omitted here.
The consideration of two approaching macrocrack tips is displayed in figure 5.24: Once the enrichments on the fine scale overlap, the introduced criterion for coalescence is fulfilled. From the propagated crack tip, the shortest distance to the other crack tip is determined (figure 5.24(a)). Finally, the resulting path is mapped onto the coarse scale mesh, such that in each finite element the crack can be represented using one bilinear function (figure 5.24(b)). Therefore the intersection points of the first estimated crack path, displayed in figure 5.24(a), with the finite elements is determined. The level set interpolation of the resulting segmented crack yields C^0- continuous crack paths in Ω^0. Consequently, the final crack path slightly differs from its first estimation, but coarse scale mesh refinement overcomes this minor inaccuracy. Note that, coalescence is predicted later than in a comparable singlescale analysis. Thus, two approaching coarse scale crack tips can be modeled highly accurately using the multiscale approach, even with their tips being in the same/neighboring coarse scale element/s.

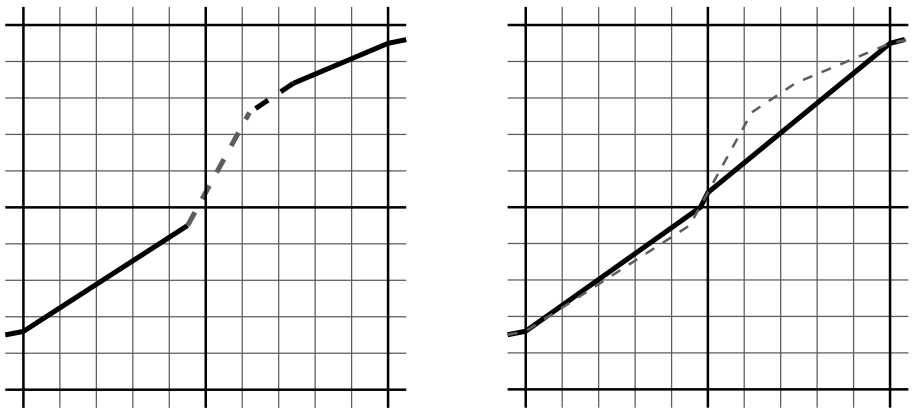

(a) One step before coalescence. (b) Final crack path.

Figure 5.24: Coalescing macrocrack tips.

The procedure for a macrocrack tip merging with a macrocrack face is similar to the approach introduced above: Once the enrichments overlap as illustrated in figure 5.25, the

shortest distance from the tip to the crack face is determined, yielding a first estimation of the resulting crack configuration. The C^0- continuous interpolation of the crack paths onto Ω^0 yields again a slightly different crack path. With mesh refinement, these differences vanish.

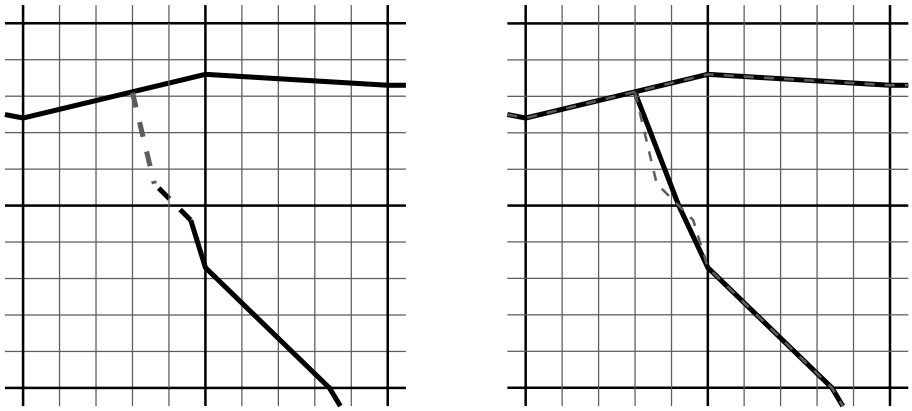

(a) One step before coalescence. (b) Final crack path.

Figure 5.25: Macrocrack tip and macrocrack face merge.

The coalescence of a microcrack tip with a macrocrack tip is similar to two merging macrocrack tips and illustrated in figure 5.26: Once the criterion for coalescence is fulfilled, both crack tips are connected via their shortest distance. In order to achieve a C^0- continuous crack path in Ω^0, the path is interpolated. Especially the former microcrack path differs from its coarse scale approximation, as it used to be interpolated with fine scale shape functions N^1. With this coalescence scheme a transition from fine scale features on the coarse scale is considered, as the microcrack is now part of the macrocrack.

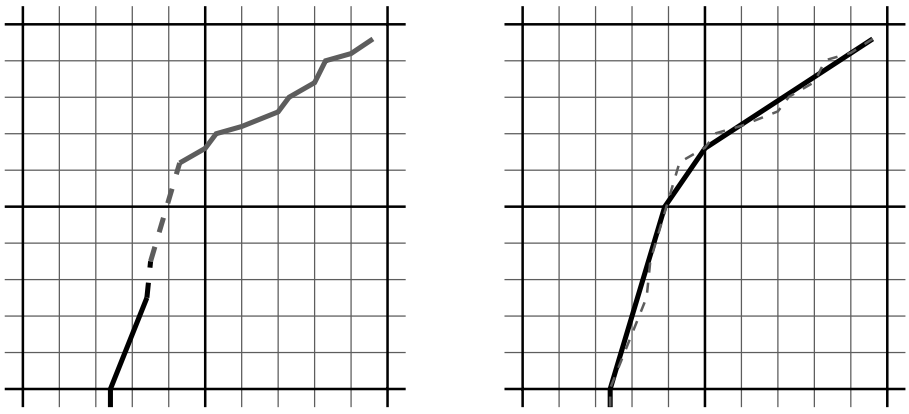

(a) One step before coalescence. (b) Final crack path.

Figure 5.26: Coalescing macrocrack tip and microcrack tip.

A difficulty arises if the shortest distance from a macrocrack tip to a microcrack does not yield a microcrack tip, but a microcrack face as displayed in figure 5.27(a). Merging both cracks at the determined point leads to the following problems: If this microcrack is only in

one coarse scale element, the coarse scale enrichment scheme is not longer valid. A ramp function being non-zero in this element would be required. In case coalescence occurs as displayed in figure 5.27(a), one of the resulting macrocrack tips might propagate. Using one bilinear function per element and crack to store their paths would naturally require moving their intersection point. To circumvent these issues and stick to two bilinear functions per element, a different approach is applied: Both microcrack tips are connected to the intersection point of the macrocrack with the finite element as displayed in figure 5.27(b). Thus, the introduced enrichment scheme and displacement field approximation can be applied independently of the position and length of microcracks and macrocracks. Depending on the geometry, i.e. fine and coarse scale mesh as well as microcracks and macrocracks, the final crack path differs from its first estimations. However, coarse scale mesh refinement reduces these differences automatically.

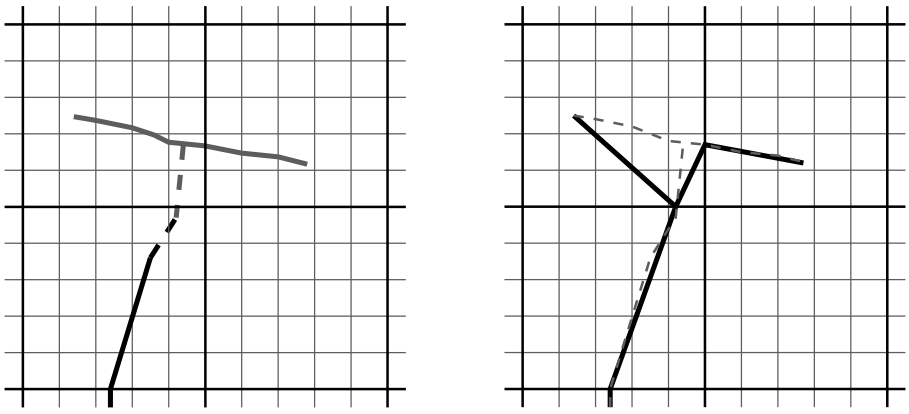

(a) One step before coalescence. (b) Final crack path.

Figure 5.27: Macrocrack tip merges with microcrack face.

Independent of the coalescence scenario, the enrichment scheme is finally updated, such that the enrichment functions match the new crack geometry.

Overall numerical procedure

The extensions introduced in this section yield the components for a multiscale framework to capture crack growth and crack coalescence of cracks on different length scales. The computational framework is sketched in table 5.5. As fine scale domains are chosen to be within an user defined radius around the macrocrack crack tips, whose position might change due to crack propagation, this method is fully adaptive. Furthermore, the fine scale domains are allowed to grow together, yielding a flexible tool to determine crack growth and crack coalescence efficiently and accurately.

loop, number of propagation steps n_{prop}	
solve for displacement field	section 4.3
update boundary conditions λ^0	section 5.1.2
solve for displacement field	section 4.3
perform crack propagation	section 5.1.2
check for and perform crack coalescence	section 5.2.2
end loop	
solve for displacement field	section 4.3
update boundary conditions	section 5.1.2
solve for displacement field	section 4.3

Table 5.5: Overall numerical procedure to perform multiscale crack propagation and crack coalescence.

Computational examples

In the last part of this section, three computational examples reveal the need to take microcracks into account. Furthermore, they demonstrate the robustness and flexibility of the proposed model. The required number of finite elements to take microcracks into account in a singlescale analysis, explains the need for a multiscale analysis. The last two presented examples are published by HOLL ET AL. (2013).

Three-point bending test

The three-point bending test by INGRAFFEA & GRIGORIU (1990), introduced in section 5.1.1, is investigated by taking 199 randomly distributed microcracks of length $0.15a$ into account. The initial crack distribution is displayed in figure 5.28, while the material and geometrical properties are kept, according to figure 5.3. In contrast to the singlescale analysis, the coarse scale mesh consists of 682 coarse scale elements, while each coarse scale element is refined with 9×9 fine scale elements. Thus, the coarse scale problem is reduced by a factor of 10, while the effective mesh resolution is about 5 times higher than in the singlescale analysis.
The final crack path is displayed in figure 5.28: In the first propagation steps, the trajectory shows a similar behavior to the experimental solution. As the crack tip gets attracted by a microcrack, the angle of deflection is slightly larger. Once both cracks merge, the path changes, such that the trajectory of the multiscale simulation is nearly parallel to the experimentally determined crack path. Once the macrocrack reaches another microcrack, crack coalescence, and with it a second major kink in the path, occurs. Finally, the crack tip intersects the boundary of the middle hole at a different point than observed in the experiment.
This example clarifies two major aspects of the proposed method: Firstly, existing microcracks cannot be neglected as they might change the final crack path. Secondly, the required computational effort can be reduced drastically by the multiscale approach: A refinement to capture the fine scale effects with uniform refinement accurately yields five times more elements.

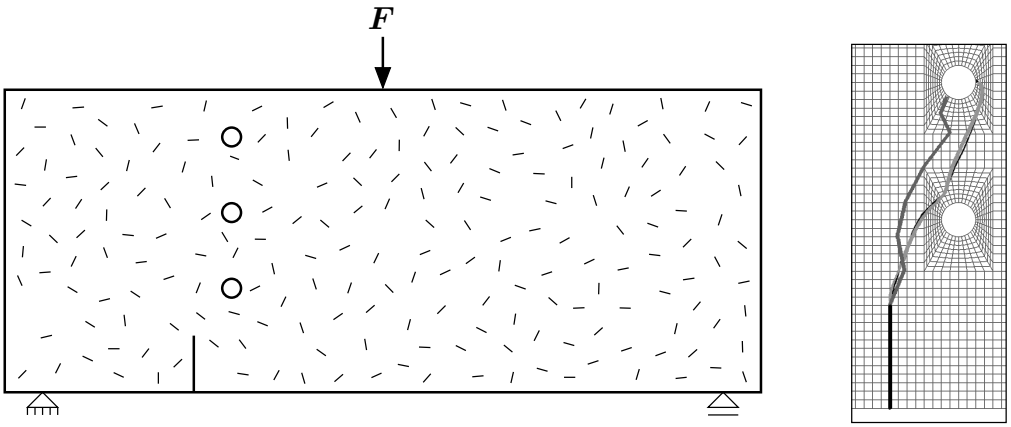

Figure 5.28: Left: 199 randomly distributed microcracks of length $0.15a$ in experiment by INGRAFFEA & GRIGORIU (1990) with measurements given in figure 5.3.
Right: Experimental crack path (black), numerical crack path without microcracks (light gray) and numerical macrocrack path including microcracks (dark gray).

Multiscale analysis versus singlescale analysis

In the second example, a square domain Ω^0 with its origin in its center and of size $\ell \times \ell$, with $\ell = 2.0$, is investigated taking into account about 150 randomly distributed microcracks of length $0.005\,\ell$. To identify the required finite element mesh and to study the robustness of the presented method, results of coarse scale mesh refinement are discussed. Secondly, the multiscale method is compared to a singlescale analysis without considering microcracks.

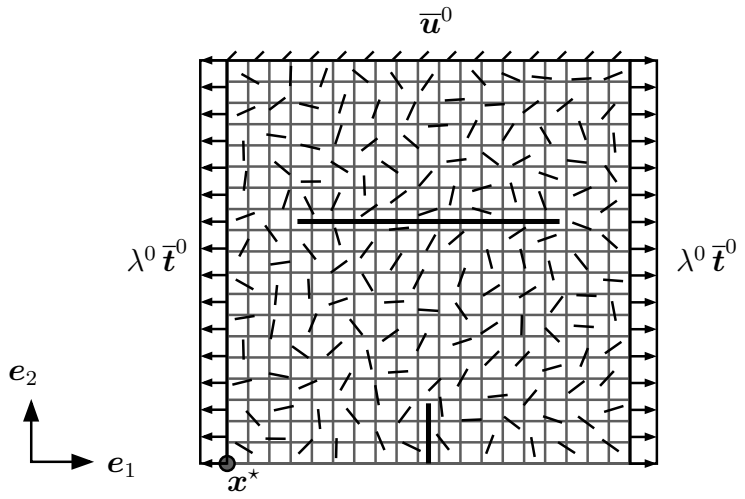

Figure 5.29: About 150 microcracks and two macrocracks in Ω^0, here meshed with 19×19 coarse scale elements.

Here, quasi-static crack propagation in an isotropic, linear elastic solid with the LAMÉ's material constants $\mu = 10$, $\Lambda = 20$ and the energetic fracture toughness $J_c = 1$ is assumed. As displayed in figure 5.29, uniform tractions $\overline{\boldsymbol{t}}^0 = \pm\,\boldsymbol{e}_1$ are applied on the left and right side of the square. The structure is clamped at the upper side of Ω^0, i.e. $\overline{\boldsymbol{u}}^0 = \boldsymbol{0}$. The fine scale

domains are chosen to be within the user defined radius $r_{\mathrm{MS}} = 0.21\,\ell$ around the macrocrack tips.
To capture all microcracks precisely in a singlescale analysis requires a 241×241 uniform finite element mesh. The effective mesh, i.e. fine scale elements per coarse scale element times the number of coarse scale elements, for multiscale analysis should have at least the same resolution. As the final crack path is interpolated using N^0 shape functions, it depends mainly on the coarse scale mesh resolution. Thus, the coarse scale mesh is refined, while the number of fine scale elements per coarse scale element is decreased to obtain a similarly effective mesh resolution. Here, the introduced problem is computed using five different meshes, according to table 5.6.

Refinement	Coarse scale elements	Fine scale elements per coarse scale element	Resulting mesh considering uniform refinement
1	19×19	13×13	247×247
2	29×29	9×9	261×261
3	39×39	7×7	273×273
4	49×49	5×5	245×245
5	89×89	3×3	267×267

Table 5.6: Mesh resolution properties.

Three resulting coarse scale meshes of the crack tip belonging to the vertical crack are illustrated in figure 5.30. Independent of the coarse scale resolution, the fine scale elements have about the same size. Furthermore, the area and shape of the fine scale domain changes as coarse scale elements inside or cut by the circle spanned with r_{MS} around the crack tip, belong to Ω^1. A fine mesh in Ω^0 approximates the circular fine scale domain more precisely, yielding slightly different fine scale domains for the introduced coarse scale meshes.

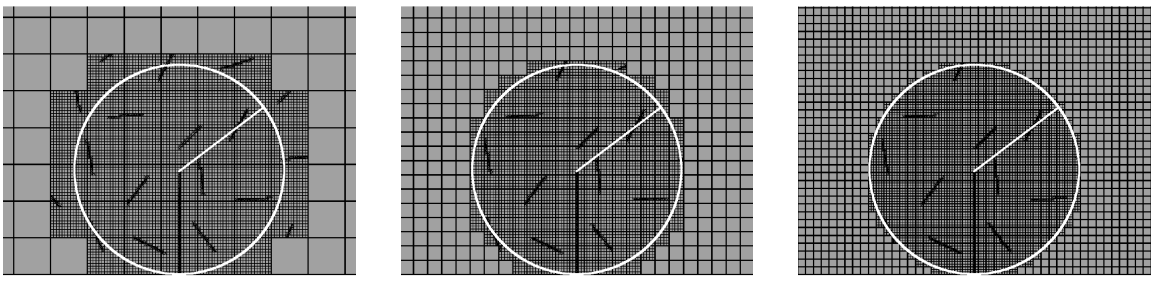

(a) 19×19 coarse scale elements; 13×13 fine scale elements per coarse scale element.

(b) 49×49 coarse scale elements; 5×5 fine scale elements per coarse scale element.

(c) 89×89 coarse scale elements; 3×3 fine scale elements per coarse scale element.

Figure 5.30: Coarse scale mesh refinement. Radius r_{MS} is marked white.

The resulting crack paths for the introduced multiscale meshes are displayed in figure 5.31 (left). All crack paths resemble each other: The propagating macrocrack tips initially grow in the same direction and merge with the same microcracks. In all examples, the macrocrack tip hits the second macrocrack face at nearly the same point. Due to the bilinear

interpolation of the macrocracks on the coarse scale, the final crack paths vary slightly from each other. Thus, the finer coarse scale discretizations naturally exhibit a smoother description of the final crack path. However, the coarsest mesh still captures the crack path with sufficient accuracy.
A comparison of the required load to satisfy crack growth, i.e. $\max(\mathcal{G}) = \mathcal{G}_c$, is illustrated in figure 5.31 (right): The starting time t_0 refers to the initial configuration displayed in figure 5.29 while the final time T is the time when both macrocracks merge. Crack coalescence leads to an abrupt extension of the crack path on the coarse scale. Adapting the load factor yields kinks in the displayed diagrams, which all computations reflect in a similar fashion. Apart from the coarsest mesh, the major kink, occurring at about two-thirds of the computation time, has a similar peak value. Thus, the comparison of the load displacement curves exhibits similar features as comparing the crack paths: All investigated meshes provide similar results for this complex example, such that the proposed method is assumed to be robust.

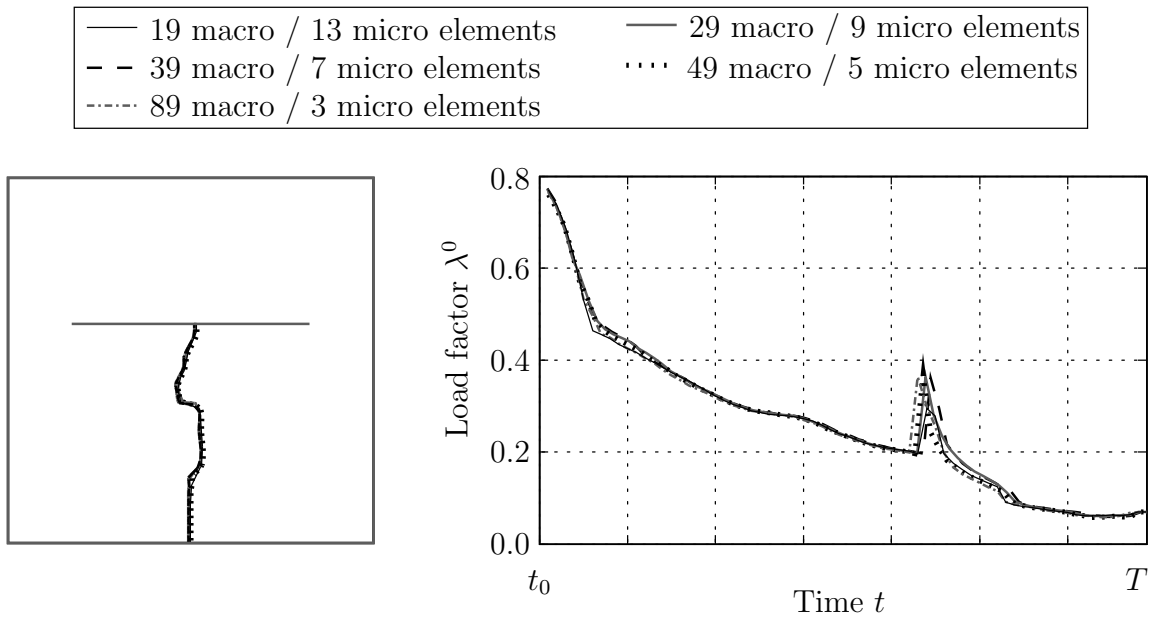

Figure 5.31: Final crack paths in Ω^0 and load factor versus displacement for different coarse scale meshes.

To study the effect of microcracks, the example sketched in figure 5.29 is computed in a singlescale analysis without taking any microcracks into account. The dependency of the load factor on the load step is illustrated in figure 5.32(a). As the crack tip in the singlescale analysis runs straight through the domain and merges only with the second macrocrack, the crack paths vary. Consequently, the position of the crack tips differ at the same load step such that a direct comparison of both analyses is difficult. As the crack tip positions in the initial configuration and just after the coalescence of both macrocracks are the same, the singlescale result is stretched to match these points. Two major differences between both curves stand out in this example: Firstly, taking microcracks into account yields a higher external load to enforce crack propagation, meaning that microcracks are a positive feature to prevent the

macrocrack from growing. Secondly, the load curve decreases smoothly without any kinks in the singlescale computation, while the consideration of microcracks leads to significant kinks which occur when cracks merge.
In figure 5.32(b) load-displacement curves are given, evaluated at point $\boldsymbol{x}^\star$ which is marked in figure 5.29. Apart from the initially varying load factors another major difference can be observed: The initial tangents have different slopes due to the fact that microcracks globally weaken the structure. Furthermore, this figure displays once more the robustness of the proposed method: Due to the application of load control procedure with the crack propagation criterion being the constrained equation, such a complex load-displacement curve, i.e. snap-back problem, can be computed both with comparable ease and speed. Here, the sharp peaks and many kinks do not cause any difficulties in solving the system of equations.

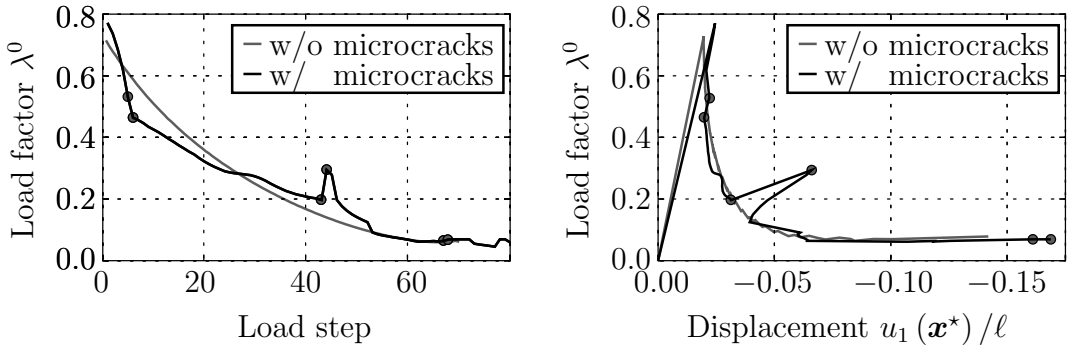

(a) Load factor versus load step.

(b) Load factor λ^0 versus displacement at point $\boldsymbol{x}^\star = -\boldsymbol{e}_1 - \boldsymbol{e}_2$.

Figure 5.32: Comparing singlescale analysis without microcracks to coarsest multiscale analysis.

In the following figures 5.33 - 5.36, the coarse scale domain $\Omega^0 \backslash \Omega^1$ is displayed with its finite element meshes, while the fine scale meshes are omitted to maintain visibility, i.e. fine scale domains are displayed as surface plots. The gray circled marks in figure 5.32 refer to crack configurations in figures 5.34 - 5.36 always one step before and one step after crack coalescence.
A reason for requiring a higher external load once the microcracks are considered is displayed in figure 5.33: In the vicinity of the macrocrack tip, a nearly parallel running microcrack shields the macrocrack tip. The stresses and therefore the SIFs are reduced such that a higher external load is required to perform crack propagation. Further numerical investigations on crack shielding were performed by LOEHNERT & BELYTSCHKO (2007a).
Once the advancing macrocrack has passed the shielded area, the corresponding tip reaches a microcrack tip, displayed in figure 5.34(a). A further crack propagation step fulfills the criterion of crack coalescence, such that the crack tips of both cracks are connected. According to section 5.2.2, the resulting macrocrack is mapped onto the coarse scale, yielding the configuration displayed in figure 5.34(b).

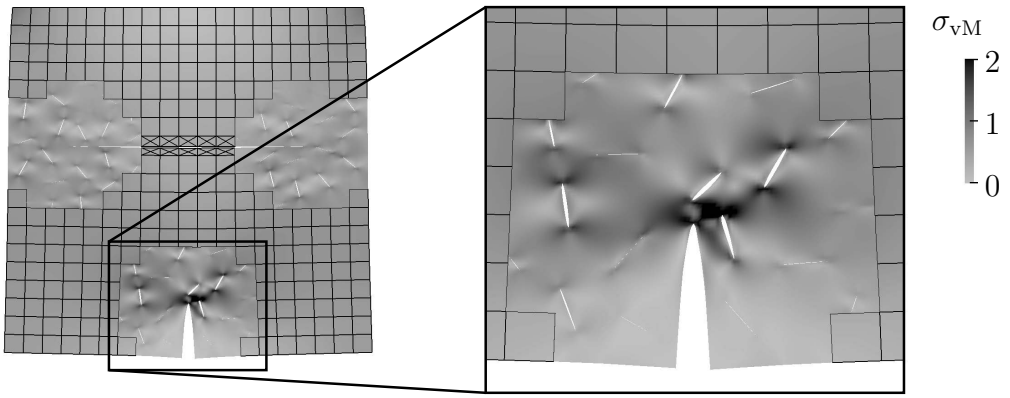

Figure 5.33: Crack shielding in first load step.

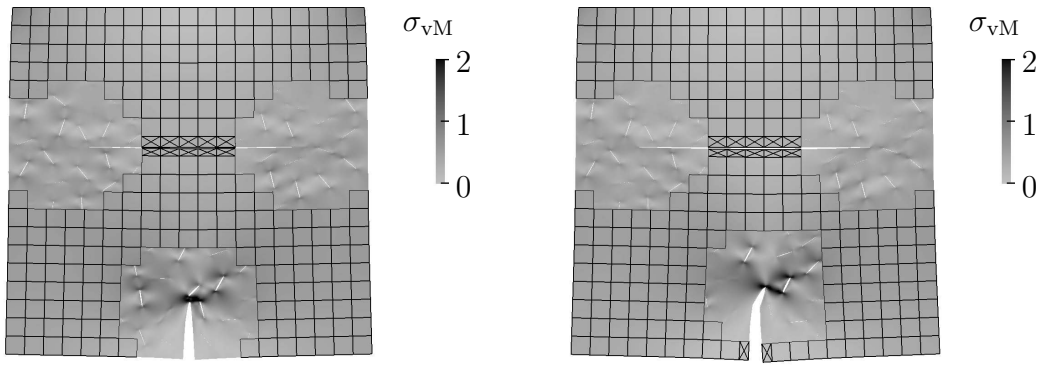

(a) VON MISES stress σ_{vM} before coalescence. (b) VON MISES stress σ_{vM} after coalescence.

Figure 5.34: Microcrack elongates macrocrack abruptly.

Due to the loading conditions, the macrocrack and with it the corresponding fine scale domain, is moving upwards until the macrocrack tip reaches another microcrack tip, displayed in figure 5.35(a). In the following load step both crack tips merge, displayed in figure 5.35(b). Due to the orientation of the microcrack, the resulting macrocrack is abruptly tilted approximately $\pi/2$. However, the applied boundary conditions force the crack to grow in $\boldsymbol{e}_2$-direction, which requires an increase of λ^0 compared to the previous load step. After the following propagation step, the crack already has nearly rotated back in its original direction, such that the load is decreased. Thus, this microcrack is responsible for the kinks in the load-displacement and the load-time curves, displayed in figure 5.32. Note that, only in two computation steps do the fine scale domains overlap. Thus, the projection of the boundary conditions as well as solving the fine scale domains are mainly computed independent of each other.

After merging with two other microcracks, the propagating macrocrack tip reaches the other macrocrack face. As displayed in figure 5.36(a), all fine scale domains overlap, such that only one large fine scale domain exists. An infinitesimal increase of the external load yields crack propagation of the vertically running macrocrack, such that the nodal enrichments on the fine scale overlap and both macrocracks merge. As the propagating crack tip merges with

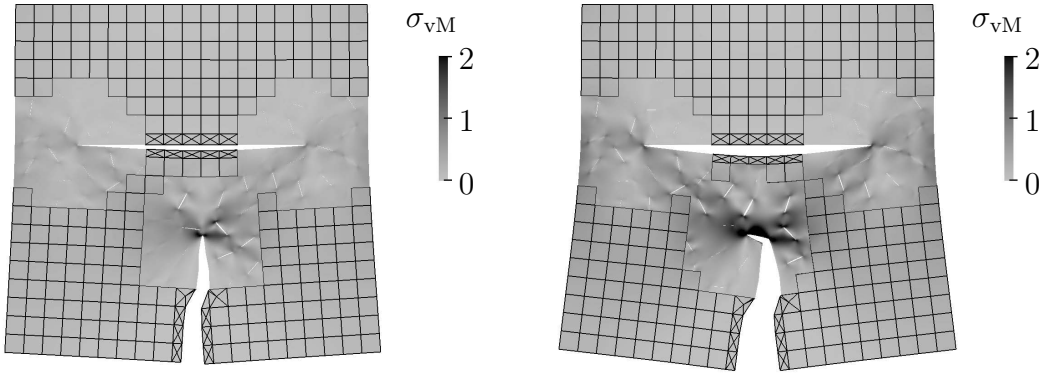

(a) VON MISES stress σ_{vM} before coalescence. (b) VON MISES stress σ_{vM} after coalescence.

Figure 5.35: Crack coalescence leads to a highly different macrocrack tip orientation.

a macrocrack face, the crack tip vanishes and is consequently enriched using two modified HEAVISIDE enrichment functions. Defining fine scale domains only in the vicinity of macrocrack tips, only two non-overlapping fine scale domains remain, displayed in figure 5.36(b). As none of the two macrocrack tips are shielded or amplified by microcracks, the SIFs and the load factor λ^0 reach a similar value as in the singlescale analysis.

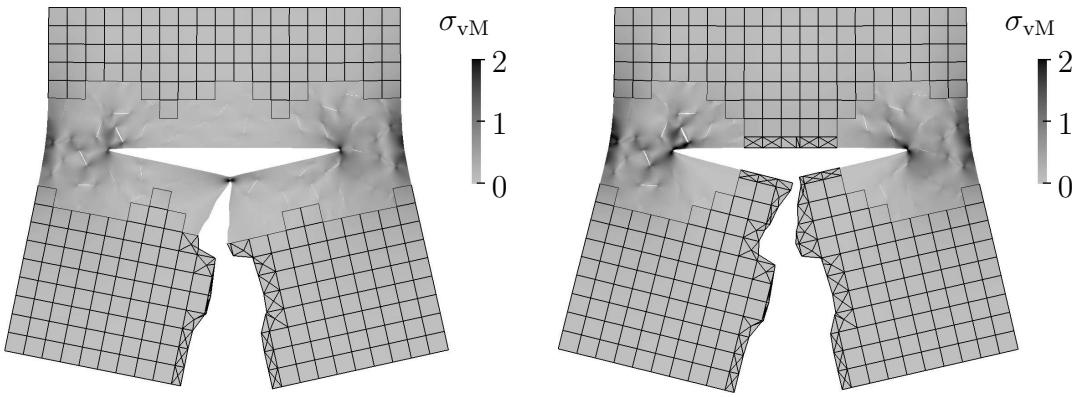

(a) VON MISES stress σ_{vM} before coalescence. (b) VON MISES stress σ_{vM} after coalescence.

Figure 5.36: Both macrocracks merge.

This example exhibits the great impact microcracks have on the global response of the structure. Not only do the crack paths change when microcracks are considered, but also the required external load differ due to shielding and amplification of microcracks. Furthermore, a refinement of the finite element mesh shows the robustness of the proposed method.

Effect of a single microcrack

In the following example, the influence of a single microcrack on the overall behavior of the structure is investigated. The material parameters $\mu, \Lambda, \mathcal{G}_c$ and the size of Ω^0 are adopted from the previous example. Only the length of the about 110 microcracks, i.e. $0.0056\,\ell$, as

well as the size of the fine scale domains, with $r_{\mathrm{MS}} = 0.19\,\ell$, are changed slightly to demonstrate that fine scale domains can separate during the computation process. The structure contains four macrocracks with seven tips, whose fine scale domains initially all overlap. To study the influence of a single microcrack, the structure is computed including the centered microcrack, displayed in figure 5.37(a), and omitting this microcrack as illustrated in figure 5.37(b). Therefore, the samples will be referred to as "with microcrack" and "without microcrack" respectively. Both structures undergo the same boundary conditions: They are clamped at the bottom, i.e. $\overline{\boldsymbol{u}}^0 = \boldsymbol{0}$, and are torn apart at their top with $\overline{\boldsymbol{t}}^0 = \boldsymbol{e}_2$. As in the previous example, fine scale domains are displayed as surfaces while the contour of the finite elements is displayed in the course scale domain $\Omega^0 \backslash \Omega^1$.

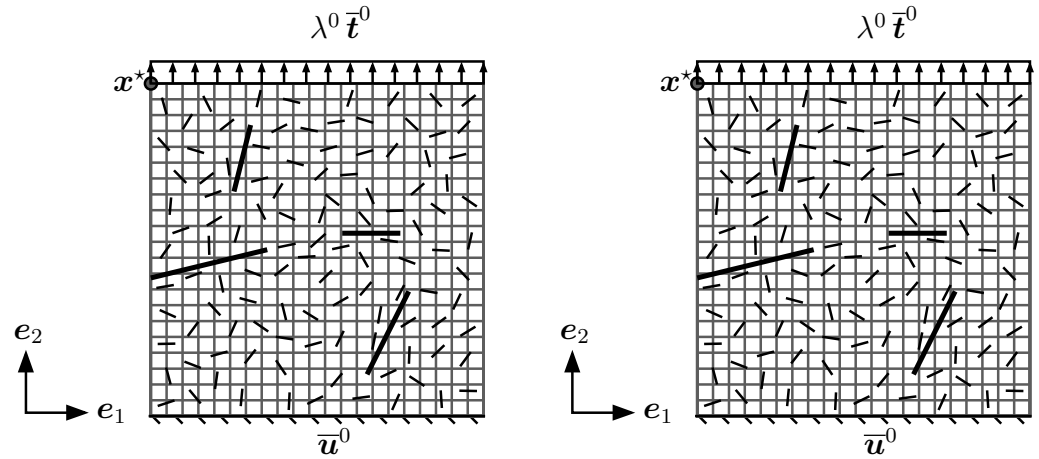

(a) Crack distribution with a microcrack in the center of Ω^0.

(b) Crack distribution without a microcrack in the center of Ω^0.

Figure 5.37: Domain Ω^0 with four macrocracks and about 110 microcracks, meshed with 21×21 coarse scale elements. Each coarse scale element is split into 9×9 fine scale elements.

Loading the structure "with microcrack" yields the highest energy release rate at the macrocrack tip, which is cutting the boundary of Ω^0. After merging with two microcrack tips, displayed in figures 5.38(a) - (b) and in figures 5.38(b) - (c), two macrocrack tips merge, illustrated in figures 5.38(c) - (d). Subsequently, the fine scale domains do not overlap anymore resulting in two smaller fine scale domains. With further crack propagation, the advancing macrocrack reaches a microcrack face, displayed in figure 5.38(d). Merging both cracks, as shown in figure 5.38(e), yields an additional macrocrack tip and consequently an extra fine scale domain. As it still overlaps with other fine scale domains, the total number of fine scale domains does not change. No further crack coalescence occurs until the end of the computation, captured in figure 5.38(f).
At the beginning of the fracturing process, the second structure "without microcrack" behaves similarly to the previous example: After some propagation steps of the same macrocrack tip, a microcrack elongates the advancing macrocrack, displayed in figures 5.40(a) - (b). Due to the omission of the centered microcrack, the macrocrack propagates in contrast to the previous example more in negative $\boldsymbol{e}_2$-direction, illustrated in figure 5.40(c). After merging

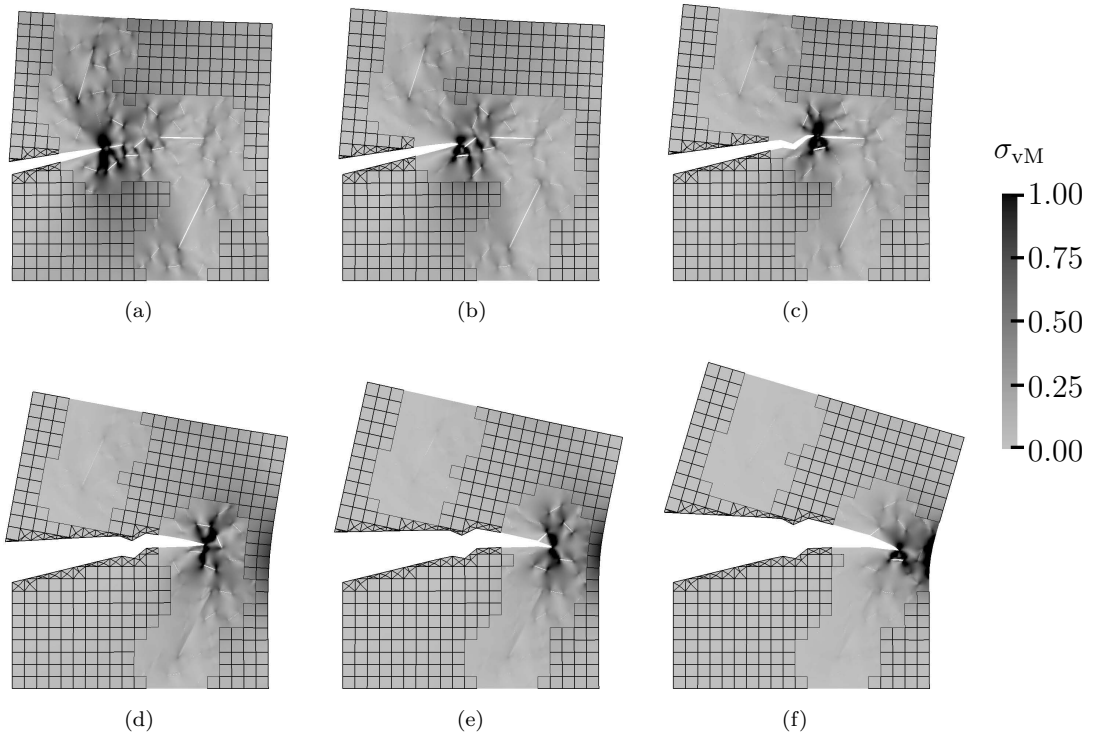

Figure 5.38: Crack propagation and coalescence for sample "with microcrack" referring to figure 5.37(a).

with a microcrack, displayed in figure 5.40(d), the macrocrack merges with a macrocrack face, shown in figure 5.40(e). Thus, only one crack tip vanishes, such that one fine scale domain vanishes. However, the fine scale domains do not overlap anymore, such that two smaller fine scale domains are computed onwards. The propagating tip merges analogously to the previous example with a microcrack face, generating an additional macrocrack tip, before reaching its final position at the end of the computation, displayed in figure 5.40(f).
Comparing both final crack paths in figure 5.39(a) reveals the impact of a single microcrack on the global behavior: While the crack paths are similar in the beginning of the computation, their deviation in the center of the plate is large. Once the tips merge with the centered macrocrack, the crack trajectories resemble each other.
A similar conclusion can be drawn by investigating the load-displacement behavior of both computations, displayed in figure 5.39(b). The initial tangents are similar, but once crack propagation occurs, totally different responses of the structure are observed: For $0.15 > u_2\left(\boldsymbol{x}^\star\right)/\ell > 0.05$ both samples follow complex load-curves with some snap-backs, until the macrocracks merge. From that point on, the load-displacement curves resemble each other, both undergoing two minor snap-backs in a very similar fashion.
This example reveals the effect of a single microcrack on the global response of the structure: In this example, omitting one microcrack yields a totally different post critical behavior in terms of load-displacement curves and crack paths. Thus, it shows once more the need of taking all microcracks into account, even though the global response is similar once both

macrocracks are merged: A single microcrack might change the behavior of the structure significantly and with it the required external load λ^0 to perform crack propagation.

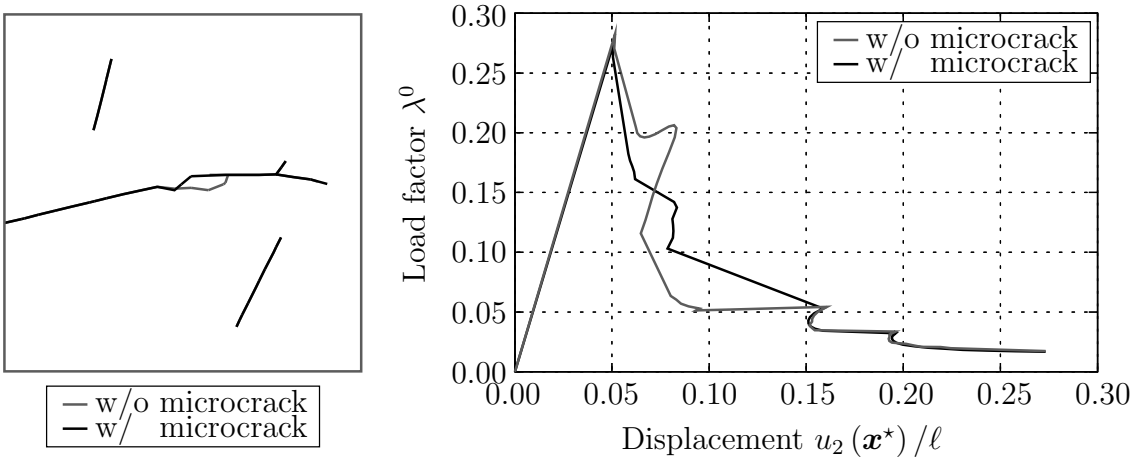

(a) Final crack paths in Ω^0.

(b) Load factor versus displacement at point $\boldsymbol{x}^\star = -\boldsymbol{e}_1 + \boldsymbol{e}_2$.

Figure 5.39: Crack paths and load-displacement curves.

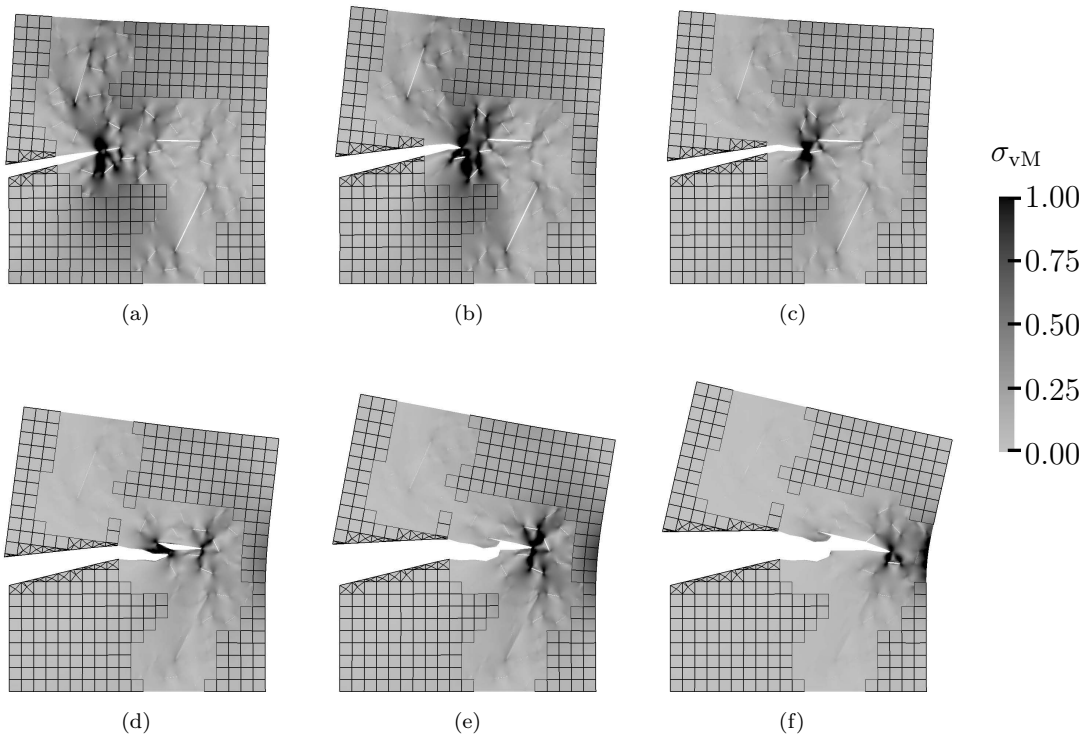

Figure 5.40: Crack propagation and coalescence for sample ”without microcrack“ referring to figure 5.37(b).

5.3 3D crack propagation

As the XFEM combined with the multiscale projection method revealed its benefits for two-dimensional problems, it is extended to three-dimensional space in this section. The implemented crack propagation algorithm is first presented for singlescale analysis in section 5.3.1 and finally utilized in a multiscale framework in section 5.3.2.

5.3.1 Crack propagation on one scale

Analyzing cracks in three-dimensional space using the XFEM/GFEM goes back to the work of DUARTE ET AL. (2000), SUKUMAR ET AL. (2000) and LOEHNERT ET AL. (2011) in terms of the corrected XFEM, among others. Crack propagation in context of LEFM was successfully employed by DUARTE ET AL. (2001), MOËS ET AL. (2002), GRAVOUIL ET AL. (2002), CHOPP & SUKUMAR (2003), SUKUMAR ET AL. (2003) and FRIES & BAYDOUN (2012) among others. Two major tasks are discussed in most above mentioned publications: Firstly, a criterion of crack propagation and secondly a method to update the crack surface Γ and crack front $\partial\Gamma$. Both issues are addressed in this section and finally applied to three-dimensional crack propagation problems.

Stress intensity factor extraction

Extending the J-integral to three-dimensional problems is not straight forward, as the crack front does not enclose a ring on which the integral has to be carried out as in two-dimensional problems. The mathematical extension from a two-dimensional ring to a three-dimensional tube, as proposed by MORAN & SHIH (1987a) and MORAN & SHIH (1987b), displayed in figure 5.41, yields SIFs depending on the position of their evaluation, i.e. $K_{\mathrm{I}} = K_{\mathrm{I}}(\boldsymbol{x}_{\partial\Gamma})$, $K_{\mathrm{II}} = K_{\mathrm{II}}(\boldsymbol{x}_{\partial\Gamma})$, $K_{\mathrm{III}} = K_{\mathrm{III}}(\boldsymbol{x}_{\partial\Gamma})$, with $\boldsymbol{x}_{\partial\Gamma} \in \partial\Gamma$. Thus, the J-integral, whose value depends on its position s on the crack front, yields a similar computation as in (2.74). In order to apply a domain form as done for two-dimensional problems, a smoothing function being zero outside the integrated domain V is applied. In terms of the XFEM, this approach was implemented by SUKUMAR ET AL. (2000) leading to an adequate approximation for the SIFs, which is thus applied in this work.

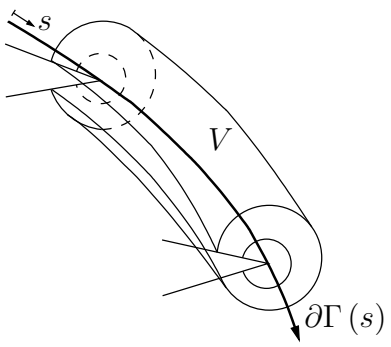

Figure 5.41: Volume V to integrate for SIF extraction along crack front $\partial\Gamma(s)$, with $s = s(\boldsymbol{x}_{\partial\Gamma}), \boldsymbol{x}_{\partial\Gamma} \in \partial\Gamma$.

As the energy release depends on the position along the crack front one might consider two strategies to model crack propagation: In cases where crack propagation occurs, only points which fulfill the criterion for crack propagation advance. This might yield a rather rough crack front $\partial\Gamma$ and a lot of iterations to follow the crack path. Alternatively, one can consider the whole crack advancing in cases where crack propagation occurs at one point, yielding most likely a comparably smooth crack front. The parts of the crack front of the advancing crack which do not fulfill the criterion of crack growth, propagate according to their energy release. FRIES & BAYDOUN (2012) state that in LEFM the final crack path does not depend on one of the approaches. As the second idea yields faster results it is applied in this work. Rewriting the criterion for crack propagation (2.68) in terms of the relative energy release rate $\tilde{\mathcal{G}} = \tilde{\mathcal{G}}(\boldsymbol{x}_{\partial\Gamma})$ yields

$$\exists\, \boldsymbol{x} \in \partial\Gamma : \tilde{\mathcal{G}}(\boldsymbol{x}) = \frac{\mathcal{G}(\boldsymbol{x})}{\mathcal{G}_c} \geq 1 \quad . \tag{5.16}$$

As in linear elastic quasi-static fracture mechanics the increment of propagation is unknown, this amplitude of growth $\Delta a = \Delta a(\boldsymbol{x}_{\partial\Gamma})$ is chosen to depend on the energy release rate. Thus, points of propagating cracks not fulfilling (5.16), according to the above mentioned second propagation approximation, advance as well, such that

$$\Delta a = k\,\tilde{\mathcal{G}} \quad . \tag{5.17}$$

Here, k is typically chosen to be half a characteristic element length as chosen for two-dimensional problems, i.e. $k = h_e/2$. Applying the same strategy as proposed for two-dimensional problems to ensure stable crack growth, the boundary conditions are multiplied with a global load factor λ. Thus, crack propagation is just occurring in the following load step such that the highest amplitude of growth is equal to k.
Making the rigorous assumption of pure mode I/II propagation allows the application of the criterion of maximum hoop stress (2.88) to determine the direction of growth $\theta_c = \theta_c(\boldsymbol{x}_{\partial\Gamma})$. Thus, the position of the new crack front $\boldsymbol{x}_{\partial\Gamma_{(i+1)}}$ for the following load step $(i+1)$ can be determined by adding the increment of growth $\boldsymbol{v} = \boldsymbol{v}\left(\boldsymbol{x}_{\partial\Gamma_{(i)}}\right)$ to the current position of the crack front $\boldsymbol{x}_{\partial\Gamma_{(i)}}$

$$\begin{aligned} \boldsymbol{x}_{\partial\Gamma_{(i+1)}} &= \boldsymbol{x}_{\partial\Gamma_{(i)}} + \boldsymbol{v} \\ &= \boldsymbol{x}_{\partial\Gamma_{(i)}} + \Delta a\, \cos(\theta_c)\, \boldsymbol{g}_1 + \Delta a\, \sin(\theta_c)\, \boldsymbol{g}_2 \quad . \end{aligned} \tag{5.18}$$

Here, the orthogonal local basis $\boldsymbol{g}_i$ at the crack front, displayed in figure 2.4, can be computed easily using the level set fields ψ and ϕ

$$\boldsymbol{g}_1 = \frac{\nabla\phi}{||\nabla\phi||} \quad , \quad \boldsymbol{g}_2 = \frac{\nabla\psi}{||\nabla\psi||} \quad , \quad \boldsymbol{g}_3 = \boldsymbol{g}_1 \times \boldsymbol{g}_2 \quad . \tag{5.19}$$

As pointed out by FRIES & BAYDOUN (2012) and by RABCZUK ET AL. (2010), the evaluation of the SIFs might pose some difficulties. To overcome this issue, MOUSAVI & SUKUMAR (2010) and MINNEBO (2012) investigated the impact of the transformation by DUFFY (1982) on the accuracy of the SIFs. Therefore, the integration introduced in section 3.1.3 should be modified: To capture the stress singularity more accurately, the tetrahedrons/triangles introduced for integration should be collapsed at the crack front/tip. A

different strategy to improve the SIF extraction was proposed by OZER ET AL. (2012): The authors apply higher order LEGENDRE polynomials for the arbitrary smoothing function q leading to a better approximation of the SIFs. A third alternative to improve accuracy is the application of higher order terms of the asymptotic solution by WILLIAMS (1957) and MUSKHELISHVILI (1963), implemented in the XFEM framework by LIU ET AL. (2004), RÉTHORÉ ET AL. (2010), PASSIEUX ET AL. (2011), ZAMANI ET AL. (2012) and LAN ET AL. (2013). Besides the better approximation of the displacement field at the crack front and a direct evaluation of the SIFs, this method yields more unknowns, depending on the applied order of displacement approximation. Even though those approaches have a benefit towards the extraction of the SIFs, the proposed method still yields adequate results and will be applied in the following.
As the SIFs and therefore θ_c and Δa vary depending on their position, these variables require discretization as well. Thus, the SIFs are evaluated in the center of the elementwise trilinear segment of the crack front, and then linearly interpolated onto intersection points of the finite element with the crack segment, taking into account the values of the neighboring elements. This leads to N_{fp}^{j} discrete points $\hat{\boldsymbol{X}}_i$ describing the crack front for each propagating crack j. As within this approach the level set values are interpolated using C^0- continuous functions, their gradient in (5.19) is generally discontinuous on the boundary of the finite element. Thus, the local basis at the intersection points is averaged by the arithmetic mean leading to the crack front movement $\boldsymbol{v}_i = \boldsymbol{v}\left(\hat{\boldsymbol{X}}_i\right)$ for each discrete point $\hat{\boldsymbol{X}}_i$.

Crack propagation due to damage growth

Besides difficulties the J-integral might pose in three-dimensional space that are discussed above, it is even more difficult to evaluate this quantity for non-linear material behavior. However, the introduced damage model overcomes both issues: With an appropriate choice of $\tilde{\epsilon}$, a criterion for crack growth for a variety of different material laws is available without even requiring the computation of J. Thus, the C^0- continuous distribution of $\overline{\epsilon}$ yields a damage based criterion for crack growth (2.100). Similar to the energy release based criterion, a crack advances once one point on the crack front fulfills (2.100) such that the increment of growth can be computed similar to (5.17)

$$\Delta a = k\,\frac{\overline{\epsilon}\left(\boldsymbol{x}_{\partial\Gamma}\right)}{\kappa_c} \quad . \tag{5.20}$$

Employing the criterion of maximum hoop stress following the technique by FRIES & BAYDOUN (2012) yields analogously to the SIF extraction the direction of growth θ_c. This direction is found by searching along an arc around the currently investigated point for $\max\left(\sigma_{\theta\theta}\right)$, showing promising results by FRIES & BAYDOUN (2012). Thus, only the criterion for propagation is discussed in this work following two main objectives: First, how to find the most suitable equivalent variable according to (2.92)-(2.95) to model discrete fracture and second, how sensitive the chosen model is to material parameters, mesh and loading conditions. Therefore, a cube containing a straight crack with its front centered in the center of the cube is meshed with $19 \times 19 \times 19$ elements. In order to ensure that the equivalent measure yields crack propagation following the theory of LEFM, seven different displacement boundary

conditions are applied on the boundary of the cube. In case of mixed mode loading, the SIFs are chosen to be equal unless they are chosen to be zero. According to (2.69) and (2.71), the applied displacement field is chosen such that $\mathcal{G} = \mathcal{G}_c$ holds for all computations. Thus, for all computations $\overline{\epsilon} = \kappa_c$ would be the optimal result meaning that $\tilde{\epsilon}$ is able to predict crack growth identical to the theory of LEFM.
The results for the introduced non-local strains (2.92)-(2.95) are displayed in figure 5.42 using material parameters $\mu = 10$, $\Lambda = 20$ and $c = 0.1$: One can see that both energy based formulations (2.92) and (2.93) do not fulfill $\mathcal{G} = \mathcal{G}_c$ for all cases. Using the positive eigenvalues of $\boldsymbol{\varepsilon}$ (2.94) as equivalent measure for crack propagation leads to a fairly precise approximation of crack growth according to the theory of LEFM. However, figure 5.42 displays a lack of accuracy for pure mode I loading conditions. The modified VON MISES criterion (2.95) with $k = 2$ yields the smallest oscillations in the presented examples. Thus, this criterion is applied in the following.

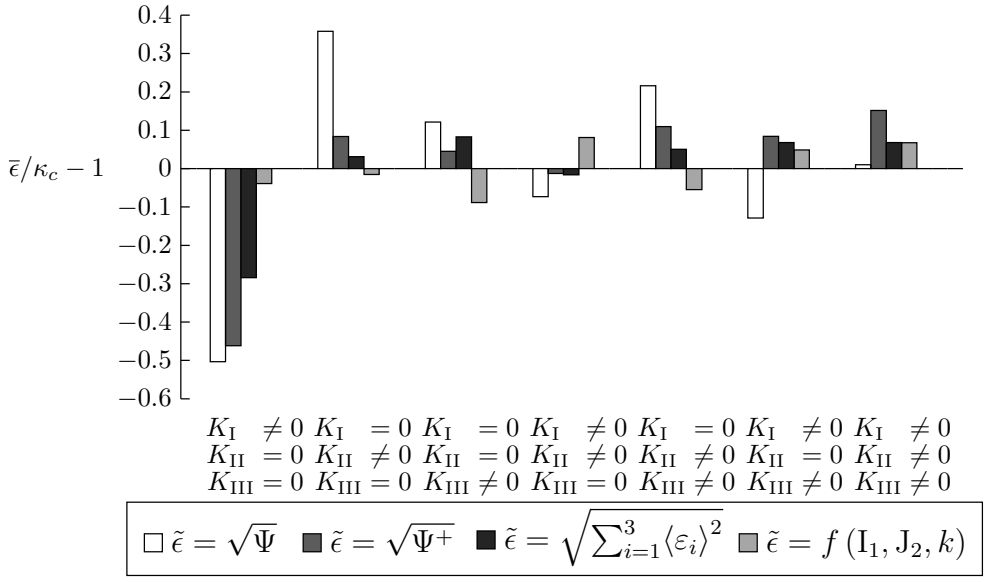

Figure 5.42: Different equivalent strains $\tilde{\epsilon}$ for varying loading conditions.

In the second step the influence of material parameters and mesh in combination with different load cases is investigated: Changing the material constants leads to different boundary conditions according to (2.69), but not to any change in the criterion for crack growth, such that $\mathcal{G} = \mathcal{G}_c$ remains. Rotating the finite element mesh, as displayed in figure 5.43, and applying the adjusted boundary conditions does not change the criterion of growth either. One can see clearly, that the highest non-local equivalent strain appears in the vicinity of the crack front, justifying once more the assumption of the absence of the internal variable D and modeling damage via advancing cracks.
The results of all computations are displayed in figure 5.44: While the results seem to be independent of the internal length scale c and the orientation of the finite element mesh, LAMÉ's constants have a higher impact on the results.
With less than 10% deviation from the optimum in the presented examples, this method still requires further improvement. Comparing this approach to the traditional approach to deter-

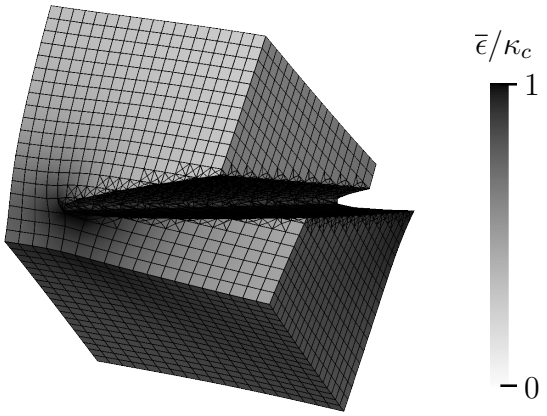

Figure 5.43: Mesh rotated around crack with loading conditions $K_{\mathrm{I}} = K_{\mathrm{II}} = K_{\mathrm{III}}$, $\max(\bar{\epsilon}) = \kappa_c$ and right-hand side $\tilde{\epsilon} = f(\mathrm{I}_1, \mathrm{J}_2, k)$.

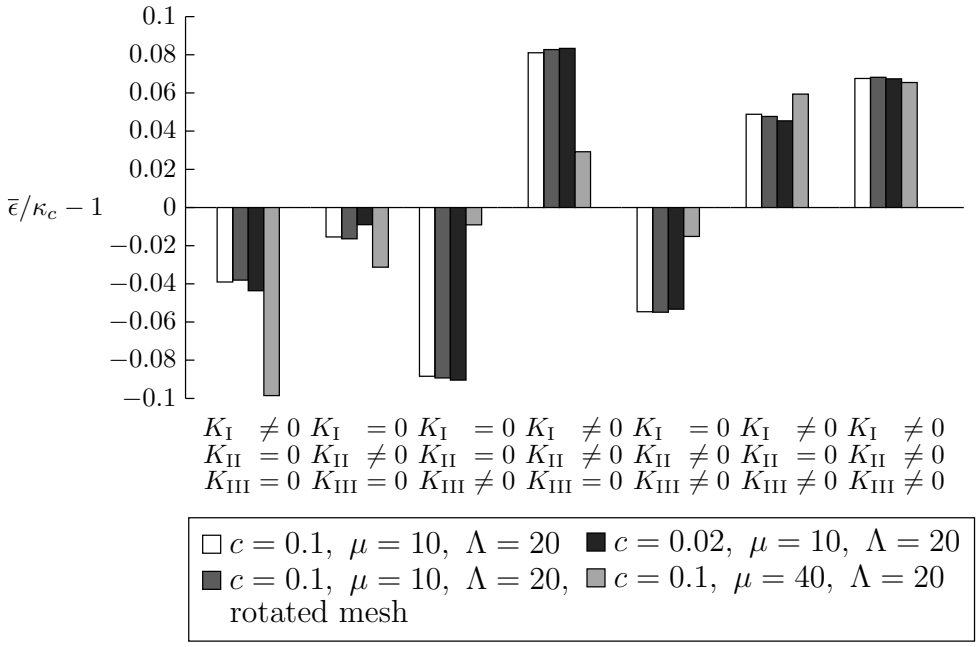

Figure 5.44: Effect of material parameters, mesh orientation and loading conditions on $\bar{\epsilon}$, for $\tilde{\epsilon} = f(\mathrm{I}_1, \mathrm{J}_2, k)$ with $k = 2$.

mine crack propagation via the computation of the J-integral, the proposed method yields minor drawbacks in LEFM. These are the determination of c and κ_c as well as the requirement to solve an extra global equation. Beneficial is the direct outcome of the increment of growth Δa. In case of non-elastic material behavior, the J-integral is difficult to evaluate such that damage models gain attention. Comparing the proposed model to continuous-to-discontinuous approaches by MAZARS & PIJAUDIER-CABOT (1996), WELLS ET AL. (2002), AREIAS & BELYTSCHKO (2005), MEDIAVILLA ET AL. (2006a), SEABRA ET AL. (2013) among others states the benefits of the introduced idea: Due to the assumption that the highest non-local strain occurs always at the crack front, damage might be modeled via

growth of discrete cracks. Thus, in LEFM no history data is required such that a mapping of these internal, quadrature point based variables is not necessary. Furthermore, this assumption yields a weaker coupling between both governing equations, symmetric system matrices and a linear system to solve in linear elasticity, leading to a significant speed-up in computation time. With an appropriate choice of $\tilde{\epsilon}$, this model can be easily applied to non-elastic materials. However, crack initiation, as provided automatically in traditional damage models, has not been included up to now, but is generally a possible extension.

Level set update

Updating the crack front geometry, i.e. in this work the level set fields, can be realized with different techniques, e.g. the fast marching method by SUKUMAR ET AL. (2003), a geometrical approach by FRIES & BAYDOUN (2012) and COLOMBO (2012) or solving the HAMILTON–JACOBI equation by GRAVOUIL ET AL. (2002) among others. Here, a geometrical approach is chosen, as these approaches do not require the solution of another global equation. Furthermore, geometrical approaches do not depend that strongly on the topology of the finite element mesh, as e.g. the finite difference based fast marching method. In contrast to the geometrical approach by FRIES & BAYDOUN (2012), who transfer the global level set fields to explicit crack surfaces, add new triangles to the surfaces and finally transform the resulting surface into level set representation, only the level sets in the vicinities of the advancing fronts are updated in this work.
For all cracks having front displacements of $||\boldsymbol{v}_j|| > 0$ all elements in the vicinity of the advancing crack front within a distance of $r_{\text{tube}} = \max_{j=1,\dots,N_{\text{fp}}} (||\boldsymbol{v}_j||)$ are collected in the set $\mathcal{T}$, yielding a tube around this front with its surface $\partial\mathcal{T}$. This tube contains at least all crack front elements and their neighboring elements. To be computationally efficient, the update of the level set functions is carried out only in $\mathcal{T}$, sketched in figure 5.45.

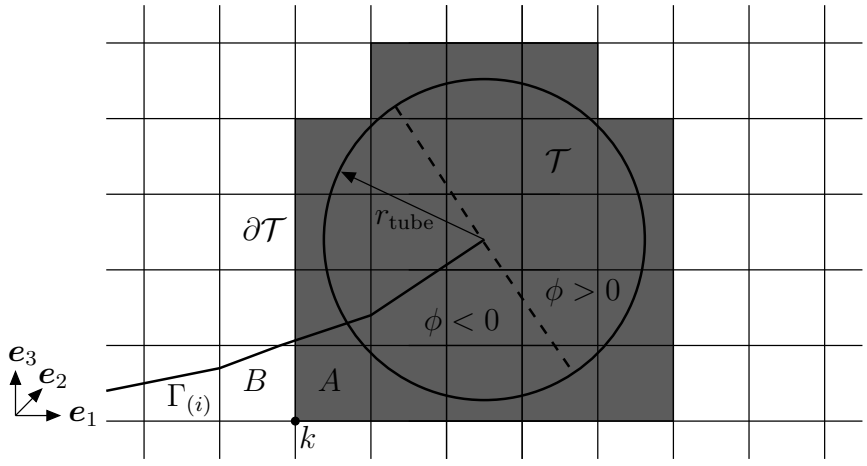

Figure 5.45: Cross section of tube around crack front.

Firstly, all enrichments in $\mathcal{T}\backslash\partial\mathcal{T}$ are deleted. The enrichments on the boundary of the tube need to be persevered, as a local update of the enrichment scheme leads to incorrect enrichments, displayed in figure 5.45: Cracked elements outside the domain, like element B, are

not investigated anymore, such that HEAVISIDE enrichments at node k are missing. Element A is the only element being updated and containing node k, but as this element is not cracked it does not lead to any enrichments at node k. In a second preparation before actually updating the crack surface, all level set values in front of the crack front, i.e. $\phi > 0$, are deleted. Level set values behind the crack front, i.e. $\phi < 0$, remain and will be compared to the newly computed signed distances.
The computed crack front movements $\boldsymbol{v}_j$ and the current points $\hat{\boldsymbol{X}}_j$ form the extension of the current crack $\Gamma_{(i)}$ with its front $\partial\Gamma_{(i)}$ yield a first approximation of the new crack front $\partial\tilde{\Gamma}_{(i+1)}$, displayed in figure 5.46(a). The quadrilateral surfaces spanned by $\boldsymbol{v}_j$, $\hat{\boldsymbol{X}}_j$, $\boldsymbol{v}_{j+1}$ and $\hat{\boldsymbol{X}}_{j+1}$ are subdivided into triangles. Therefore, the arithmetic mean of these four points is computed and connected to two points of the quadrilateral leading to four triangles. By looping all triangles and all elements in $\mathcal{T}$, the shortest distance to the nodes can be determined. Choosing the orientation of all triangles such that their normals $\boldsymbol{n}_{\text{tri}}$ point in a positive direction of $\psi_{(i)}$ at the current step (i), yields the level set field $\psi_{(i+1)}$ for the crack surface for the following step $(i+1)$. Note that, as the angle of growth using the criterion of maximum hoop is restricted to 70.5^{o}, the signed distance can be computed uniquely using the dot product $\nabla\psi_{(i+1)} \cdot \boldsymbol{n}_{\text{tri}} > 0$.
However, the first approximation of the crack front $\partial\tilde{\Gamma}_{(i+1)}$ cannot be captured using a trilinear interpolation of ϕ. As this line might contain one or even more kinks in one finite element. Thus, an interpolation of the crack surface is required. Therefore, the intersection points $\hat{\boldsymbol{x}}_j$ between finite elements and $\partial\tilde{\Gamma}_{(i+1)}$ are computed. Connecting all points leads to an suitable approximation of the crack front $\partial\Gamma_{(i+1)}$, with $\hat{\boldsymbol{x}}_j \in \partial\Gamma_{(i+1)} \ \wedge \ \hat{\boldsymbol{x}}_j \in \partial\tilde{\Gamma}_{(i+1)}$, displayed in figure 5.46(b).

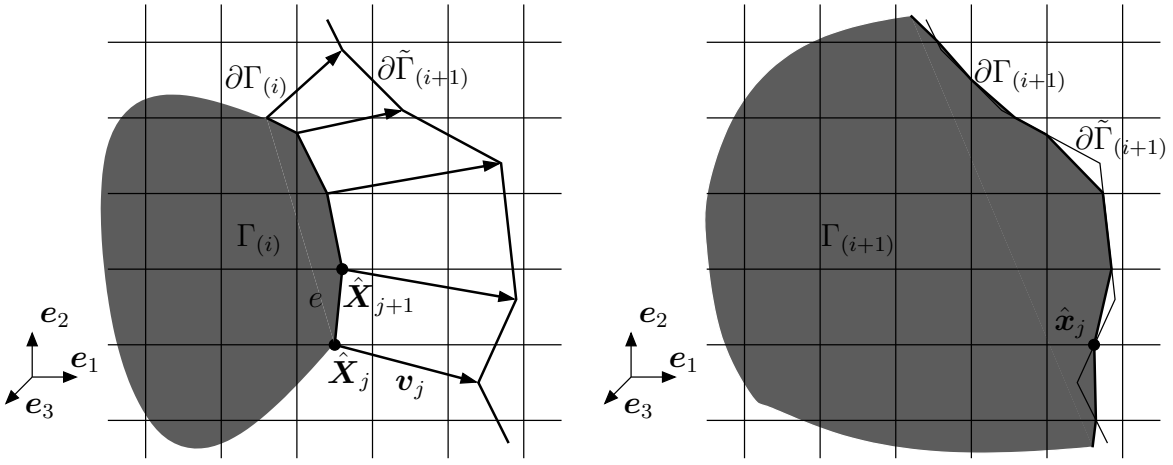

(a) First approximation of new crack front $\partial\tilde{\Gamma}_{(i+1)}$.

(b) Final approximation of crack front $\partial\Gamma_{(i+1)}$.

Figure 5.46: 3D crack surface update.

In order to satisfy $\nabla\psi \cdot \nabla\phi = 0$, a least square method is applied in each crack front element to obtain the nodal values of the second level set field

$$\Pi_\phi = \int_{\Omega_e} (\nabla\psi \cdot \nabla\phi)^2 \, \mathrm{d}V \quad . \tag{5.21}$$

To achieve an accurate approximation of the level set field, this equation is constrained using a LAGRANGE multiplier method, such that the level set value is zero at both intersection points $\hat{\boldsymbol{x}}_1$ and $\hat{\boldsymbol{x}}_2$ in the current finite element

$$\begin{aligned} \Pi_{\lambda_1} &= \lambda_1 \, \phi\left(\hat{\boldsymbol{x}}_1\right) \quad , \\ \Pi_{\lambda_2} &= \lambda_2 \, \phi\left(\hat{\boldsymbol{x}}_2\right) \quad , \end{aligned} \tag{5.22}$$

yielding the overall potential

$$\Pi = \Pi_\phi + \Pi_{\lambda_1} + \Pi_{\lambda_2} \quad . \tag{5.23}$$

The variation of Π

$$\left[\begin{array}{ccc} \delta_\phi \Pi & \delta_{\lambda_1} \Pi & \delta_{\lambda_2} \Pi \end{array} \right] = \left[\begin{array}{c} 0 \end{array} \right] \quad , \tag{5.24}$$

yields the linear system of equations

$$\left[\begin{array}{ccc} \frac{\partial^2 \Pi}{\partial \phi \, \partial \phi} & \frac{\partial^2 \Pi}{\partial \phi \, \partial \lambda_1} & \frac{\partial^2 \Pi}{\partial \phi \, \partial \lambda_2} \\ \frac{\partial^2 \Pi}{\partial \lambda_1 \, \partial \phi} & \frac{\partial^2 \Pi}{\partial \lambda_1 \, \partial \lambda_1} & \frac{\partial^2 \Pi}{\partial \lambda_1 \, \partial \lambda_2} \\ \frac{\partial^2 \Pi}{\partial \lambda_2 \, \partial \phi} & \frac{\partial^2 \Pi}{\partial \lambda_2 \, \partial \lambda_1} & \frac{\partial^2 \Pi}{\partial \lambda_2 \, \partial \lambda_2} \end{array} \right] \cdot \left[\begin{array}{c} \Delta \phi \\ \Delta \lambda_1 \\ \Delta \lambda_2 \end{array} \right] = - \left[\begin{array}{c} \frac{\partial \Pi}{\partial \phi} \\ \frac{\partial \Pi}{\partial \lambda_1} \\ \frac{\partial \Pi}{\partial \lambda_2} \end{array} \right] \quad . \tag{5.25}$$

Applying some derivatives leads to the system being solved

$$\left[\begin{array}{ccc} \frac{\partial^2 \Pi}{\partial \phi \, \partial \phi} & 1 & 1 \\ 1 & 0 & 0 \\ 1 & 0 & 0 \end{array} \right] \cdot \left[\begin{array}{c} \Delta \phi \\ \Delta \lambda_1 \\ \Delta \lambda_2 \end{array} \right] = - \left[\begin{array}{c} \frac{\partial \Pi}{\partial \phi} \\ \phi\left(\hat{\boldsymbol{x}}_1\right) \\ \phi\left(\hat{\boldsymbol{x}}_2\right) \end{array} \right] \quad . \tag{5.26}$$

Following (3.19), ϕ is discretized using trilinear shape functions and eight nodal unknowns, resulting in a 10×10 system of equations. However, as the gradients of the first level set field are not C^0- continuous, ϕ itself is not C^0- continuous: The nodal values of ϕ depend on the current finite element. Therefore, the mean average of the nodal unknowns is computed using the computed unknowns from all neighboring elements. Thus, the gradients of the level set fields are not perfectly orthogonal. However, this procedure leads to a very good compromise between accuracy, computation time and nearly orthogonal level set gradients. Finally, the enrichments are set according to the new crack geometry such that all quantities for the following load step are determined.
The overall numerical propagation algorithm is equivalent to two-dimensional problems, sketched in table 5.1. Here, the adaption of the external boundary conditions is applied analogously to two-dimensional problems according to equation (5.3).

Implementation details

Even though the main ideas for three-dimensional crack propagation problems can be adopted one-to-one from two-dimensional problems, the implementation of crack propagation is different due to the fact of a whole line moving in space instead of independent points. As not all the cracks in the domain propagate and the nodal level set values are stored as a global quantity not assigned to a particular crack, a direct application of growth to all cracks would lead to several propagating cracks. To avoid this phenomenon and apply crack

propagation only to cracks fulfilling the criterion for growth makes an assignment and sorting of crack segments inevitable. To avoid searching for the neighboring front points of $\hat{\boldsymbol{X}}_j$ to set up the discrete surfaces to determine ψ, the front points $\hat{\boldsymbol{X}}_j$ and their properties are sorted such that in the array $\hat{\boldsymbol{X}}_{(\cdot)}$ neighboring discrete points are assignment to the same finite element e, i.e. $\hat{\boldsymbol{X}}_j \in \Omega_e \ \wedge \ \hat{\boldsymbol{X}}_{j+1} \in \Omega_e$, as displayed in figure 5.46(a). Therefore, two arrays are set up, displayed in figure 5.47: The pointer $n_{\mathrm{tf}}(c)$ defines the position at which a discrete point of the advancing crack c starts and ends. Its length depends on the number of propagating cracks n_{crp}, such that $1 \leq c \leq n_{\mathrm{crp}} + 1$. The second array contains besides coordinates all nodal data required at point $\hat{\boldsymbol{X}}_j$ to determine the nodal level set values, i.e. the propagation increment $\boldsymbol{v}_j$, the two elements assigned to this point $\mathrm{elem}_{\mathrm{cf}}(\{1,2\}, j)$ as well as the crack face normal at step (i) to determine the correct sign for the level set function. The assignment of $\hat{\boldsymbol{X}}_j$ to both elements $\mathrm{elem}_{\mathrm{cf}}(\{1,2\}, j)$ is required to determine the averaged local basis $\boldsymbol{g}_i$. The size of this second array thus depends on the number of propagating discrete front points n_{p}, such that $1 \leq j \leq n_{\mathrm{p}}$, with $n_{\mathrm{tf}}(n_{\mathrm{crp}} + 1) = n_{\mathrm{p}}$.

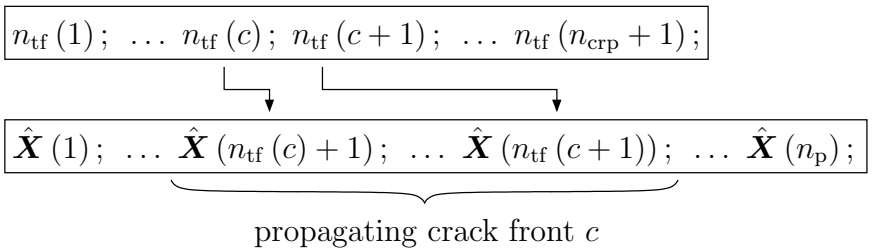

Figure 5.47: Storage of propagating crack fronts.

A pseudo-code of this sorting algorithm is displayed in table 5.7. Here, n_{crf} is the total number of discrete front points and $\boldsymbol{x}_{\mathrm{cf}}(\{1,2\}, k)$ refers to the two front points of element k. This variable is not a global array, as the computation in terms of the level set of these points is comparably cheap. The logical array ℓ_{done} is required to avoid looping an element twice, which might otherwise lead to an infinite looping of lines 9 - 31. As the first followed point $\boldsymbol{x}_{\mathrm{cf}}(1, i)$ referring to the initially propagating element i is generally not a point on the boundary of the domain, the second point $\boldsymbol{x}_{\mathrm{cf}}(2, i)$ needs to be followed after inverting the already determined arrays. Thus, sorted arrays according to figure 5.47 are achieved, independent of the crack front geometry, i.e. an enclosed front like a ring or a line in space ending at the boundary of the domain. As cracks change during computation process, this sorting algorithm is applied at every load step.

```
1  n_crp = 0 , n_p = 0 , ℓ_done ( ) = 0 , n_tf (1) = 0
2  loop i = 1, n_crf
3     if (i propagates ∧ ℓ_done (i) = 0)
4        m = 1 , j = 0 , ℓ_done (i) = 1
5        n_crp = n_crp + 1 , n_p = n_p + 1
6        elem_cf (1, n_p) = i
7        X̂ (n_p) = x_cf (m, i)
8        compute and store propagation increment v_{n_p} and current crack face normal
9        do while (j < n_crf)
10          j = j + 1
11          if (X̂ (n_p) = x_cf (1, j)) ; k = 1
12          elseif (X̂ (n_p) = x_cf (2, j)) ; k = 2
13          else k = 0
14          if (k ≠ 0 ∧ ℓ_done (j) = 0)
15             n_p = n_p + 1
16             elem_cf (2, n_p − 1) = j
17             elem_cf (1, n_p) = j
18             X̂ (n_p) = x_cf (k, j)
19             compute and store propagation increment v_{n_p} and current crack face normal
20             ℓ_done (j) = 1 , j = 0
21          endif
22          if (j = n_crf ∧ m = 1)
23             m = 2
24             invert arrays v( · ), elem_cf( · , · ) and X̂( · ) from entries p to n_p to restart from the
               originally propagating element i using its second intersection point x_cf (2, i)
25             n_p = n_p + 1
26             elem_cf (1, n_p) = i
27             X̂ (n_p) = x_cf (m, i)
28             compute and store propagation increment v_{n_p} and current crack face normal
29             ℓ_done (j) = 1 , j = 0
30          endif
31       enddo
32       n_tf (n_crp + 1) = n_p
33    endif
34 end loop
```

Table 5.7: Finding and sorting advancing crack fronts.

Computational examples

To verify that the proposed model is able to capture the required mechanical features, comparably simple examples are considered first. The following examples demonstrate the robustness and flexibility of the introduced method. In all examples LAMÉ's material constants are chosen to $\mu = 10$, $\Lambda = 20$ and the fracture energy is $\mathcal{G}_c = 1$. The geometrical measurements $a = \frac{6}{19}$, $\ell = 2$ hold for all following examples as well.

Tearing and shearing of a single cracked domain

To demonstrate that the three-dimensional model for crack growth is able to reflect simple shearing and tearing conditions accurately, a domain containing a straight crack in $\boldsymbol{e}_1$ - $\boldsymbol{e}_2$ plane is loaded with respective boundary conditions $\overline{\boldsymbol{u}}_1$ and $\overline{\boldsymbol{u}}_2$, displayed in figure 5.48. Here, the origin is located in the center of the cuboid, which is meshed with $19 \times 3 \times 19$ elements.

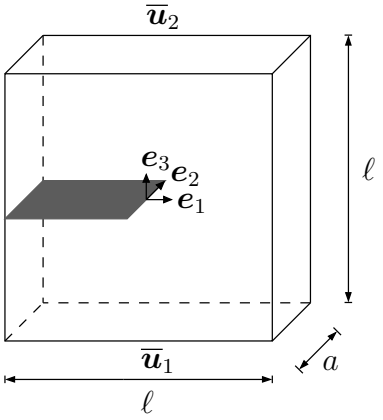

Figure 5.48: Straight crack.

To apply only tearing, the DIRICHLET boundary conditions read

$$\begin{aligned} \overline{\boldsymbol{u}}_1(\overline{\boldsymbol{x}}_1) &= u_1\,\boldsymbol{e}_1 + u_2\,\boldsymbol{e}_2 + 0\,\boldsymbol{e}_3 \quad \text{with} \quad \overline{\boldsymbol{x}}_1 = x_1\,\boldsymbol{e}_1 + x_2\,\boldsymbol{e}_2 - \ell/2\,\boldsymbol{e}_3 \quad , \\ \overline{\boldsymbol{u}}_2(\overline{\boldsymbol{x}}_2) &= u_1\,\boldsymbol{e}_1 + u_2\,\boldsymbol{e}_2 + \lambda\,\boldsymbol{e}_3 \quad \text{with} \quad \overline{\boldsymbol{x}}_2 = x_1\,\boldsymbol{e}_1 + x_2\,\boldsymbol{e}_2 + \ell/2\,\boldsymbol{e}_3 \quad . \end{aligned}$$

Here, u_i and x_i are the unknowns of the displacement field and the components of the position vector respectively. The VON MISES stress distribution after crack propagation as well as the corresponding crack path are displayed in figure 5.49. Similar to two-dimensional problems, the VON MISES stress is highest at the crack front and appears in a typical kidney-shape around the crack front. Furthermore, the crack grows straight through the domain, with its front being a straight line parallel to the $\boldsymbol{e}_2$ - axis. Thus, for this simple loading condition, the model predicts the crack path sufficiently accurately.
The application of pure mode II displacement boundary conditions on the entire boundary is not straight forward as the nodal unknowns of the enrichment functions on the boundary of the domain require defined values as well. Thus, shearing boundary conditions are applied

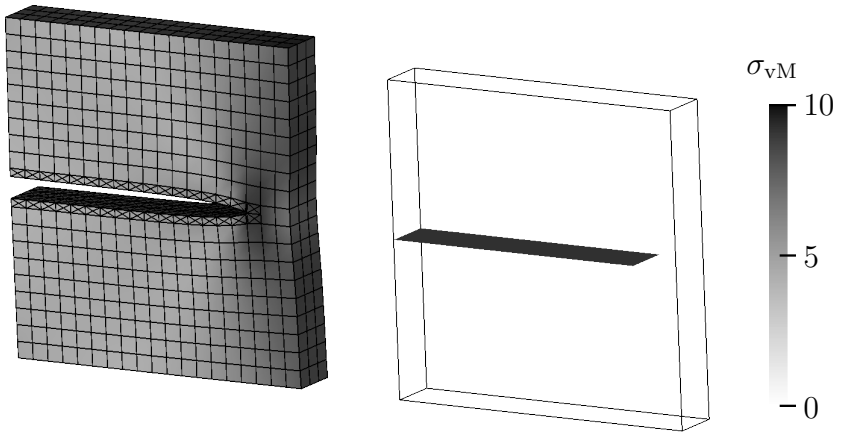

Figure 5.49: Tensile test. Left: Deformed structure. Right: Crack path in undeformed domain.

here by changing $\overline{\boldsymbol{u}}_1$ and $\overline{\boldsymbol{u}}_2$ to

$$\begin{aligned} \overline{\boldsymbol{u}}_1\left(\overline{\boldsymbol{x}}_1\right) &= 0\,\boldsymbol{e}_1 + u_2\,\boldsymbol{e}_2 + 0\,\boldsymbol{e}_3 \quad \text{with} \quad \overline{\boldsymbol{x}}_1 = x_1\,\boldsymbol{e}_1 + x_2\,\boldsymbol{e}_2 - \ell/2\,\boldsymbol{e}_3 \quad , \\ \overline{\boldsymbol{u}}_2\left(\overline{\boldsymbol{x}}_2\right) &= \lambda\,\boldsymbol{e}_1 + u_2\,\boldsymbol{e}_2 + u_3\,\boldsymbol{e}_3 \quad \text{with} \quad \overline{\boldsymbol{x}}_2 = x_1\,\boldsymbol{e}_1 + x_2\,\boldsymbol{e}_2 + \ell/2\,\boldsymbol{e}_3 \quad . \end{aligned}$$

The VON MISES stress distribution of the final crack propagation step and the final crack path are displayed in figure 5.50. The crack deflects 69.3^{o} in its first crack propagation step which almost resembles the analytical solution of pure mode II crack propagation, i.e. 70.5^{o}. As the applied shearing boundary conditions contain some displacements reflected by mode I, i.e. $K_{\mathrm{I}} \neq 0$, a slight decrease of the angle of deflection is reasonable. After some steps of crack propagation, the angle of deflection decreases slightly and in the proceeding steps it increases again, leading to small oscillations of the crack surface. This indicates minor errors in the extraction of the SIFs, but as the crack turns back onto its old trajectory, these errors seem uncritical. Furthermore, as in the tearing example, the crack front is a straight line parallel to the $\boldsymbol{e}_2$ - axis. Consequently, the proposed model is able to predict the crack path highly accurately for simple loading cases.

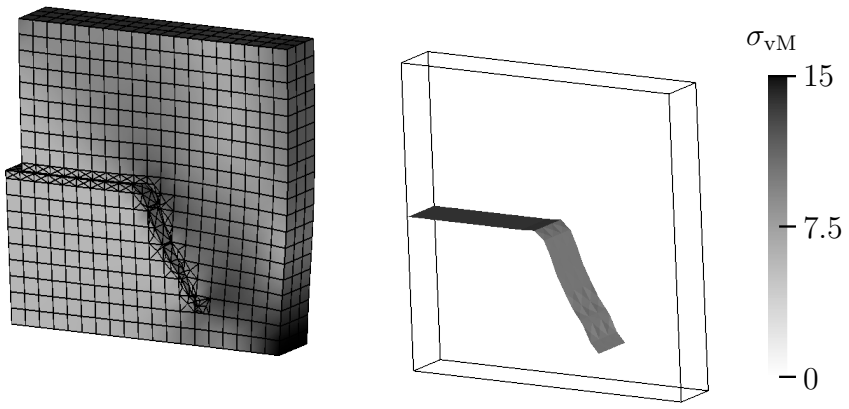

Figure 5.50: Shear test. Left: Deformed structure. Right: Crack path in undeformed domain.

Mixed mode loading of skew crack

In order to verify if the model generally holds for three-dimensional problems, the introduced crack is now tilted by $\pi/6$ around $\boldsymbol{e}_1$, displayed in figure 5.51.

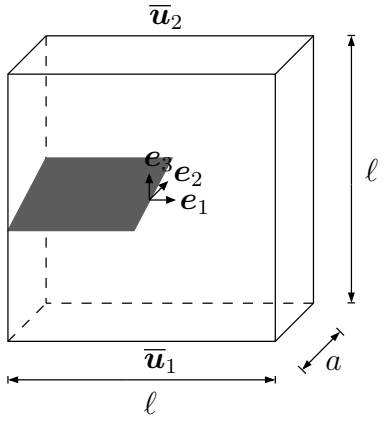

Figure 5.51: Skew crack, rotated by $\pi/6$ around $\boldsymbol{e}_1$.

Furthermore, the DIRICHLET boundary conditions contain shearing and tearing equally, yielding

$$\begin{aligned} \overline{\boldsymbol{u}}_1(\overline{\boldsymbol{x}}_1) &= 0\,\boldsymbol{e}_1 + 0\,\boldsymbol{e}_2 \;+ 0\,\boldsymbol{e}_3 \quad \text{with} \quad \overline{\boldsymbol{x}}_1 = x_1\,\boldsymbol{e}_1 + x_2\,\boldsymbol{e}_2 - \ell/2\,\boldsymbol{e}_3 \quad , \\ \overline{\boldsymbol{u}}_2(\overline{\boldsymbol{x}}_2) &= \lambda\,\boldsymbol{e}_1 + u_2\,\boldsymbol{e}_2 + \lambda\,\boldsymbol{e}_3 \quad \text{with} \quad \overline{\boldsymbol{x}}_2 = x_1\,\boldsymbol{e}_1 + x_2\,\boldsymbol{e}_2 + \ell/2\,\boldsymbol{e}_3 \quad . \end{aligned}$$

Thus, mode I and mode II are applied via external loading, while mode III is applied via tilting the crack around $\boldsymbol{e}_1$. The resulting crack path and stress distribution is displayed in figure 5.52.

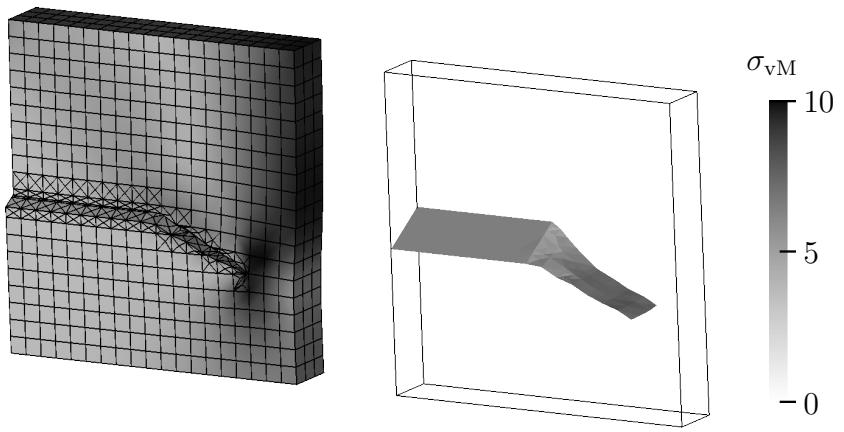

Figure 5.52: Mixed mode loading. Left: Deformed structure. Right: Crack path in undeformed domain.

In the beginning of the simulation the crack front rotates around $\boldsymbol{e}_1$ until it is parallel to $\boldsymbol{e}_2$. The direction of growth is then between mode I and mode II loading, which reflects the

external boundary conditions. LAZARUS ET AL. (2008) made similar investigations experimentally: Instead of applying tearing and shearing, the structure is only torn apart. Similar the example presented here, the crack turns around $\boldsymbol{e}_1$ until the crack front is parallel to $\boldsymbol{e}_2$. It subsequently follows a straight path in the experiment, as if only tearing is applied. Thus, in the numerical as well as in the experimental setup the direction of propagation changes until it matches the applied boundary conditions.
Besides the reasonable crack path, this example exhibits the splendid flexibility of the presented model: The interpolation of the crack face and the update of the level set field is able to represent twisting cracks. Complicated crack paths can be tracked, such that this model can be applied to more general problems.

Propagation of circular crack

The last example in this section investigates a circular crack with diameter 1 in a cuboid with the dimension $2 \times 2 \times 1.3$. The block is meshed with $17 \times 17 \times 11$ elements and loaded with displacement boundary conditions $\lambda\,\overline{\boldsymbol{u}}$, perpendicular to the crack surface. Figure 5.53(a) displays the loaded configuration with the initial crack surface. Here, the external load is adjusted such that crack propagation is just avoided. In the following displayed load steps the crack grows while the external load $\lambda\,\overline{\boldsymbol{u}}$ decreases. Note that, once the crack propagates through the boundary of the domain the evaluation of the J-integral becomes slightly inaccurate at these positions. However, to demonstrate the flexibility of the surface update, the computation is continued. In figure 5.53(c) technically four crack fronts exist which are all cutting off one corner of the domain. Due to slight numerical inaccuracies in terms of SIF extraction, the stabilization with λ and the restriction that only one crack propagates, at least four steps of propagation are required to result in a symmetric crack configuration again, displayed in e.g. figure 5.53(d). According to the direction of $\overline{\boldsymbol{u}}$, the crack is growing in its plane which can be captured accurately with this model. The ability of the crack to grow through the boundary of the domain is successfully displayed here.

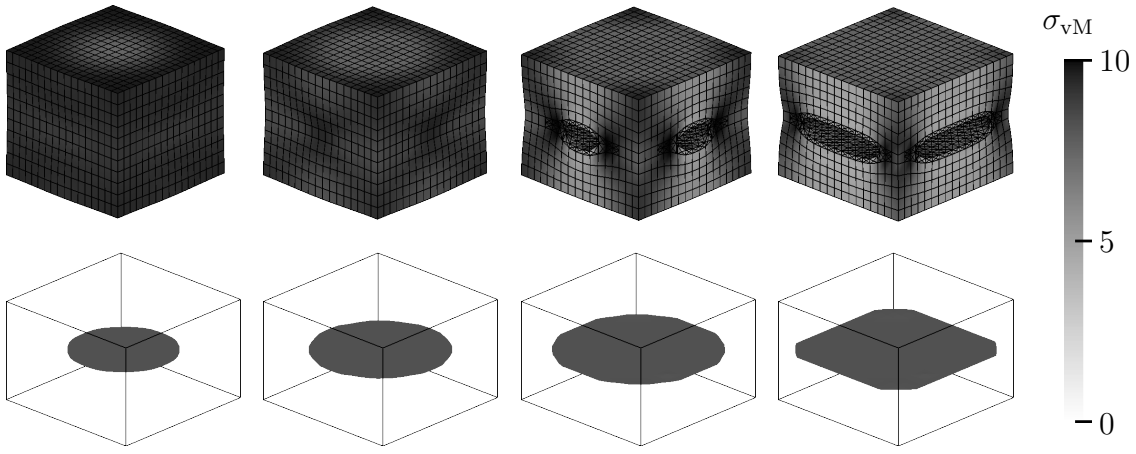

(a) $\lambda = 3.18$ (b) $\lambda = 2.99$ (c) $\lambda = 2.67$ (d) $\lambda = 2.34$

Figure 5.53: Circular crack advancing. Top: Deformed structure. Bottom: Crack path in undeformed domain.

These four examples demonstrate the main features of the proposed method: The mechanical model is able to predict the direction of crack growth accurately for mode I, mode II and mode III crack propagation. Furthermore, an efficient crack surface update tracks the crack surface independently of the element shape and the boundary of the domain. Thus, this method can be applied to more general problems as well as multiscale analysis.

5.3.2 Multiscale crack propagation

In the context of multiscale analysis a so-called global-local GFEM (GFEM$^{\text{gl}}$) approach, proposed by PEREIRA ET AL. (2012), reveals its benefits from a fine scale computation to determine crack growth with higher accuracy: Fine scale effects are not considered in the GFEM$^{\text{gl}}$, such that the fine scale computation is applied to gain more accurate results especially at the crack front. A strong coupling between the scales and embedding the fine scale crack path directly into the global problem yields a highly accurate tool to determine crack growth of coarse scale cracks. However, considering fine scale defects explicitly in the global problem leads to a vast increase of the computation time. Consequently, the GFEM$^{\text{gl}}$ is not applicable in the context of multiscale analysis. Thus, similar to two-dimensional problems, the multiscale projection method is applied, to take into account microcracks efficiently using a weak coupling between scales, introduced by HOLL ET AL. (2014).
In the multiscale projection method, all cracks are known explicitly only at the finest scale. Thus, the criterion for crack propagation and the computation of the direction of growth need to be carried out on this scale, such that all cracks are able to propagate. Consequently, the coarse scale is fully driven by the fine scale. As advancing microcracks are only taken into account on the fine scale explicitly, the propagation can be fully evaluated on this scale following the introduced singlescale approach. Interpolating advancing macrocracks in two-dimensional multiscale simulations onto the coarse scale is similar to two-dimensional singlescale analysis. However, three-dimensional interpolation of the crack path is not as straight forward due to the fact that a whole line instead of a single point advances.
Computing $\partial\tilde{\Gamma}^0_{(i+1)}$ using the intersection points of the finite elements with the fine scale fronts $\partial\Gamma^1_{(i+1)}$ or $\partial\tilde{\Gamma}^1_{(i+1)}$ would neglect several fine scale features, as a lot of vectors $\boldsymbol{v}^1_j$ in between those intersection points would be ignored. Evaluating alternatively only at intersection points $\hat{\boldsymbol{X}}^0_I$ on the fine or coarse scale domain drops a lot of fine scale features as well. The computation of level sets on the fine scale would take all effects into account, but is also not an appropriate option as piecewise trilinear level set approximation within a single coarse scale element would require higher order approximation. However, this would lead to an extreme extension of the proposed method and would increase the costs for integrating cracked coarse scale element significantly. Therefore, all fine scale front displacements $\boldsymbol{v}^1_i$ are trilinearly averaged to receive the coarse scale propagation vectors $\boldsymbol{v}^0_j$, displayed in figure 5.54. With

$$\boldsymbol{v}^0_I = \sum_{j=1}^{n^0_{\text{parts}}} \frac{\max\left(d_j\right)}{\sum_{i=1}^{n^0_{\text{parts}}} \max\left(d_i\right)} \left(\frac{1}{\sum_{i=1}^{n^1_{\text{fp},j}} d_i} \sum_{i=1}^{n^1_{\text{fp},j}} \left(1 - d_i\right) \boldsymbol{v}^1_i \right) \quad , \tag{5.27}$$

the whole crack front can be mapped onto the coarse scale, by taking all fine scale effects into account. Here, n^0_{parts} is the number of coarse scale crack segments joining the current

discrete front point $\hat{\boldsymbol{X}}_I^0$ such that

$$n_{\text{parts}}^0 = \begin{cases} 1 & \forall\, \hat{\boldsymbol{X}}_I^0 \in \partial\Omega^0 \\ 2 & \forall\, \hat{\boldsymbol{X}}_I^0 \in \Omega^0 \backslash \partial\Omega^0 \end{cases} \quad . \tag{5.28}$$

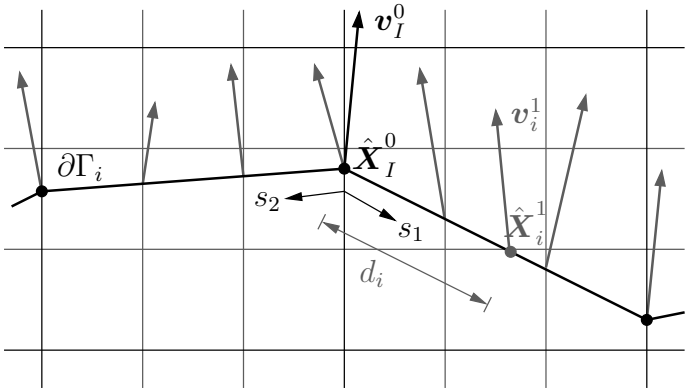

Figure 5.54: Approximation of crack front $\boldsymbol{v}_I^0$ using fine scale results $\boldsymbol{v}_i^1$. Fine scale properties as mesh and vectors are colored gray, coarse scale properties are colored black.

The variable $n_{\text{fp},j}^1$ is the number of discrete fine scale points $\hat{\boldsymbol{X}}_i^1$ of segment j, with $n_{\text{fp},j}^1 \geq 2$ as the coarse scale element itself has two intersection points. This variable depends, besides on the number of fine scale elements per coarse scale element, mainly on the position of the macrocrack in the coarse scale element. With the distance d_i

$$d_i = \left|\left| \hat{\boldsymbol{X}}_I^0 - \hat{\boldsymbol{X}}_i^1 \right|\right| \quad , \tag{5.29}$$

all variables are known to determine the coarse scale quantity $\boldsymbol{v}_I^0$. Finally, these vectors are passed to the coarse scale on which the level set update is performed, according to the introduced singlescale approach.
In order to ensure stable crack growth, the external boundary conditions are updated according to section 5.1.2. Finally, the algorithm sketched in table 5.2 is applied to model several steps of crack propagation.

Implementation details

Similarly to the singlescale approach, the crack fronts are sorted into arrays as depicted in figure 5.47. In contrast to singlescale analysis, the evaluation of crack propagation is carried out on the fine scale domains such that all crack fronts are stored using the algorithm introduced in table 5.7. As this sorting algorithm can distinguish between different crack fronts and as non-overlapping fine scale domains can be treated independently from each other, projecting boundary conditions and solving fine scale domains is computed in parallel using OPENMP. In case one coarse scale element is assigned to two or more crack tips, the respective fronts merge to one enlarged fine scale domain. After convergence of the multiscale analysis, the criterion for crack growth including the propagation increments $\boldsymbol{v}_I^0$

are computed on the fine scale and passed to the coarse scale at the respective point in the array to its position vector $\hat{\boldsymbol{X}}_J^0$.

Computational examples

The following computational examples demonstrate the flexibility of the multiscale method combined with the proposed crack propagation algorithm. First, the ability of merging fine scale domains is demonstrated and then the effect of microcracks is investigated in the following example. In these examples LAMÉ's material constants are chosen to $\mu = 10$, $\Lambda = 20$ and the fracture energy is $\mathcal{G}_c = 1$. Finally, this method is applied to a gas turbine blade to investigate crack growth on the micro level.

Multiple cracks

To demonstrate the ability to merge fine scale domains, two cracks are considered here as displayed in figure 5.55. The geometrical measurements are set to $a = \frac{6}{19}$, $\ell = 2$, $c_1 = \frac{8}{19}$ and $c_2 = \frac{11}{19}$, and the fine scale radius is $r_{\mathrm{MS}} = 3 \cdot \frac{\sqrt{3}}{19} \approx 0.273$. The domain is meshed using $19 \times 3 \times 19$ coarse scale elements and $5 \times 5 \times 5$ fine scale elements per coarse scale element yielding an effective mesh of $95 \times 15 \times 95$ elements. The structure is loaded with the boundary conditions

$$\begin{aligned} \overline{\boldsymbol{u}}_1^0(\overline{\boldsymbol{x}}_1) &= 0\,\boldsymbol{e}_1 \quad + 0\,\boldsymbol{e}_2 \; + 0\,\boldsymbol{e}_3 \quad \text{with} \quad \overline{\boldsymbol{x}}_1 = x_1\,\boldsymbol{e}_1 + x_2\,\boldsymbol{e}_2 - \ell/2\,\boldsymbol{e}_3 \quad , \\ \overline{\boldsymbol{u}}_2^0(\overline{\boldsymbol{x}}_2) &= -\lambda^0\,\boldsymbol{e}_1 + u_2^0\,\boldsymbol{e}_2 + \lambda^0\,\boldsymbol{e}_3 \quad \text{with} \quad \overline{\boldsymbol{x}}_2 = x_1\,\boldsymbol{e}_1 + x_2\,\boldsymbol{e}_2 + \ell/2\,\boldsymbol{e}_3 \quad . \end{aligned}$$

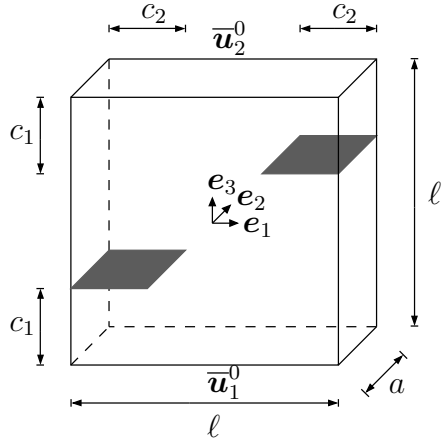

Figure 5.55: Two straight cracks in cuboid.

As the external load is adjusted such that the highest energy release rate is equal to its material parameter, only the upper crack propagates, displayed in figure 5.56(a). Due to $\overline{\boldsymbol{u}}_1^0$ and $\overline{\boldsymbol{u}}_2^0$ and the presence of the non-growing crack, the propagating crack tilts towards the other crack front. As long as the fine scale domains do not overlap, the projection of the boundary conditions as well as the complete fine scale computation can be performed in parallel. When both fine scale domains merge, one larger fine scale domain emerges in which only

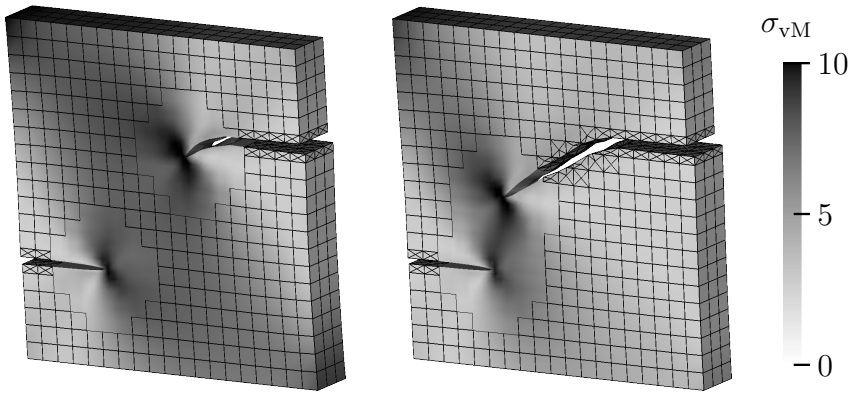

(a) Separated fine scale domains.

(b) Merged fine scale domains.

Figure 5.56: VON MISES stress σ_{vM} of multiple coarse scale cracks in domain.

one crack propagates, displayed in figure 5.56(b).
This example demonstrates two major features of the multiscale projection method in combination with crack propagation. As long as fine scale domains do not overlap, they can be treated independently such that a parallelization via OPENMP saves computation time compared to serial computations. Merging fine scale domains can be captured as well, showing again the great flexibility of the proposed method. However, merged fine scale domains can not be computed in parallel anymore.
At first glance, a single advancing circular crack, as displayed in figure 5.57, does not clearly belong to the section *Multiple cracks*.

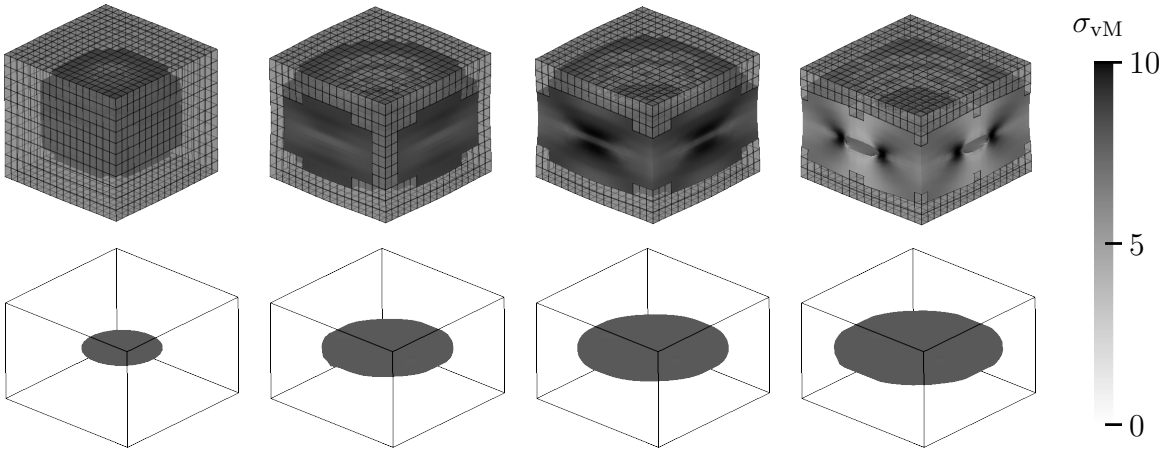

Figure 5.57: Circular crack advancing. Top: Deformed structure with transparent coarse scale domain and fine scale domain displaying VON MISES stress. Bottom: Crack path in undeformed domain.

However, with extension of the crack surface as displayed in figure 5.57 the front is advancing through the boundary of the domain. Thus, from one propagation step to another, four crack fronts exist instead of one, each cutting off a corner displayed in figure 5.57(c). Consequently, four fine scale domains exist each referring to one crack front. As the fine

scale domains overlap, only one merged fine scale is computed containing four independent crack fronts. Thus, analogously to the singlescale example only one of the fronts propagates such that after four propagation steps the problem is symmetric again, as illustrated in figure 5.57(d). Here, the boundary conditions, the coarse scale mesh and the geometry is chosen to be identical to the introduced singlescale example. For the fine scale computation, each coarse scale element is subdivided into $3 \times 3 \times 3$ fine scale elements.
This example reveals once more the flexibility of the proposed multiscale method. It demonstrates furthermore that the introduced multiscale technique is able to handle enclosed crack fronts as well as open crack fronts. As no microcracks are considered here, the crack surface resembles the surface obtained in the singlescale computation.

Effect of microcracks on propagating crack front

The influence of microcracks on the global response of a structure is investigated in the example displayed in figure 5.51. Computing the crack path in a multiscale analysis without taking microcracks into account is displayed in figure 5.58. Neither the final crack path nor the stress distribution change significantly compared to the singlescale analysis, illustrated in figure 5.52. Due to the $5 \times 5 \times 5$ finer resolution in the fine scale domain at the crack front, the SIF extraction obtains a higher precision leading to a slight change in direction of growth.

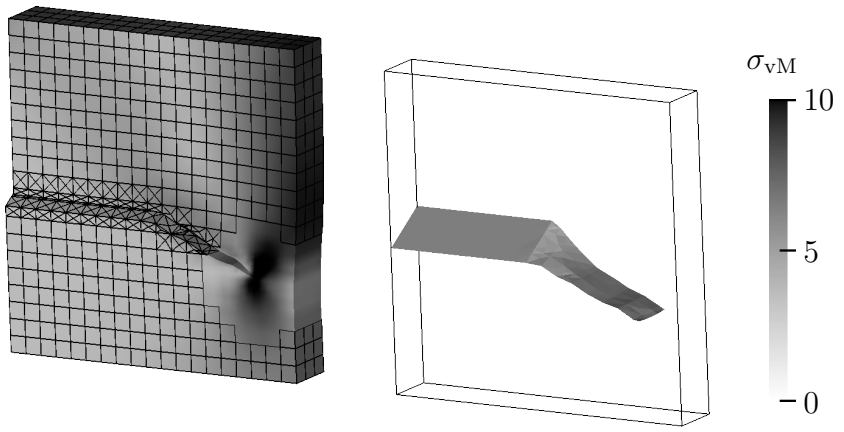

Figure 5.58: Mixed mode loading. Left: Deformed structure. Right: Crack path.

To investigate the effect microcracks have on crack propagation, 51 circular microcracks are now considered as displayed in figure 5.59. The distribution of these cracks is random, but such that the respective level set fields do not interfere each other. The crack path and stress distribution is displayed in figure 5.59. The turning of the crack front around $\boldsymbol{e}_1$ is similar to computations without microcracks, but the angle of deflection increases slightly. Once the crack front reaches a microcrack such that one node receives nodal level set values originating from different cracks, the cracks are close enough to merge. As this feature is not implemented in this work, the computation stops.
Thus, the crack path can be compared at the final load step of the computation taking microcracks into account. Apart from the slightly smaller load factor λ^0 of 2% once microcracks are considered, the different crack paths are displayed in figure 5.60(a): This overview states

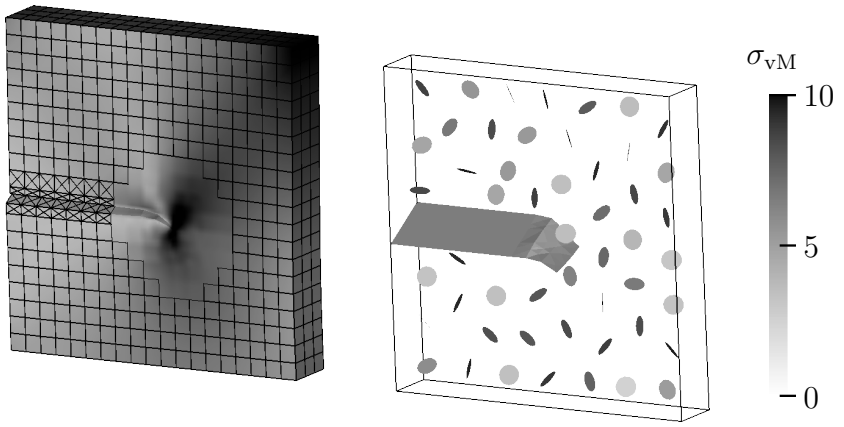

Figure 5.59: Mixed mode loading. Left: Deformed structure. Right: Crack path and 51 microcracks.

a difference between both paths. The impact of the microcracks is given in a detail of the crack front shown in figure 5.60(b): Considering microcracks enforces the crack to grow more in negative $\boldsymbol{e}_3$ direction.

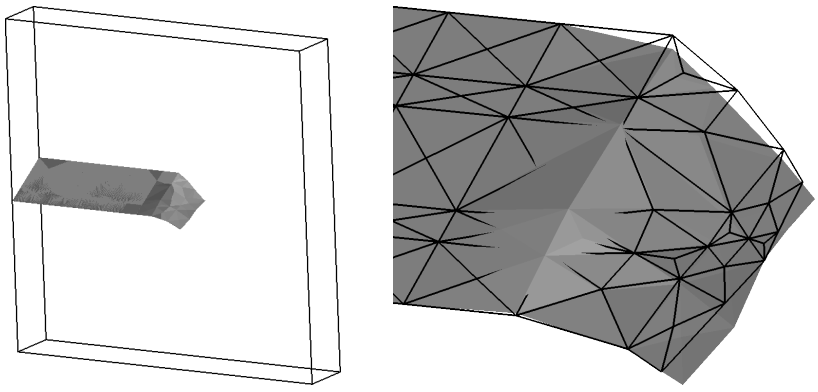

(a) Coarse scale paths. (b) Detail of crack fronts.

Figure 5.60: Crack paths considering microcracks (solid, gray) and without microcracks (left: solid, light gray / right: wireframe, black).

This example clarifies the need to take microcracks into account via the multiscale projection method: Using uniform refinement would require a mesh resolution of $95 \times 15 \times 95$ elements. Ignoring these fine scale effects would lead to a different crack path, especially when considering merging cracks between scales. Even without this feature, small but clear differences can be observed in terms of crack path and load factor λ^0.

Investigation of crack growth in a turbine blade

A more practical application is the evaluation of crack propagation in real structures. Special attention is given here to predict growth of microcracks in turbine blades as displayed in figure 5.61. This turbine blade is a rotor blade of the last stage of an air turbine and was designed by the Institute of Turbomachinery and Fluid Dynamics of the Gottfried Wilhelm

Leibniz Universität Hannover. It is mostly used to investigate fluid phenomena and therefore designed rather conservatively in terms of mechanical loading. To investigate microcrack growth efficiently, the whole $138\,\mathrm{mm}$ long turbine blade is first simulated over its lifetime without considering softening. This yields an estimation for the highest loaded quadrature point in the structure on which in the second step the crack propagation model is applied. If a crack propagates on the finest scale, it will usually continue propagating without increasing λ^0 in quasi-static simulations in LEFM. Thus, the blade needs to be maintained or replaced to ensure a safe operation.
The material of the blade, i.e. the high strength aluminum alloy CERTAL - EN AW 7022, is modeled by a viscoplastic solid considering small displacements. As this blade is subjected to high thermal loading, unidirectional thermomechanical coupling and temperature dependent material parameters describe the behavior sufficiently. An accurate application of the external loads, e.g. via unidirectional fluid structure coupling by ASCHENBRUCK ET AL. (2013), yields precise boundary conditions and with it a reliable response of the structure. Simulating the blade over its service life yields an estimation of the highest loaded quadrature point following a linear damage accumulation by PALMGREN (1924) and MINER (1945). As modeling this blade is not the main task of this work it is therefore not further explained here. The interested reader is referred to ROGGE & ROLFES (2012) for a detailed description and to HOLL ET AL. (2014) for a summary.

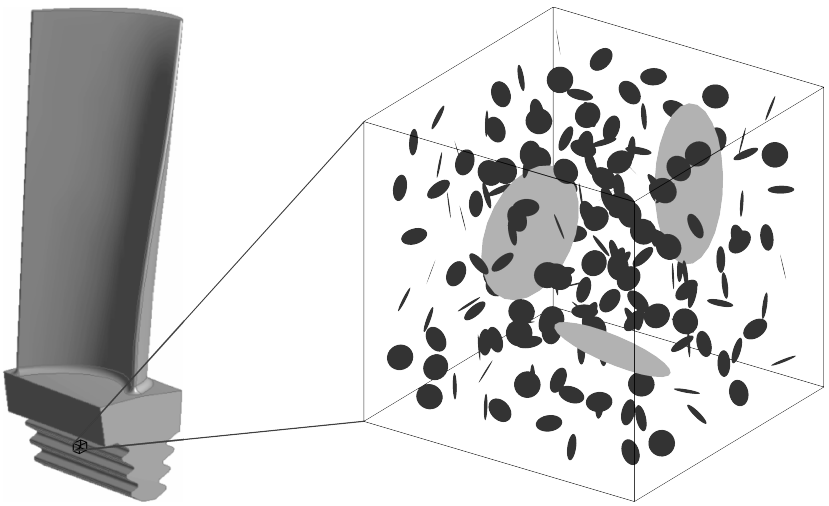

Figure 5.61: Investigated turbine blade (left) and corresponding micro domain (right).

The highest loaded point according to linear damage accumulation is in the fir-tree teeth of the blade as sketched in figure 5.61. The corresponding element has a volume $V \approx 1.08\,\mathrm{mm}^3$, which leads to an average unit cell of $0.6\,\mathrm{mm} \times 0.6\,\mathrm{mm} \times 0.6\,\mathrm{mm}$ using a five point integration rule, which is in the following investigated regarding crack propagation. This fine scale domain contains three larger ellipsoidal and 182 smaller circular cracks. The smaller cracks are only taken into account implicitly using the presented multiscale technique. The geometrical and mesh properties are summarized in table 5.8.
Following HOLL ET AL. (2014), inelastic deformations are nearly zero for the entire blade. As furthermore no softening is applied in the blade model, the concept of LEFM is ap-

Size of picked domain	$0.6\,\mathrm{mm} \times 0.6\,\mathrm{mm} \times 0.6\,\mathrm{mm}$
Macrocracks	Three ellipses with half-axis $0.15\,\mathrm{mm}$ and $0.11\,\mathrm{mm}$
Microcracks	182 circles with radius $25\,\mu\mathrm{m}$
Coarse scale mesh	$41 \times 41 \times 41$ elements
Fine scale mesh	$3 \times 3 \times 3$ elements per coarse scale element

Table 5.8: Properties of investigated domain.

plicable. Due to this nearly linear behavior during the whole service life, the ratio of the components of the strain tensor does not change. Thus, applying the highest strain tensor as a boundary condition on the fine scale is the most critical load case, i.e.

$$[\varepsilon_{ij}] = \begin{bmatrix} 2.51 & 2.31 & -0.05 \\ 2.31 & -1.64 & 0.08 \\ -0.05 & 0.08 & -0.05 \end{bmatrix} \cdot 10^{-3} \quad .$$

With YOUNG's modulus $E = 72,000\,\mathrm{MPa}$, POISSON's ratio $\nu = 0.33$ and the range of fracture toughness of $4.5\,\mathrm{N/mm} \leq \mathcal{G}_c \leq 49.5\,\mathrm{N/mm}$ according to GROSS & SEELIG (2007), the fine scale problem can be solved: The highest energy release $\mathcal{G}$ in the whole domain is $\mathcal{G} = 0.16\,\mathrm{N/mm}$. Thus, the external load can be increased by a factor of $5.7 \leq \lambda^0_{\max} \leq 19$, depending on the material parameter $\mathcal{G}_c$.
The VON MISES stress for $\mathcal{G} = \mathcal{G}_c = 4.5\,\mathrm{N/mm}$ is displayed in figure 5.62(a). As typical in LEFM, in all three non-overlapping fine scale domains the stresses are highest at the fronts. Increasing λ^0 to force a crack to grow leads to merging cracks just after the first propagation step. The final crack path is displayed in figure 5.62(b) without displaying the microcracks to maintain visibility.

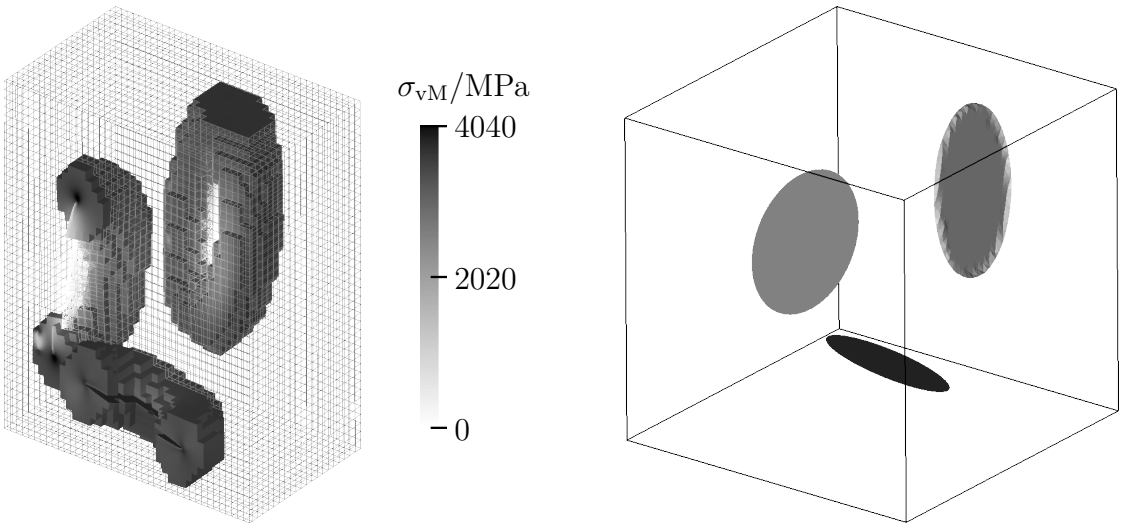

(a) Stress distribution in fine scale domains. Deformation scaled by factor 10.

(b) Final coarse scale cracks in undeformed domain.

Figure 5.62: Resulting crack path and stress distribution.

A reason for such a load capacity might be the conservative design of the turbine blade. However, this procedure still clarifies its benefits: The lifetime simulation with a comparatively simple model yields a precise estimation of the highest loaded point. Applying the strain history of this point to a microscale model capturing fine scale features leads to an evaluation of crack propagation on this scale. Thus, real structures can be analyzed precisely on the fine scale while the computational effort is kept as low as possible.

Chapter 6

Conclusions and outlook

Within this work, an adaptive multiscale technique for modeling crack interactions between scales was developed. The focus was set on modeling crack propagation and crack coalescence with computational efficiency, in order to investigate the behavior of microcracks on the global response of the structure.
Starting by analyzing two-dimensional problems, crack propagation utilizing the XFEM according to MOËS ET AL. (1999) and FRIES (2008) was introduced, which conformed well with experiments performed by INGRAFFEA & GRIGORIU (1990). The combination of the multiscale projection method and crack propagation allowed to account for microcracks in the vicinity of the crack front and lead to a fully adaptive numerical tool. In order to track a stable crack path, the criterion for crack growth required fulfillment on the finest scale. Therefore, an iteration scheme was presented, adapting the boundary conditions of the coarse scale. As crack propagation was computed on the finest scale, a method to upscale coarse scale trajectories onto the corresponding scale was presented. This feature yielded a multiscale technique for propagating cracks, fully driven by the finest scale. As cracks generally tend to merge at some stage of a fracturing process and as the numerical model was not able to account for crack coalescence, the simulations of the whole fracturing process were stopped as cracks approached each other. Especially when a large number of microcracks were considered, only a few propagation steps could be simulated. To incorporate this capability into the presented multiscale method to model crack propagation, an additional enrichment function for intersecting cracks, based on the work of DAUX ET AL. (2000), was applied to this model. In contrast to the crack coalescence approach by BUDYN ET AL. (2004), cracks were merged once the distance of a tip to a second crack fell below a mesh dependent threshold value. This value was chosen such that enrichment functions of different cracks did not overlap, so that the computation of the J-integral was carried out in domains with only one singular function. Additionally, the presented model considered merging crack tips using the same mesh based criterion for coalescence. To investigate the effect of microcracks on the overall behavior of the structure, the method for crack coalescence was coupled to the multiscale projection method. As macrocracks approach each other before crack coalescence will be detected on the fine scale, the XFEM was enhanced to capture even two macrocrack tips in one finite element. In order to keep the assignment of cracks and enrichments comparably simple, an alternative ramp function was introduced, which reduced the enrichment area to cracked elements. After this preparatory work on the coarse scale, several scenarios

of merging cracks of different scales were considered. Thus, this multiscale approach enabled scale transition via coalescence and furthermore handled vanishing and appearing fine scale domains during computation process, occurring due to crack coalescence. Besides this high flexibility and the fully adaptive computation of the fine scale domains, the numerical examples demonstrated the robustness of the presented method. Subsequently, multiscale analyses were compared to simulations without considering microcracks exhibiting a noticeable difference in crack paths and required load for crack propagation. Omitting only one microcrack changed the global response significantly, as demonstrated in the final example. Thus, the examples clearly exhibited the benefit of the proposed method as well as the need of considering all present microcracks.
The additional dimension of the crack front and crack surface coming with the three-dimensional approach required a revisit of the determination procedures of the J-integral needed for crack propagation. An alternative approach based on continuum damage mechanics was presented, capturing the mechanical properties of LEFM. This approach yielded slightly poorer results in LEFM compared to the J-integral, such that the integral was used in this work. Thus, the energy release rate scaled the boundary conditions to satisfy the criterion for crack propagation. The criterion of maximum hoop stress and a local geometrical approach to update the level set field presented in this work lead to a fast and stable update of the crack surface for the coming propagation step. In context of multiscale analysis, the coarse scale crack geometry was upscaled from the fine scale to the coarse scale to keep the integration algorithm, but still considering effects from the fine scale. A parallelization of the fine scale domains via OPENMP was introduced, which decreased the computation time. The presented examples demonstrated the ability of the proposed model: The level set update was able to display rotations in the crack path with a rather coarse mesh and followed the expected crack path. Similar to two-dimensional problems, microcracks influenced the global response of a structure in terms of crack path as well as required load for propagation. Despite the above mentioned achievements, four major tasks would improve the applicability of the model to more complex physical problems.

- The proposed model is implemented for quadrilateral and hexahedral elements. In order to mesh more general structures, e.g. turbine blades, higher order triangular and tetrahedral elements are required. A challenging problem is the biquadratic/triquadratic crack surface representation, which allows a single crack to intersect one element four times.

- Merging cracks in a three-dimensional multiscale analysis will most likely expose the effect of microcracks once more. This feature would furthermore allow a continuation of the multiscale computations presented here and display a post critical global response of the structure. However, crack coalescence in three-dimensional space requires intense programming and additional mechanical features: In contrast to two-dimensional problems, only three cracks per finite element would cover most merging scenarios, as this allows three merging surfaces intersecting in a single point. Besides this geometrical challenge, the mechanical behavior for partly joined cracks needs to be embedded into the finite element ansatz. Additionally, merging strategies between scales need to be revisited as coarse scale cracks cannot necessarily only be elongated.

- Most materials, especially metals, undergo plastic deformation before fracture. The application of a plastic material behavior has a significant impact on the fracture criterion: The evaluation of J-integral is not straightforward. Furthermore, the criterion of maximum hoop stress is only applicable to LEFM. With an appropriate choice of the driving quantity for crack propagation, the application of a damage model as presented in this work can resolve these issues, displayed in figure 6.1. Plasticity usually induces history variables, which are traditionally stored at quadrature points. Due to crack propagation, quadrature points move to avoid infinite entries in the stiffness matrix. Therefore, the application of a mapping strategy, e.g. SHEPARD's method, becomes inevitable. Furthermore, the singular enrichment functions at the crack front need to be replaced according to ELGUEDJ ET AL. (2006), to avoid infinite stresses at the crack front. This ansatz leads to a different crack opening behavior, since $\boldsymbol{u} \propto \sqrt{r}$.

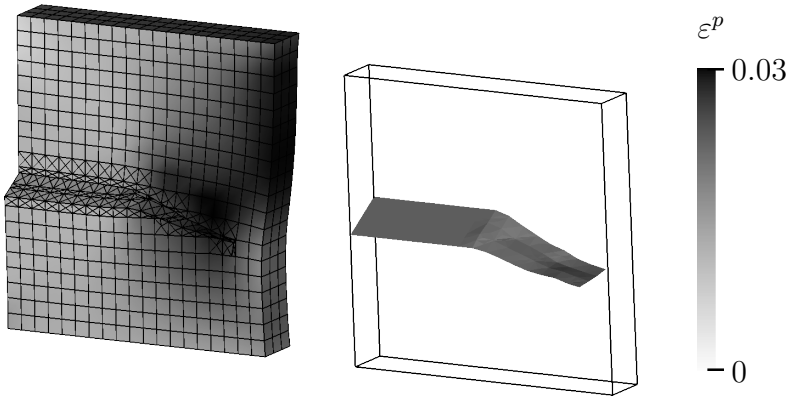

Figure 6.1: Effective plastic strain ε^p.

- The presented method is able to compute crack growth and crack coalescence on different scales. However, the fracturing of virgin materials cannot be captured by this model. According following to MAZARS & PIJAUDIER-CABOT (1996), a criterion for crack nucleation based on a damage model can resolve this remedy. Alternatively, a multiscale strategy by e.g. BELYTSCHKO ET AL. (2008) incorporating statistically distributed defects might be a suitable model: By evolving and merging these defects on the finest scale, macrocracks appear.

The above mentioned improvements are by far not the only possible extensions, but state which ones should be addressed first. However, this choice strongly depends on the problem being modeled, e.g. geometry, material behavior, size and orientation of cracks.

Bibliography

ALTENBACH J. & ALTENBACH H. *Einführung in die Kontinuumsmechanik*. Teubner, 1994.

ANDERSON T. *Fracture mechanics: Fundamentals and applications*. Taylor & Francis, 2005.

AREIAS P. & BELYTSCHKO T. Analysis of three-dimensional crack initiation and propagation using the extended finite element method. *International Journal for Numerical Methods in Engineering*, 63 (2005): 760–788.

AREIAS P., CÉSAR DE SÁ J. & CONCEIÇÃO ANTÓNIO C. A gradient model for finite strain elastoplasticity coupled with damage. *Finite Elements in Analysis and Design*, 39 (2003): 1191–1235.

ASCHENBRUCK J., MEINZER C., POHLE L., PANNING-VON SCHEIDT L. ET AL. Regeneration-induced forced response in axial turbines. In *Proceedings of the ASME Turbo Expo 2013*, GT2013, pages 1–12. 2013. GT2013-95431.

BABUŠKA I. & BANERJEE U. Stable generalized finite element method (SGFEM). *Computer Methods in Applied Mechanics and Engineering*, 201–204 (2012): 91–111.

BABUŠKA I., CALOZ G. & OSBORN J. Special finite element methods for a class of second order elliptic problems with rough coefficients. *SIAM Journal on Numerical Analysis*, 31 (1994): 945–981.

BALL J. Convexity conditions and existence theorems in nonlinear elasticity. *Archive for Rational Mechanics and Analysis*, 63 (1977): 337–403.

BARSOUM R. On the use of isoparametric finite elements in linear fracture mechanics. *International Journal for Numerical Methods in Engineering*, 10 (1976): 25–37.

BATHE K.J. *Finite-Elemente-Methoden: Matrizen und lineare Algebra, die Methode der finiten Elemente, Lösungen von Gleichgewichtsbedingungen und Bewegungsgleichungen*. Springer, 1986.

BAŽANT Z., BELYTSCHKO T. & CHANG T. Continuum theory for strain-softening. *Journal of Engineering Mechanics*, 110 (1984): 1666–1692.

BÉCHET E., MINNEBO H., MOËS N. & BURGARDT B. Improved implementation and robustness study of the X-FEM for stress analysis around cracks. *International Journal for Numerical Methods in Engineering*, 64 (2005): 1033–1056.

BELYTSCHKO T. & BLACK T. Elastic crack growth in finite elements with minimal remeshing. *International Journal for Numerical Methods in Engineering*, 45 (1999): 601–620.

BELYTSCHKO T., LIU W. & MORAN B. *Nonlinear Finite Elements for Continua and Structures*. Wiley, 2000.

BELYTSCHKO T., LOEHNERT S. & SONG H. Multiscale aggregating discontinuities: A method for circumventing loss of material stability. *International Journal for Numerical Methods in Engineering*, 73 (2008): 869–894.

BENZLEY S. Representation of singularities with isoparametric finite elements. *International Journal for Numerical Methods in Engineering*, 8 (1974): 537–545.

DE BERG M., CHEONG O., VAN KREVELD M. & OVERMARS M. *Computational Geometry: Algorithms and Applications*. Springer, 2008.

BERNARD P., MOËS N. & CHEVAUGEON N. Damage growth modeling using the Thick Level Set (TLS) approach: Efficient discretization for quasi-static loadings. *Computer Methods in Applied Mechanics and Engineering*, 233–236 (2012): 11–27.

BITTENCOURT T., WAWRZYNEK P., INGRAFFEA A. & SOUSA J. Quasi-automatic simulation of crack propagation for 2D LEFM problems. *Engineering Fracture Mechanics*, 55 (1996): 321–334.

BORDEN M., VERHOOSEL C., SCOTT M., HUGHES T. ET AL. A phase-field description of dynamic brittle fracture. *Computer Methods in Applied Mechanics and Engineering*, 217–220 (2012): 77–95.

BOURDIN B. *Une méthode variationnelle en mécanique de la rupture, théorie et applications numériques (A Variational Method for Brittle Fracture, Theory and Numerical Implementation)*. Ph.D. thesis, Université Paris Nord (1998).

BOURDIN B., FRANCFORT G. & MARIGO J.J. The variational approach to fracture. *Journal of Elasticity*, 91 (2008): 5–148.

BUDYN É. *Multiple Crack Growth by the eXtended Finite Element Method*. Ph.D. thesis, Northwestern University (2004).

BUDYN É., ZI G., MOËS N. & BELYTSCHKO T. A method for multiple crack growth in brittle materials without remeshing. *International Journal for Numerical Methods in Engineering*, 61 (2004): 1741–1770.

BYFUT A. & SCHRÖDER A. *hp*-adaptive extended finite element method. *International Journal for Numerical Methods in Engineering*, 89 (2012): 1392–1418.

BYSKOV E. The calculation of stress intensity factors using the finite element method with cracked elements. *International Journal of Fracture Mechanics*, 6 (1970): 159–167.

CHADWICK P. *Continuum mechanics: Concise theory and problems*. Dover Publications, Inc., 1999.

CHAN S., TUBA I. & WILSON W. On the finite element method in linear elastic fracture mechanics. *Engineering Fracture Mechanics*, 2 (1970): 1–17.

CHEW L. Constrained delaunay triangulations. *Algorithmica*, 4 (1989): 97–108.

CHOPP D. & SUKUMAR N. Fatigue crack propagation of multiple coplanar cracks with the coupled extended finite element / fast marching method. *International Journal of Engineering Science*, 41 (2003): 845–869.

COENEN E., KOUZNETSOVA V. & GEERS M. Novel boundary conditions for strain localization analyses in microstructural volume elements. *International Journal for Numerical Methods in Engineering*, 90 (2012): 1–21.

COLOMBO D. An implicit geometrical approach to level sets update for 3D non planar X-FEM crack propagation. *Journal of the Aeronautical Sciences*, 237–240 (2012): 39–50.

DAUX C., MOËS N., DOLBOW J., SUKUMAR N. ET AL. Arbitrary branched and intersecting cracks with the extended finite element method. *International Journal for Numerical Methods in Engineering*, 48 (2000): 1741–1760.

DAWICKE D., SUTTON M., NEWMAN J. & BIGELOW C. Measurement and analysis of critical CTOA for an aluminum alloy sheet. In ERDOGAN F., ed., *Fracture Mechanics: 25th Volume*, volume 1220 of *ASTM Special Technical Publication*, pages 358–379. ASTM Comm E 8 Fatigue & Fracture, 1995.

DE VREE J., BREKELMANS W. & VAN GILS M. Comparison of nonlocal approaches in continuum damage mechanics. *Computers & Structures*, 55 (1995): 581–588.

DOLBOW J. *An Extended Finite Element Method with Discontinuous Enrichment for Applied Mechanics*. Ph.D. thesis, Northwestern University (1999).

DOLBOW J., MOËS N. & BELYTSCHKO T. Discontinuous enrichment in finite elements with a partition of unity method. *Finite Elements in Analysis and Design*, 36 (2000): 235–260.

DOLBOW J., MOËS N. & BELYTSCHKO T. An extended finite element method for modeling crack growth with frictional contact. *Computer Methods in Applied Mechanics and Engineering*, 190 (2001): 6825–6846.

DUARTE C., BABUŠKA I. & ODEN T. Generalized finite element methods for three-dimensional structural mechanics problems. *Computers & Structures*, 77 (2000): 215–232.

DUARTE C., HAMZEH O., LISZKA T. & TWORZYDLO W. A generalized finite element method for the simulation of three-dimensional dynamic crack propagation. *Computer Methods in Applied Mechanics and Engineering*, 190 (2001): 2227–2262.

DUFFY M. Quadrature over a pyramid or cube of integrands with a singularity at a vertex. *SIAM Journal on Numerical Analysis*, 19 (1982): 1260–1262.

ELGUEDJ T., GRAVOUIL A. & COMBESCURE A. Appropriate extended functions for X-FEM simulation of plastic fracture mechanics. *Computer Methods in Applied Mechanics and Engineering*, 195 (2006): 501–515.

ERDOGAN F. & SIH G. On the crack extension in plates under plane loading and transverse shear. *Journal of Basic Engineering*, 85 (1963): 519–527.

ESHELBY J. The force on an elastic singularity. *Philosophical Transactions of the Royal Society. Series A*, 244 (1951): 87–112.

FEYEL F. & CHABOCHE J.L. FE^2 multiscale approach for modelling the elastoviscoplastic behaviour of long fibre SiC/Ti composite materials. *Computer Methods in Applied Mechanics and Engineering*, 183 (2000): 309–330.

FLORY P. Thermodynamic relations for high elastic materials. *Transactions of the Faraday Society*, 57 (1961): 829–838.

FRIES T. *A Stabilized and Coupled Meshfree/Meshbased Method for Fluid-Structure Interaction Problems*. Ph.D. thesis, Technische Universität Braunschweig (2005).

FRIES T. A corrected XFEM approximation without problems in blending elements. *International Journal for Numerical Methods in Engineering*, 75 (2008): 503–532.

FRIES T. & BAYDOUN M. Crack propagation with the extended finite element method and a hybrid explicit–implicit crack description. *International Journal for Numerical Methods in Engineering*, 88 (2012): 1527–1558.

FRIES T. & BELYTSCHKO T. The extended/generalized finite element method: An overview of the method and its applications. *International Journal for Numerical Methods in Engineering*, 84 (2010): 253–304.

FRIES T., BYFUT A., ALIZADA A., CHENG K. ET AL. Hanging nodes and XFEM. *International Journal for Numerical Methods in Engineering*, 86 (2011): 404–430.

GARZON J., O'HARA P., DUARTE C. & BUTTLAR W. Improvements of explicit crack surface representation and update within the generalized finite element method with application to three-dimensional crack coalescence. *International Journal for Numerical Methods in Engineering*, (2013). DOI: 10.1002/nme.4573.

GEERS M., KOUZNETSOVA V. & BREKELMANS W. Multi-scale computational homogenization: Trends and challenges. *Journal of Computational and Applied Mathematics*, 234 (2010): 2175–2182.

GRAVOUIL A., MOËS N. & BELYTSCHKO T. Non-planar 3D crack growth by the extended finite element and level sets – Part II: Level set update. *International Journal for Numerical Methods in Engineering*, 53 (2002): 2569–2586.

GRIFFITH A. The phenomenon of rupture and flow in solids. *Philosophical Transactions of the Royal Society. Series A*, 221 (1921): 163–198.

GROSS D. & SEELIG T. *Bruchmechanik*. Springer, 2007.

GURTIN M., FRIED E. & ANAND L. *The Mechanics And Thermodynamics Of Continua*. Cambidge University Press, 2010.

HAUPT P. *Continuum mechanics and theory of materials*. Springer, 2002.

HÄUSLER S., LINDHORST K. & HORST P. Combination of material force concept and the extended finite element method for mixed mode crack growth simulations. *International Journal for Numerical Methods in Engineering*, 85 (2011): 1522–1542.

HENSHELL R. & SHAW K. Crack tip finite elements are unnecessary. *International Journal for Numerical Methods in Engineering*, 9 (1975): 495–507.

HOLL M., LOEHNERT S. & WRIGGERS P. An adaptive multiscale method for crack propagation and crack coalescence. *International Journal for Numerical Methods in Engineering*, 93 (2013): 23–51.

HOLL M., ROGGE T., LOEHNERT S., WRIGGERS P. ET AL. 3D multiscale crack propagation using the XFEM applied to a gas turbine blade. *Computational Mechanics*, 53 (2014): 173–188.

HOLZAPFEL G. *Nonlinear solid mechanics*. Wiley, 2000.

HUGHES T. Multiscale phenomena: Green's functions, the Dirichlet-to-Neumann formulation, subgrid scale methods, bubbles and the origins of stabilized methods. *Computer Methods in Applied Mechanics and Engineering*, 127 (1995): 387–401.

HUTCHINSON J. Crack tip shielding by micro-cracking in brittle solids. *Acta Metallurgica*, 35 (1987): 1605–1619.

INGLIS C. Stresses in a plate due to the presence of cracks and sharp corners. *Transactions of the Royal Institution of Naval Architects*, 44 (1913): 219–241.

INGRAFFEA A. & GRIGORIU M. Probabilistic fracture mechanics: A validation of predictive capability. Technical Report 90-8, Department of Structural Engineering, Cornell University (1990).

IRWIN G. Analysis of stresses and strains near the end of a crack traversing a plate. *Journal of Applied Mechanics*, 24 (1957): 361–364.

KACHANOV L. Time of the rupture process under creep conditions. *Izvestiya Akademii Nauk SSSR. Otdelenie Tekhnicheskikh Nauk.*, 8 (1958): 26–31.

KIRSCH E. Die Theorie der Elastizität und die Bedürfnisse der Festigkeitslehre. *Zeitschrift des Vereins Deutscher Ingenieure*, 42 (1898): 797–807.

LABORDE P., POMMIER J., RENARD Y. & SALAÜN M. High-order extended finite element method for cracked domains. *International Journal for Numerical Methods in Engineering*, 64 (2005): 354–381.

LAN M., WAISMAN H. & HARARI I. A direct analytical method to extract mixed-mode components of strain energy release rates from Irwin's integral using extended finite element method. *International Journal for Numerical Methods in Engineering*, 95 (2013): 1033–1052.

LASRY D. & BELYTSCHKO T. Localization limiters in transient problems. *International Journal of Solids and Structures*, 24 (1988): 581–597.

LAZARUS V., BUCHHOLZ F., FULLAND M. & WIEBESIEK J. Comparison of predictions by mode II or mode III criteria on crack front twisting in three or four point bending experiments. *International Journal of Fracture*, 153 (2008): 141–151.

LEGRAIN G., MOËS N. & VERRON E. Stress analysis around crack tips in finite strain problems using the extended finite element method. *International Journal for Numerical Methods in Engineering*, 63 (2005): 290–314.

LEMAITRE J. Local approach of fracture. *Engineering Fracture Mechanics*, 25 (1986): 523–537.

LIU X., XIAO Q. & KARIHALOO B. XFEM for direct evaluation of mixed mode SIFs in homogeneous and bi-materials. *International Journal for Numerical Methods in Engineering*, 59 (2004): 1103–1118.

LOEHNERT S. A stabilization technique for the regularization of nearly singular extended finite elements. *Computational Mechanics*, (2013): (submitted).

LOEHNERT S. & BELYTSCHKO T. Crack shielding and amplification due to multiple microcracks interacting with a macrocrack. *International Journal of Fracture*, 145 (2007a): 1–8.

LOEHNERT S. & BELYTSCHKO T. A multiscale projection method for macro / microcrack simulations. *International Journal for Numerical Methods in Engineering*, 71 (2007b): 1466–1482.

LOEHNERT S. & MUELLER-HOEPPE D. Multiscale methods for fracturing solids. In REDDY B., ed., *IUTAM Symposium on Theoretical, Computational and Modelling Aspects of Inelastic Media*, pages 79–87. Springer, 2008.

LOEHNERT S., MUELLER-HOEPPE D. & WRIGGERS P. 3D corrected XFEM approach and extension to finite deformation theory. *International Journal for Numerical Methods in Engineering*, 86 (2011): 431–452.

MALVERN L. *Introduction to the Mechanics of a Continuous Medium*. Prentice-Hall, 1969.

MASSART T., PEERLINGS R. & GEERS M. An enhanced multi-scale approach for masonry wall computations. *International Journal for Numerical Methods in Engineering*, 69 (2007): 1022–1059.

MAZARS J. & PIJAUDIER-CABOT G. Continuum damage theory - Application to concrete. *Journal of Engineering Mechanics*, 115 (1989): 345–365.

MAZARS J. & PIJAUDIER-CABOT G. From damage to fracture mechanics and conversely: A combined approach. *International Journal of Solids and Structures*, 33 (1996): 3327–3342.

MEDIAVILLA J., PEERLINGS R.H.J. & GEERS M.G.D. Discrete crack modelling of ductile fracture driven by non-local softening plasticity. *International Journal for Numerical Methods in Engineering*, 66 (2006a): 661–688.

MEDIAVILLA J., PEERLINGS R.H.J. & GEERS M.G.D. A robust and consistent remeshing-transfer operator for ductile fracture simulations. *Computers & Structures*, 84 (2006b): 604–623.

MELENK J. & BABUŠKA I. The partition of unity finite element method: Basic theory and applications. *Computer Methods in Applied Mechanics and Engineering*, 139 (1996): 289–314.

MENK A. & BORDAS S. A robust preconditioning technique for the extended finite element method. *International Journal for Numerical Methods in Engineering*, 85 (2011): 1609–1632.

MIEHE C., SCHRÖDER J. & SCHOTTE J. Computational homogenization analysis in finite plasticity – simulation of texture development in polycrystalline materials. *Computer Methods in Applied Mechanics and Engineering*, 171 (1999): 387–418.

MIEHE C., WELSCHINGER F. & HOFACKER M. Thermodynamically consistent phase-field models of fracture: Variational principles and multi-field FE implementations. *International Journal for Numerical Methods in Engineering*, 83 (2010): 1273–1311.

MINER M. Cumulative damage in fatigue. *Journal of Applied Mechanics*, 12 (1945): A159–A164.

MINNEBO H. Three-dimensional integration strategies of singular functions introduced by the XFEM in the LEFM. *International Journal for Numerical Methods in Engineering*, 92 (2012): 1117–1138.

MOËS N. Initiation and crack growth with the Thick Level Set damage model coupled to the eXtended Finite Element Method. In GRAVOUIL A., ed., *3rd Conference on the Extended Finite Element Method*. Lyon, France, 2013.

MOËS N. & BELYTSCHKO T. Extended finite element method for cohesive crack growth. *Engineering Fracture Mechanics*, 69 (2002): 813–833.

MOËS N., DOLBOW J. & BELYTSCHKO T. A finite element method for crack growth without remeshing. *International Journal for Numerical Methods in Engineering*, 46 (1999): 131–150.

MOËS N., GRAVOUIL A. & BELYTSCHKO T. Non-planar 3D crack growth by the extended finite element and level sets – Part I: Mechanical model. *International Journal for Numerical Methods in Engineering*, 53 (2002): 2549–2568.

MOËS N., STOLZ C., BERNARD P. & CHEVAUGEON N. A level set based model for damage growth: The thick level set approach. *International Journal for Numerical Methods in Engineering*, 86 (2011): 358–380.

MOONEY M. A theory of large elastic deformation. *Journal of Applied Physics*, 11 (1940): 582–592.

MORAN B. & SHIH C.F. Crack tip and associated domain integrals from momentum and energy balance. *International Journal of Fracture*, 27 (1987a): 615–642.

MORAN B. & SHIH C.F. A general treatment of crack tip contour integrals. *International Journal of Fracture*, 35 (1987b): 295–310.

MOUSAVI S. & SUKUMAR N. Generalized Duffy transformation for integrating vertex singularities. *Computational Mechanics*, 45 (2010): 127–140.

MUELLER-HOEPPE D. *A multiscale method for fracturing solids*. Ph.D. thesis, Institut für Kontinuumsmechanik (2012).

MUSKHELISHVILI N. *Some Basic Problems of the Mathematical Theory of Elasticity*. P. Noordhoff, 1963.

NOLL W. Die Herleitung der Grundgleichungen der Thermomechanik der Kontinua aus der Statistischen Mechanik. *Journal of Rational Mechanics and Analysis*, 4 (1955): 627–646.

NUISMER R. An energy release rate criterion for mixed mode fracture. *Journal of Rational Mechanics and Analysis*, 11 (1975): 245–250.

OGDEN R. Large deformation isotropic elasticity - on the correlation of theory and experiment for incompressible rubberlike solids. *Proceedings of the Royal Society A: Mathematical, Physical and Engineering Sciences*, 326 (1972): 565–584.

OGDEN R. *Non-linear elastic deformations*. Dover, 1984.

OLIVER J. Continuum modelling of strong discontinuities in solid mechanics using damage models. *Computational Mechanics*, 17 (1995): 49–61.

OLIVER J. Modelling strong discontinuities in solid mechanics via strain softening constitutive equations. Part 1: Fundamentals. *International Journal for Numerical Methods in Engineering*, 39 (1996a): 3575–3600.

OLIVER J. Modelling strong discontinuities in solid mechanics via strain softening constitutive equations. Part 2: Numerical simulation. *International Journal for Numerical Methods in Engineering*, 39 (1996b): 3601–3623.

OSHER S. & SETHIAN J. Fronts propagating with curvature-dependent speed: Algorithms based on Hamilton-Jacobi formulations. *Journal of Computational Physics*, 79 (1988): 12–49.

OZER H., DUARTE C. & AL-QADI I. Formulation and implementation of a high-order 3-D domain integral method for the extraction of energy release rates. *Computational Mechanics*, 49 (2012): 459–476.

PALMGREN A. Die Lebensdauer von Kugellagern (The service life of ball bearings). *Zeitschrift des Vereins Deutscher Ingenieure*, 68 (1924): 339–341. (NASA TT F-13460).

PANDOLFI A. & ORTIZ M. An eigenerosion approach to brittle fracture. *International Journal for Numerical Methods in Engineering*, 92 (2012): 694–714.

PASSIEUX J., GRAVOUIL A., RÉTHORÉ J. & BAIETTO M. Direct estimation of generalized stress intensity factors using a three-scale concurrent multigrid X-FEM. *International Journal for Numerical Methods in Engineering*, 85 (2011): 1648–1666.

PEERLINGS R. *Enhanced damage modelling for fracture and fatigue*. Ph.D. thesis, Technische Universiteit Eindhoven (1999).

PEERLINGS R., DE BORST R., BREKELMANS W. & DE VREE J. Gradient enhanced damage for quasi-brittle materials. *International Journal for Numerical Methods in Engineering*, 39 (1996): 3391–3403.

PEREIRA J., KIM D.J. & DUARTE C. A two-scale approach for the analysis of propagating three-dimensional fractures. *Computational Mechanics*, 49 (2012): 99–121.

PIJAUDIER-CABOT G. & BAŽANT Z. Nonlocal damage theory. *Journal of Engineering Mechanics*, 113 (1987): 1512–1533.

POMMIER S., GRAVOUIL A., COMBESCURE A. & MOËS N. *Extended Finite Element Method for Crack Propagation*. Iste Publishing Company, 2011.

PRANGE C., LOEHNERT S. & WRIGGERS P. Error estimation for crack simulations using the XFEM. *International Journal for Numerical Methods in Engineering*, 91 (2012): 1459–1474.

RABCZUK T., BORDAS S. & ZI G. On three-dimensional modelling of crack growth using partition of unity methods. *Computers & Structures*, 88 (2010): 1391–1411.

RÉTHORÉ J., ROUX S. & HILD F. Hybrid analytical and extended finite element method (HAX-FEM): A new enrichment procedure for cracked solids. *International Journal for Numerical Methods in Engineering*, 81 (2010): 269–285.

RICE J. A path independent integral and the approximate analysis of strain concentration by notches and cracks. *Journal of Applied Mechanics*, 35 (1968): 379–386.

RICHARD H., FULLAND M. & SANDER M. Theoretical crack path prediction. *Fatigue & Fracture of Engineering Materials & Structures*, 28 (2005): 3–12.

RIVLIN R. Large elastic deformations of isotropic materials. IV. Further developments of the general theory. *Philosophical Transactions of the Royal Society. Series A*, 241 (1948): 379–397.

ROGGE T. & ROLFES R. Stochastische Untersuchungen regenerationsbedingter Imperfektionen einer Turbinenschaufel: Modellierung des deterministischen Modells zur effizienten Berechnung des Schwingungs- und Festigkeitsverhaltens. In *5. Dresdner-Probabilistik-Workshop*. Dresden, Germany, 2012.

ROSE L. Effective fracture toughness of microcracked materials. *Journal of the American Ceramic Society*, 69 (1986a): 212–214.

ROSE L. Microcrack interaction with a main crack. *International Journal of Fracture*, 31 (1986b): 233–242.

RUBINSTEIN A. Macrocrack interaction with semi-infinite microcrack array. *International Journal of Fracture*, 27 (1985): 113–119.

RUBINSTEIN A. Macrocrack-microdefect interaction. *Journal of Applied Mechanics*, 53 (1986): 505–510.

SEABRA M., ŠUŠTARIČ P., CÉSAR DE SÁ J. & RODIČ T. Damage driven crack initiation and propagation in ductile metals using XFEM. *Computational Mechanics*, 52 (2013): 161–179.

SIH G. Strain-energy-density factor applied to mixed mode crack problems. *International Journal of Fracture*, 10 (1974): 305–321.

SIMO J. & HUGHES T. *Computational inelasticity*. Springer, 1998.

SIMO J. & JU J. Strain- and stress-based continuum damage models - I. Formulation. *International Journal of Solids and Structures*, 23 (1987a): 821–840.

SIMO J. & JU J. Strain- and stress-based continuum damage models - II. Computational aspects. *International Journal of Solids and Structures*, 23 (1987b): 841–869.

SIMO J., OLIVER J. & ARMERO F. An analysis of strong discontinuities induced by strain-softening in rate-independent inelastic solids. *Computational Mechanics*, 12 (1993): 277–296.

STOLARSKA M., CHOPP D., MOËS N. & BELYTSCHKO T. Modelling crack growth by level sets in the extended finite element method. *International Journal for Numerical Methods in Engineering*, 51 (2001): 943–960.

STROUBOULIS T., COPPS K. & BABUŠKA I. The generalized finite element method: An example of its implementation and illustration of its performance. *International Journal for Numerical Methods in Engineering*, 47 (2000): 1401–1417.

STROUBOULIS T., COPPS K. & BABUŠKA I. The generalized finite element method. *Computer Methods in Applied Mechanics and Engineering*, 32–33 (2001): 4081–4193.

SUKUMAR N., CHOPP D. & MORAN B. Extended finite element method and fast marching method for three-dimensional fatigue crack propagation. *Engineering Fracture Mechanics*, 70 (2003): 29–48.

SUKUMAR N., MOËS N., MORAN B. & BELYTSCHKO T. Extended finite element method for three-dimensional crack modelling. *International Journal for Numerical Methods in Engineering*, 48 (2000): 1549–1570.

SZABÓ I. *Geschichte der mechanischen Prinzipien und ihrer wichtigsten Anwendungen*. Birkhäuser Verlag, 1987.

TRELOAR L. The elasticity of a network of long-chain molecules – I. *Transactions of the Faraday Society*, 39 (1943a): 36–41.

TRELOAR L. The elasticity of a network of long-chain molecules – II. *Transactions of the Faraday Society*, 39 (1943b): 241–246.

TRUESDELL C. & NOLL W. *The non-linear field theories of mechanics*. Springer, 1965.

TRUESDELL C. & TOUPIN R. *The classical field theories*. Springer, 1960.

WELLS G., SLUYS L. & DE BORST R. Simulating the propagation of displacement discontinuities in a regularized strain-softening medium. *International Journal for Numerical Methods in Engineering*, 53 (2002): 1235–1256.

WESTERGAARD H. Bearing pressures and cracks. *Journal of Applied Mechanics*, 6 (1939): A49–A53.

WILLIAMS M. Stress singularities resulting from various boundary conditions in angular corners of plates in extension. *Journal of Applied Mechanics*, 19 (1952).

WILLIAMS M. On the stress distribution at the base of a stationary crack. *Journal of Applied Mechanics*, 24 (1957).

WRIGGERS P. *Nonlinear Finite Element Methods*. Springer, 2008.

ZAMANI A., GRACIE R. & ESLAMI M. Cohesive and non-cohesive fracture by higher-order enrichment of XFEM. *International Journal for Numerical Methods in Engineering*, 90 (2012): 452–483.

ZIENKIEWICZ O. & TAYLOR R. *The Finite Element Method for Solids and Structural Mechanics*. Elsevier Butterworth-Heinemann, 2005a.

ZIENKIEWICZ O. & TAYLOR R. *The Finite Element Method. Its Basis and Fundamentals*. Elsevier Butterworth-Heinemann, 2005b.

Curriculum vitae

Matthias Holl

born May 19, 1985 in Mettingen, Germany

Research Experience

since 02.2010	Research assistant at the Institute of Continuum Mechanics, Leibniz Universität Hannover, Germany

Education

10.2005 - 12.2009	Leibniz Universität Hannover Civil Engineering Focus: Computational Mechanics Degree: Dipl.-Ing.
08.2008 - 01.2009	Kungliga Tekniska högskolan, Stockholm, Sweden Mechanical Engineering Focus: Computational Mechanics

Awards and Scholarships

01.2010	Victor-Rizkallah Award for exceptional accomplishments at the Department of Civil Engineering of the Leibniz Universität Hannover in 2010